UNIVERSITÀ DEGLI STUDI DI PADOVA

Dipartimento di Fisica e Astronomia “Galileo Galilei”

Master Degree in Astrophysics and Cosmology

Final Dissertation

Impact of Wolf-Rayet stellar winds on compact object formation

Supervisor

Dr. Michele Trabucchi

Co-supervisors

Prof. Dr. Michela Mapelli

Dr. Lumen Boco

Candidate

Sofia Mesini

Academic Year 2024/2025

Contents

Abstract

Wolf-Rayet (WR) stars are massive stars that have lost their hydrogen envelopes, exposing the underlying helium cores. In the Small Magellanic Cloud (SMC), 12 WR stars have been observed, 7 of which appear to be single.
To exist without a binary companion, these stars must have undergone a self-stripping process. Although such a mechanism is theoretically plausible, current models of line-driven stellar winds, combined with the relatively low metallicity of the SMC, fail to fully account for the presence of apparently isolated WR stars. This is primarily due to the reduced strength of stellar winds at low metallicity, which is generally insufficient to remove the hydrogen envelope.
In this thesis, I have implemented a new model for radiation-driven stellar winds within the MESA stellar evolution code. This model includes the possibility of activating optically thick winds when a star approaches the Eddington limit.
I demonstrate that rapidly rotating stars can enter the thick-wind regime, successfully removing their hydrogen envelopes and evolving into WR stars even at low metallicity. The resulting stellar evolutionary tracks were subsequently used as input for the population synthesis code SEVN, to evaluate the impact of the new wind model on binary star populations.
Finally, the output from SEVN was used to estimate the merger efficiency of binary black hole (BBH) systems in this population, with the goal of addressing the persistent overestimation of the BBH merger rate density by theoretical models, compared to that inferred by the LIGO-Virgo-Kagra (LVK) collaboration.
Multiple relevant results have been found. Firstly, optically thick winds are able to reduce the hardening of the binary, therefore lowering the merger efficiency. On the other hand, this effect significantly increases the time delay between formation and black hole merger, which on average becomes about 10 Gyr. This means that the mergers observed today through GWs originate from objects formed at cosmic noon or earlier.

Chapter 1

Introduction

During the last few years, the gravitational wave signals observed by LIGO and Virgo have been of increasing importance to allow a deeper understanding of the surrounding universe.
From these observations, many quantities have been inferred, such as the merger rate density $\mathcal{R}$, the number of compact binaries merging per unit time and space.
Comparing the inferred value of $\mathcal{R}$ in the local universe with the value predicted from galactic models, it is clear that there is a theoretical overestimation of the actual value of this quantity, as demonstrated in [1] and shown in figure Figure 1.1.

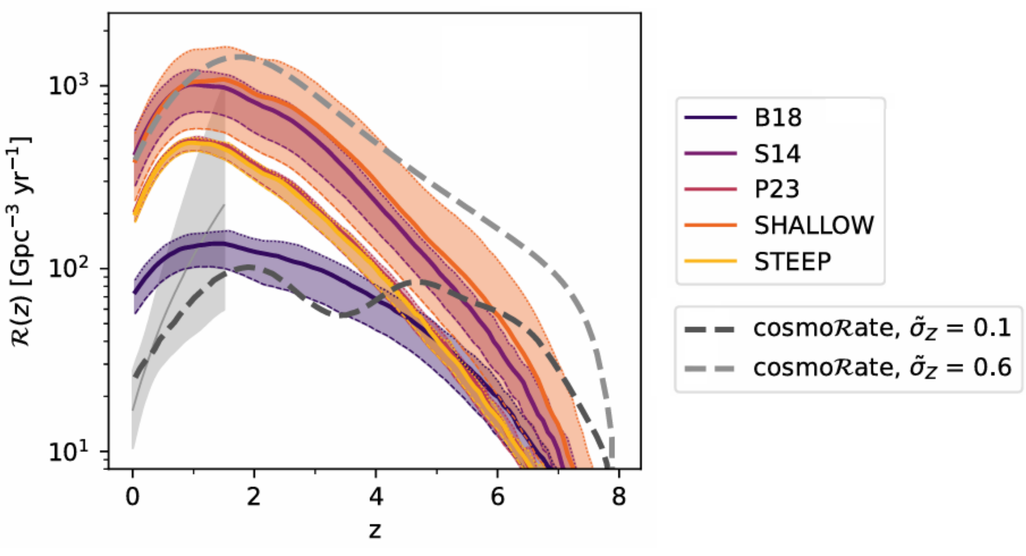

Figure 1.1: Evolution of $\mathcal{R}$ as a function of redshift for different galactic models, taken from [1]. Different colors represent, in order, the galactic models by [2], [3], [4] and the models employed in [1]. The dashed lines show the merger rate density obtained with cosmoRate [5]. Finally the gray shaded area shows the significantly lower $\mathcal{R}$ inferred by the LIGO-Virgo-KAGRA (LVK) collaboration.

In Figure 1.1, the binary black hole (BBH) merger rate density as a function of redshift for different observational scaling relations is shown.

To match the value of the merger rate density inferred from experimental data, there is a need for the modeled merger rate density to be reduced. In order to do so, one could follow many different strategies. To attempt at finding a possible solution, this thesis starts from a more in-depth study of the final stages of massive stars' lives, focusing mainly on Wolf-Rayet (WR) stars and their formation.

Wolf-Rayet stars are an incredibly interesting and fascinating kind of stars which have had the external layers of their envelopes stripped, either by winds or by binary interactions, leaving their cores progressively more exposed.
These stars, apart from being extremely complex to model due to their strong stellar winds and peculiar atmospheres, are also an essential stage in the life of stars that end up forming binary compact objects and, in particular, binary black holes.
This was studied extensively in [6], and summarized in Figure 1.2.

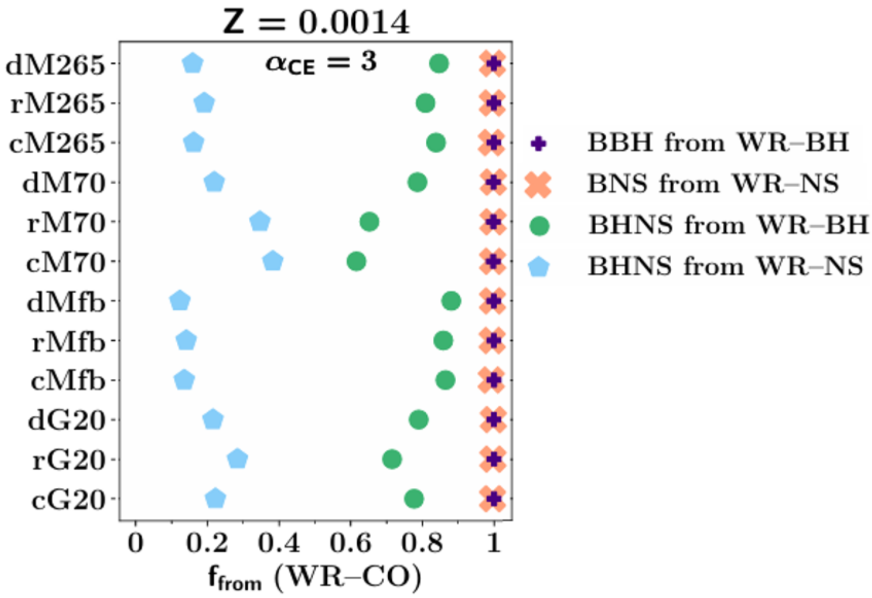

Figure 1.2: Fraction of BCO generated from different configurations, taken from [6]. With different markers are represented the fractions of each kind of binary compact object (BCO) resulting from a configuration where a WR star is involved. The dark blue crosses display the binary black hole systems originating from a WR-BH configuration.

From the dark blue crosses in Figure 1.2, it appears evident that almost all the systems coming from a WR-CO configuration end up resulting in a BBH system, highlighting once more the crucial importance of an in-depth knowledge of WR stars evolution in the context of the study of BBH formation.

As hinted before, WR stars are also extremely intriguing because of their strong stellar mass loss rates. In the context of stellar evolution, stellar winds are considered a fundamental factor in shaping the behavior of a star, but in the case of massive stars they become crucial, as they define the final fate of the stars and their compact remnant.

A fascinating environment for studying WR stars is surely the Small Magellanic Cloud (SMC), an irregular dwarf galaxy near the Milky Way, which is characterized by its relatively low metallicity, about $1/5\,Z_{\odot}$. These conditions contribute in making it an incredible laboratory to study the evolution of close-by young massive stars.
In this galaxy, 12 WRs have been observed so far and 7 of them appear to be lacking a binary companion, as found by the extensive tests performed by [7].
From these results a puzzling question arises, concerning the formation of those 7 - apparently isolated - WR stars. Indeed, these kind of stars, according to state-of-the-art wind models, can

be stripped almost exclusively by binary interactions in relatively low metallicity environments, since line driven stellar winds are not strong enough to allow the stars to self-strip their envelope.

Optically thin wind models currently in use in many stellar evolution codes are not able to reproduce the observations of WR stars, since they avoid stripping off their envelope and, instead, move towards the cooler side of the H-R diagram and become inflated supergiants.
This behavior is particularly problematic for the SMC metallicity because the simulated stars, instead of becoming hot WR stars, actually end up producing stellar tracks dying within the Humphreys-Davidson (HD) limit, an observational threshold for temperature and luminosity of massive stars, contributing to the well-known problem of overproduction of overluminous supergiants, already addressed in [8].

In an attempt understand and hopefully solve the modeling issues introduced before, a strategy could lie in implementing models for stronger winds - more specifically optically thick winds. Indeed these stronger winds could provide an enhanced self-stripping of the stars and also generate effects that could influence and maybe decrease the number of merging BBHs.

With this aim in mind, the main focus of this thesis is a detailed study of Wolf-Rayet stars from the point of view of their stellar winds, with particular attention on optically thick winds.
A new optically thick wind model has been implemented in the stellar evolutionary code MESA, in order to analyze the impact of these winds both on single star, through an in-depth study of the produced stellar tracks, and on binary systems, via population studies. The main focus of this work is to find a formation channel for single WRs in relatively low metallicity environments. In addition to this, the effect of the new stellar wind model will be studied also on binary stars, aiming for a reduction of the merger efficiency for BBH and, consequently, of the merger rate density.

This work is organized as follows: in Chapter 2 will be given an introduction on massive stars' evolution; a more thorough discussion on stellar winds will then be carried on in Chapter 3, focusing mainly on the optically thick wind model adopted in this work and the results obtained using the stellar evolution code MESA. In Chapter 4, the impact of the winds studied in the previous sections on binary stellar evolution will be analyzed through a population study and the calculation of the merger efficiency. Finally, the main results and conclusions of this work will be collected in Chapter 5.

Chapter 2

Massive stars

Massive stars are defined as stars that are massive enough to be able to evolve beyond helium burning into the advanced phases of nuclear burning, as it explained in [9]. Depending on the considered physics, their initial mass is usually in the range $8 - 10\,M_\odot \leq M_{ZAMS} \leq 100\,M_\odot$. This classification is made on the minimum initial mass necessary to ignite nuclear reactions far more energetic than the ones that characterize the evolution of less massive stars. Indeed, below this threshold, the stellar core is unable to reach a temperature high enough to ignite carbon burning. The upper limit in the mass range is instead used to identify the transition between massive and very-massive stars.

Massive stars occupy the upper end of the Hertzsprung-Russell diagram (HRD). Their generally high luminosities, temperatures, and high central pressures permit H-burning to occur via the CNO cycle. This subsequently allows the ignition of progressively heavier fuels up to the production of an iron core. One of the peculiarities of these stars is their very brief evolution: due to their high luminosity and small timescale for the nuclear burning processes, their lives last only a few millions or tens of millions of years, just a relatively short interval of time on a cosmic timescale. Indeed, although they can benefit from a vast fuel reservoir, the burning happens at faster pace than in smaller stars because of the extreme temperatures reached in the core. In addition to this, strong radiation pressure and stellar winds critically influence the chemical composition and structure of the external layers of these stars, with dramatic consequences for the final outcome of their lives.

Despite being rare objects (only 2-3 stars more massive than $8M_\odot$ are formed every 1000 stars of low or intermediate mass [9]), these stars play an incredibly important role in shaping and influencing galactic life for multiple reasons. First of all, they produce most of the elements found in the universe, which are also essential for the existence of life. Because of their usually strong winds, they inject these elements into the interstellar medium, producing a chemical enrichment of the environment. On a second note, massive stars are also responsible for the production of compact objects, neutron stars and black holes, and catastrophic events, such as supernova explosions, unlike stars of lower masses. Moreover, these stars influence their environment also from the dynamical point of view. Indeed, strong winds and supernova explosions generate shockwaves that heat up the surrounding gas, expelling it from the galactic disk. This can lead to a reduction in the star formation rate. However, the turbulences and gas compression resulting from a SN explosion can sometimes produce also the opposite effect, indirectly triggering star formation in their surroundings. Since these stars are fairly rare, only a few hundreds of these stars have been observed until recently, and to deepen our knowledge about massive stars, we rely heavily on numerical modeling.

2.1 Evolution

As stated in [10], it is possible to consider the evolution of a massive star as a path towards increasingly higher central temperature and density, with a decreasing central entropy. This path is interrupted by stages of thermal equilibrium powered by nuclear burning that can trigger instabilities and drive convection. In general, the evolution of massive stars is dramatically influenced by a wide variety of parameters, such as their initial mass, chemical composition, rotation, and energy transport mechanisms. To understand the structure and evolution of stars and their observational properties, it is necessary to rely on known laws of physics. The evolution of a star is described by 5 main equations, all expressed with respect in the mass coordinate system:

1. **Mass conservation**:
$$\frac{\partial r}{\partial m} = \frac{1}{4\pi r^2 \rho} \tag{2.1}$$
where r is the radial coordinate, m the mass coordinate and ρ the density of the star

2. **Momentum conservation**:
$$\frac{\partial P}{\partial m} = -\frac{Gm}{4\pi r^4} - \frac{1}{4\pi r^2}\frac{d^2 r}{dt} \tag{2.2}$$
where P is the pressure, and t is the time coordinate

3. **Energy conservation**:
$$\frac{\partial L}{\partial m} = \epsilon_{nuc} - \epsilon_{\nu} \tag{2.3}$$
where ϵ_{nuc} is the energy gained from nuclear reactions and ϵ_{ν} is the energy lost from neutrinos

4. **Energy transport**:
$$\frac{\partial T}{\partial m} = -\frac{GmT}{4\pi r^4 P}\nabla \tag{2.4}$$
where T is the temperature and $\nabla = \dfrac{d\,ln\,T}{d\,ln\,P}$ which depends on the dominant energy transport mechanism, either radiation, convection, or conduction.

5. **Nucleosynthesis and mixing**:
$$\frac{\partial X_i}{\partial t} = \frac{m_i}{\rho}\left(\sum_j r_{ji} - \sum_k r_{ik}\right) \tag{2.5}$$
where $r_{ij}\,(r_{ik})$ is the rate of reactions that transform the element $j\,(i)$ into $i\,(k)$.

2.1.1 From Main Sequence to Advanced Evolutionary Phases

Every massive star's life goes through a series of nuclear burning stages, that get progressively more rapid and energetic. These stages happen one after the other, ending when the precedent fuel is exhausted and gravity forces the star to contract and heat up, allowing the ignition of the next fuel and starting the next burning stage. The burning phases are characterized by the kind of fuel ignited at that time, and are summarized below from [9]:

- **Hydrogen burning**: In massive stars, this burning occurs via the CNO cycle, given by $^{12}C(p,\gamma)^{13}N(\beta+)^{13}C(p,\gamma)^{14}N(p,\gamma)^{15}O(\beta+)^{15}N(p,\alpha)^{12}C$, converting Hydrogen to Helium, releasing $\simeq$ 6.5 MeV per nucleon in nuclear binding energy. Part of this energy (about 7%) is lost from the star as neutrinos escape the plasma. During this stage, the star typically appears stable and less luminous than in the following ones. This phase is often referred to as the *main sequence*, and is the longest evolutionary stage, lasting millions of years. After Hydrogen exhaustion in the core, the burning usually continues in a shell, that sits on top of the newly-formed Helium core. During the advanced burning stages, it is possible for the Hydrogen shell to be either mixed with the convective envelope in the so-called *dredge up* episodes (more common for less massive stars), or stripped away by stellar winds or eruptions (usually happening for the most massive stars).

- **Helium burning**: During this phase, nuclear burning is powered by the *triple alpha* reaction, that converts Helium in Carbon through $^4He \rightarrow ^{12}C$. Up to the depletion of Helium, Carbon accumulates in the core, and the transformation of Carbon in Oxygen starts dominating. The two reactions, in He-burning conditions, have the same temperature dependence but a different dependence on density. Due to this discrepancy, the resulting C to O ratio at the end of He-burning may vary due to different stellar densities. Indeed, stars on the low mass end are denser and produce more Carbon than Oxygen, while the behavior is reversed for stars on the high mass end. Just like in the Hydrogen case, after helium is depleted inside the core, it can be re-ignited in a shell on top of the CO core. For high enough initial stellar masses, this shell may also become convective. The core He-burning produces about 10% of the energy per nucleon of H-burning, and its duration is of the order of hundreds of thousands of years, only $\simeq$ 10% of the H-burning phase duration.

- **Carbon burning**: After He depletion in the core, the star contracts and the temperature in the core rises again, igniting Carbon burning. During this stage, the dominant reactions in the core are $^{12}C + ^{12}C$, which result in the production of an excited state of Magnesium. This subsequently de-excites, emitting neutrons, protons and alpha particles. The de-excitation products start secondary reactions, whose outcome usually is represented by the production of Neon and Oxygen. Depending on the carbon mass fraction left behind by core He-buring, C-burning can happen either as a convective or as radiative phase. During C-burning, the neutrino luminosity of the star increases dramatically, emitting $\simeq$10,000 times more energy in neutrinos than in visible light [9]. This phase is more unstable than the previous ones, and much faster, since it lasts only a few thousands of years.

- **Neon burning**: The Neon burning phase is powered by 2 reactions: $^{20}Ne(\gamma,\alpha)^{16}O$, endothermic, and $^{20}Ne(\alpha,\gamma)^{24}Mg$, exothermic, that release twice as much energy as the one needed for the first reaction to happen. It is usually a rather brief phase, induced by photo-disintegration of the Neon nuclei.

- **Oxygen burning**: This fusion phase is similar to the Carbon one, where the dominant reaction is given by $^{16}O + ^{16}O$, that results in excited Sulfur nuclei. These nuclei then de-excite, emitting neutrons, protons and alpha particles inducing secondary reactions. The final outcome is a mixture of Silicon, Sulfur and a small amount of Magnesium, left by Neon burning. O-burning phase is more extended and powerful with respect to Neon burning and, for the extent of its duration, the star starts assuming a progressively more stratified structure with concentric shells burning different fuels, reaching the so-called *onion-like structure*.

- **Silicon burning**: This is the last fusion phase possible, happening through a sequence of photo-disintegrations and α captures, lasting usually just a few days. The final outcome of this series of reactions is a mixture of Iron group isotopes.
- **Iron core formation and collapse**: Iron and Nichel mark the end of spontaneous nuclear fusion processes, since their burning is endothermic and would require a massive amount of energy to ignite and being carried on. For this reason, the last process that goes on in the star is Silicon burning. The Si-burning continues to be carried on in a shell, adding mass to the Iron core. This core becomes increasingly more massive until it reaches the so-called *Chandrasekhar limit* of $1.4M_{\odot}$. Beyond this limit, electron degeneracy pressure is no longer sufficient to prevent the gravitational pull from making the star collapse.

The different stages of a massive star's life are visible in the following Kippenhan diagram, analyzed in [11], where the evolution of the internal structure of a non-rotating 20 $M_{\odot}$ star is shown: particularly visible is the onion-like structure in the final stages of the stellar life, where all the different fuels are burning in shells outside the core.

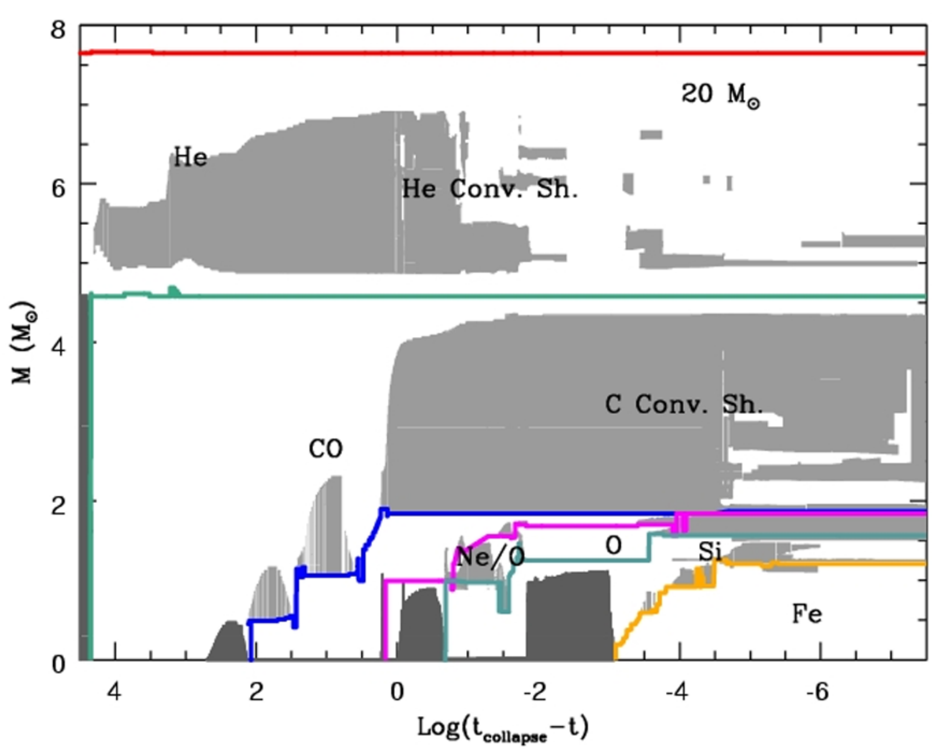

Figure 2.1: Kippenhan diagram for the evolution of a 20 $M:\odot$ star, taken from [11]. The solid colored lines mark the nuclear burning shells, while the gray shaded areas correspond to the convective regions.

2.1.2 Wolf-Rayet stars

Wolf-Rayet (WR) stars are hot and luminous stars that represent a normal stage of life for massive stars; they get their name from the two French astronomers Charles Wolf and Georges Rayet, who discovered these stars in 1867. Their most distinctive characteristic is represented by their very intense stellar winds, that expel a considerable amount of material into the interstellar medium, that can reach speeds exceeding 2000 km/s. Due to this intense mass loss, these stars lose a substantial amount of their external envelope, exposing their hot and chemically enriched internal layers, that contain elements such as Helium, Carbon, Nitrogen, and Oxygen. Due to the stripping of the envelope, usually a distinctive lack of Hydrogen in the spectrum is shown by these stars.

The exposed structure produces very peculiar spectra. Their emission is dominated by optically thick lines, differently from the ones of ordinary stars, while generally lacking absorption lines, except in some cases where a stellar companion is present. On the basis of the chemical composition detected in their spectra, it is possible to classify WR stars into different groups, that can be interpreted as an evolutionary sequence of exposure of deeper layers of the stars. WR stars come in three major subtypes:

1. **WN - Nitrogen kind**: distinct presence of Helium and Nitrogen in the spectrum, but younger stars still have partially retained their Hydrogen envelope still fall in this class, under the name of WNh. They are further subdivided in subclasses from WN3 to WN9, based on highest to lowest excitation of Helium, so that lower numbers correspond to higher temperature and ionization. Two more different kinds can be identified within this class, namely WNL, that have an amount of Hydrogen consistent with equilibrium values from the CNO-cycle, and WNE, that lack Hydrogen completely. In general these stars are considered to be at the beginning of WR phase during the star's life.

2. **WC - Carbon kind**: have a total lack of Hydrogen and little to no Nitrogen, showing a strong and distinct presence of Helium and Carbon lines lines, features consistent with partial He-burning. They are further classified in groups from WC4 to WC9, depending on ratios of carbon ions with respect to oxygen ions, and show lower temperature for higher numbers.

3. **WO - Oxygen kind**: the rarest and hottest among WR stars, they represent the final stage before supernova explosion. Because they are in such an advanced stage, the envelope stripping exposes the product of He-burning into Oxygen, whose emission lines dominate the spectrum, even if still showing the presence of Carbon and Helium, making them similar to WC. This chemical composition is expected as the star has almost reached completion for He-burning. The labels for WO range from WO1 to WO4, depending on the strength and the kind of the dominant oxygen lines.

2.1.3 Supernova explosion and final fates

After reaching the Chandrasekhar mass limit, the core begins a rapid collapse, that lasts only a few milliseconds, dramatically increasing its temperature and density. At this time, photodisintegration of iron-group nuclei occurs via electron capture, removing a significant amount of free electrons. When extreme nuclear densities are reached, neutrons are produced via the electron capture process. This process is described by $p^+ + e^- \to n + \nu_e$, and frees a massive amount of neutrinos, which end up escaping from the star.

When the core reaches densities of the order of $\rho \sim 10^{12} g/cm^3$ a change in the physics of the collapse occurs. Indeed, the plasma becomes opaque to neutrinos, which are no longer able to travel directly out from the star, but are able to escape only after many scattering events. The surface under which neutrinos end up being trapped is usually referred at as *neutrinosphere*. In these conditions, the collapse proceeds substantially in a homologous way, with the core becoming increasingly more compressed and the formation of neutrons going on, until densities of the order of the nuclear one ($\rho \sim 10^{14} g/cm^3$) are reached in the core.

At this point, since nuclear matter has a reduced compressibility, the collapse decelerates, and the infalling matter bounces on top of the hard core, generating a shock wave that starts propagating outwards, towards the external layers of the star. The shock generated by matter bouncing on top of the core was thought to be sufficient to trigger a supernova event in the past decades, and was known as *Prompt mechanism*. Even if the exact physical mechanism of the supernova (SN) explosion and the ”ingredients” needed for it to happen are still uncertain to this day, the prompt mechanism was proven to be insufficient for triggering a SN event mainly due to the massive energy losses suffered by the star because of neutrinos escaping: indeed about 90% of the collapse energy is lost in this way.

A different and more realistic explanation for this process might be the so-called *delayed neutrino heating mechanism*. In this case, the shock wave loses energy due to the insufficient push coming from the bounce on the hard core, and stalls at about a hundred solar radii from the center. In order to revive this wave and achieve the explosion, it is necessary to find a new energy source that, in this case, is constituted by the trapped neutrinos in the core. These neutrinos are able to revive the shockwave by acting like a ”hot bubble”, increasing the pressure behind the shock, driving it outward again.

However, it should not be taken for granted that, after the revival of the shock, an explosion will certainly occur. Indeed, it might happen that either in some cases the explosion might fail and a direct collapse happens, forming a black hole, or it is possible that part of the material does not receive enough kinetic energy to be ejected like in a standard supernova explosion. Indeed, this material might get trapped in the potential well of the newly formed compact object, giving rise to the phenomenon known as *fallback*.

In order to try and predict how a star will behave as a supernova, it is possible to define the probability of said star to explode, also known as *explodability*, which is highly sensitive to presupernova configuration. However, even knowing this parameter does not ensure that the final fate of the examined star is fully known. Indeed, for stars with initial mass between approximately 15 and 40 solar masses, the fate is particularly difficult to predict, with *islands of explodability* and a strong dependence on the final presupernova structure.

The final fate of massive stars is largely determined by their initial mass, which can lead the star towards different types of compact remnants or to complete destruction. Anyway, it is fundamental to understand that the final fate is not only influenced by the initial mass, but also from other factors such as stellar metallicity, rotation, and binary interactions. On top of this it is necessary to take into account also uncertainties regarding the modeling of physical processes like internal mixing ans stellar winds. In an attempt to summarize the different kinds of final fates achievable by the stars and the dependence of the final mass on the initial one and metallicity it is possible to consider Figure 2.2.

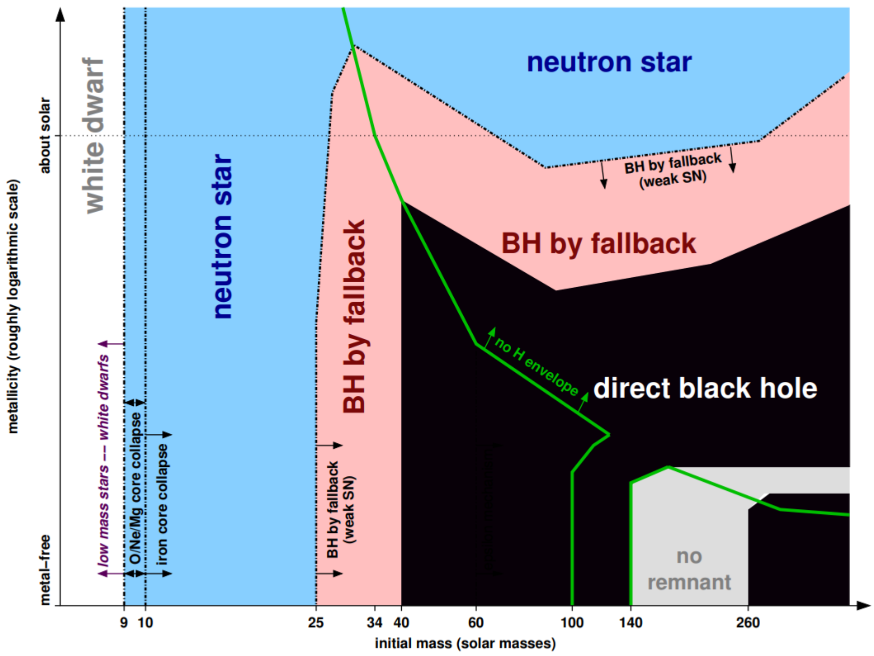

Figure 2.2: Final fates of massive stars depending on the initial mass of the progenitor and on metallicity, taken from [10]. White dwarves are indicated by the white area, blue shading represents neutron stars, red shading shows black holes forming by fallback, distinguishing them from black holes forming from direct collapse (in black in the figure). Finally, in the gray shaded area are represented the stars that explode leaving no remnant. The green line marks the threshold where the strong mass loss may remove the Hydrogen rich envelope before the explosion of the star as a supernova.

2.2 Stellar rotation and Core overshooting

Stellar rotation is a crucial feature that has the power to deeply influence the evolution of massive stars, altering their vital cycle even from the earliest stages of evolution. Firstly, rotation induces a geometrical distortion in the shape of the star, making it oblate (so squeezed at the poles and enlarged at the equator) due to the centrifugal force that reduces the effective gravity at the equator. This difference in the effective gravitational pull generates the Von Zeipel effect [12], also known as *gravitational darkening*, that makes the poles of the star appear hotter and brighter than the equator.

In the analysis of this work, the stellar rotation is expressed as a fraction of the critical rotational speed, indicated with $\Omega_{crit} = \sqrt{GM/R^3}$: this is defined as the limit in angular rotational speed at which the centrifugal force is equal to the star's gravitational pull at the equator. If the speed increases above this limit, the star starts losing matter because gravity is no longer able to pull it together and resist the centrifugal forces.

Moreover, the reduced effective gravity introduces another important effect: the increase in the mass loss rates via stellar winds. Since matter is less bound to the surface, it gets stripped away more easily. This enhancement effect is usually accounted for by a multiplicative factor in stellar evolution models. An example of this multiplication factor is taken by [13], and is calculated as follows:

$$\frac{\dot{M}(\Omega)}{\dot{M}(\Omega=0)} = \frac{(1-\Gamma)^{\frac{1}{\alpha}-1}}{\left(1-\Gamma-\frac{4}{9}\left(\frac{v}{v_{\text{crit}}}\right)^2\right)^{\frac{1}{\alpha}-1}} \tag{2.6}$$

where $\Gamma = \chi\, L/(4\pi\, G\, c\, M)$ is the total Eddington parameter (χ being the total opacity), $\alpha = 0.52$ and $v_{\rm crit} = [2\, G\, M/(3\, R_{\rm pb})]^{1/2}$, where $R_{\rm pb}$ is the polar radius at break up.

An effect that needs to be accounted for is the extra mixing in the radiative zones of the star. This mixing transports nuclear products from the core towards the external layers of the star and brings in fresh fuel to the core. This might prolong the life of the star, increase its luminosity, and enrich the surface with heavier elements.

In case of a very high rotational speed and relatively low metallicity, like the one treated in this work, rotation can induce a chemically homogeneous evolution, that prevents the star from expanding and cooling into a supergiant, while moving the evolutionary path towards hotter regions with higher luminosities. In this scenario, the star is almost completely homogeneous and stays more compact, influencing deeply the compactness parameter, which can have a huge impact both on the explodability of the star and the mass of the remnant.

Finally, the last effect (but not for importance) is the increase in dimension of the core, that translates into a higher stellar luminosity, possibly leading to more massive remnants.

As demonstrated in [14], it is possible to see the difference in evolution on the HR diagram of Figure 2.3, with tracks computer at SMC metallicity. The rotating stellar tracks are significantly hotter and more luminous than the non-rotating ones, resulting in stars that are likely to get more stripped than their non-rotating counterparts.

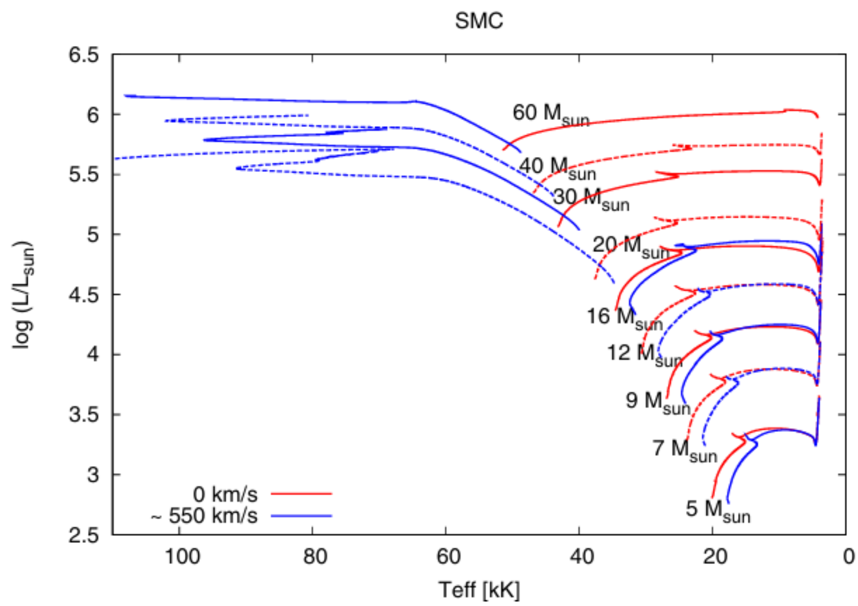

Figure 2.3: HR diagrams for rotating and non rotating stars, taken from [14]. The shown stellar tracks have been computed for non-rotating (red) and fastly rotating at 550 km/s (blue) stars.

Another fundamental process in stellar evolution is represented by convective overshooting. This process happens when convective cells, due to their inertia, penetrate beyond the boundary defined by an instability criterion (such as the Ledoux criterion) and extend into otherwise stable regions, such as radiative zones. To parameterize this effect, a numeric factor is usually employed, which represents the extent of the space traveled by convective cells in units of the pressure scale height.

In this work, the exponential overshooting by Herwig 2000 [15] has been chosen to describe the overshooting above the convective regions. The diffusion coefficient in the overshooting region can be calculated using the following equation.

$$D_{\mathrm{OV}} = D_0 \exp\left[-\frac{2(r - r_0)}{f_{\mathrm{OV}} H_P}\right] \tag{2.7}$$

where D_0 is the diffusion coefficient at the starting point of the overshooting region, which is defined at a radius r_0, just below the convective boundary. Finally f_{OV} defines the inverse slope of diffusion decay expressed in terms of the height of the pressure scale H_P. The value of f_{OV} chosen for this work is $f_{\mathrm{OV}} = 0.03$.

The consequences of this process are significant for massive stars' evolution. Indeed, just like rotation, overshooting tends to increase the effective dimension of the core, introducing fresh Hydrogen in the core. This effectively increases the duration of the main sequence phase, and brings nuclear products to the outer layers, enriching the surface material. Similarly to rotation, overshooting also increases the luminosity and effective temperature, and increases the compactness of the star.

Despite the huge progress made in the study of both stellar rotation and core overshooting, the modelization of these characteristics of the star, is still extremely complex and subject to uncertainties, despite the adoption of some approximations. Indeed, there is still a constant need for calibration with observational data.

Chapter 3

Line-driven winds

Throughout their life, stars experience mass loss episodes in the form of stellar winds, outflows of gas ejected from the external layers of a star's atmosphere. Stellar winds dramatically decrease the initial mass of the star through its evolutionary path, and their nature depends on the star type.

There are numerous different wind mechanisms. Among all, the most frequently observed kinds are dust driven winds - mainly found in cooler stars, based on the transfer of momentum from radiation to dust particles (the so-called "two stage rocket") - and line driven winds, main focus of this work, described in detail in the next section.

3.1 CAK theory

The most common wind type in massive stars is represented by line-driven or radiation-driven winds. The underlying mechanism driving these matter outflows is based on the transfer or momentum of the stellar radiation to the gas above the photosphere, which is ideal for hot, bright massive stars.

It is possible to express the ratio between gravitational force and radiative force through the electron scattering Eddington parameter, as a function of the mass M and the luminosity L of the star.

$$\Gamma_e = \frac{\kappa_e L}{4\pi c G M} \tag{3.1}$$

In the condition of fully ionized gas, it is possible to approximate the electron scattering opacity κ_e as $\simeq 0.2\,(1+X_s)$ cm^{2}g^{-1}, where X_s is the hydrogen surface abundance. The equation above, in these conditions, becomes $\Gamma_e \simeq 10^{-4.183}(1+X_s)\dfrac{L}{M}$.

Until half of the 20th century, the mathematical description of stellar winds has been fairly uncertain, specifically for hot massive stars. In 1975 Castor, Abbot and Klein developed a theory [16] - today known as CAK theory - that marked an important turning point in describing how radiation pressure could accelerate matter in the external layers of the star, generating a stable supersonic stellar wind. In order to understand this theory, it is essential to recognize the basic mechanism that allows a star to expel matter in the form of wind.

In hot massive stars, the main source of energy capable of driving this process is radiation, acting on the gas through radiation pressure, differently from other kinds of stars where thermal pressure or magnetic fields could be dominant.

In a very luminous star, photons emitted from the photosphere carry momentum, and when they interact with matter in the external layers of stellar atmosphere, they can transfer part of this momentum to matter.

In the simplest case, photons get scattered by free electrons (Thomson scattering), exerting a constant radiation pressure opposed to gravity. However, this pressure, even if present, is generally too weak to explain the high speeds and high mass-loss rates observed in O-B stars. Indeed, this radiation can sustain the stellar structure against gravitational collapse, but is not enough to win the gravitational pull and accelerate stellar material outwards. For this reason, the radiative contribution driving winds in massive stars is given by spectral lines, produced by atomic and ionic transitions. These transitions provide much greater opacity, but with the main downside of being very selective in terms of frequency bands.

The innovation of Castor, Abbott, and Klein's approach consists of recognizing that radiation does not act only through interaction with free electrons, as in the case of continuum radiation, but can exert a far more effective push on the gas through absorption on spectral lines, linked to the presence in the atmosphere of elements heavier than hydrogen. Indeed heavier elements, also called "metals", are present in small amounts even in the external layers of the star and can absorb photons in very precise frequency bands, corresponding to their electronic transitions.

When a photon gets absorbed on a spectral line, the momentum associated to that photon gets transferred to the atom or ion that absorbed it. When thousands of those lines are at play, the total force exerted by radiation can become several times greater than the one due only to Thomson diffusion, overcoming the gravitational pull and accelerating matter outward. Integrating this momentum transfer over all the scatterings results in a radially directed total line acceleration, also known as g_{rad}^{line} [17] This mechanism, also known as line-driving, is the pivot of CAK theory. However, in order to describe it in a quantitative way, it is necessary to introduce some approximations and mathematical formalisms.

Firstly, in this theory, Sobolev formalism is adopted. In fast stellar winds, the speed of the gas changes very rapidly with the radius, thus generating a high-speed gradient. This implies that photon-particle interactions occur in a very small timescale. After this timescale, radiation is no longer in resonance with the transition, due to Doppler shift. Sobolev formalism allows to treat the radiative phenomenon as local, assuming the spectral line to be shaped like a delta function and dramatically simplifying calculations for the total radiative force.

In general, when a photon gets absorbed or re-emitted by an ion, the transferred momentum is proportional to $h\nu/c$. In a very hot star - like a massive star - the high electromagnetic emission can efficiently accelerate matter in the external stellar layers to high speeds, up to thousands of km/s.
A photon can be either absorbed or emitted by an ion; even if there are many different kinds of processes at play, 4 of them hold a larger contribution and are summarized below:

- **Line scattering**: a photon gets absorbed and then re-emitted in the same atomic transition - thus keeping the same frequency
- **Line emission by recombination**: an ion collides with an electron that gets recombined and emits photons while being de-excited to a lower energy level
- **Collisional or photo-excitation line emission**: an electron inside an atom gets excited to a higher energy level either due to collisions or to the absorption of a photon, and then re-emits photons while de-exciting to a lower energy level
- **Masering by stimulated emission**: a photon hits an excited electron; the atom then

de-excites, producing a photon at the exact same frequency and direction as the original photons, resulting in two photons at the same frequency traveling in the same direction

The mechanism works as follows: radiation produced by the star is absorbed by ions in the outer layers of the star, and their electrons get excited to higher energy levels. After some time, the electrons in more energetic and unstable levels start to undergo de-excitation, thus re-emitting the photons they previously absorbed. The newly emitted photons, usually with a different frequency, are now freed in the plasma, and can excite other ions or atoms.

The majority of the elements in the stellar atmospheres have their strongest lines in the UV band. However, the portion of stellar flux in the far UV band is reduced, making it difficult for radiation-driven winds to rely only on the pressure due only to these lines. Indeed, taking into account only the few ions accelerated directly by UV photons, the amount of mass lost is extremely small and does not reproduce the observed high values in massive stars.

The solution to this problem is given by the combination of two different processes: Doppler shift of photons and repeated scattering of photons in the plasma. Indeed, Doppler shift is able to change the value of the frequency perceived by the ions they are traveling toward, making it possible for these ions to absorb photons that, in the star's frame, have a frequency different from the one needed for the transition. This effect, coupled with the frequent repeated absorption and emission of photons in the gas, is capable of increasing the speed of both ions and other particles present in the ionized plasma - protons and electrons - through Coulomb interactions [17]. This finally results in an overall acceleration of the material, which gets drawn progressively further from the star.

In order to understand how these processes contribute and how this kind of wind works, it is necessary to make some basic assumptions: let us consider homogeneous, stationary and spherically symmetric winds. These assumptions can be justified as long as rotation and magnetic fields can be neglected [17]. From these assumptions, some basic equations can be derived to describe the wind.

1. **Mass continuity equation**: the total mass lost through a spherical shell of radius r surrounding the star is conserved

$$\dot{M} = 4\pi r^2 \rho(r) v(r) \equiv -\frac{dM}{dt} > 0 \tag{3.2}$$

   where ρ is the density, v is the velocity of the gas, and r is the radial coordinate in the star's system.

2. **(Stationary) momentum equation**:

$$v\frac{dv}{dr} = -\frac{GM}{r^2} - \frac{1}{\rho}\frac{dP}{dr} + g_{rad} \tag{3.3}$$

   where P is the gas pressure, G is the gravitational constant and M is the total mass of the star. In this equation, the gravitational acceleration is directed inward, the pressure term is directed outward, and $g_{rad} = g_{rad}^{line} + g_{rad}^{continuum}$ indicates the total radiative acceleration term.

3. **Equation of motion**:

$$\left(1 - \frac{a^2}{v^2}\right) v\frac{dv}{dr} = \frac{2a^2}{r} - \frac{da^2}{dr} - \frac{GM}{r^2} + g_{rad} \tag{3.4}$$

where $a = \sqrt{\frac{RT}{\mu}}$ is the isothermal speed of sound, T is the temperature of the gas, R is the gas constant and μ is the mean molecular weight. The equation is obtained by combining the mass continuity equation to the equation of state $p = a^2\rho$

According to CAK theory, it is possible to write the total force due to lines as a function of the total flux $F = L/4\pi r^2$ in the following way [16]:

$$f_{rad} = \frac{\kappa_e F}{c}\mathcal{M} \tag{3.5}$$

where the first factor is the force due to continuous absorption, and the second one, $\mathcal{M}(t)$, is the force multiplier function. The latter expresses the effect of the lines as a function of an optical depth variable independent of line strength, $t = \kappa_e \rho v_{th}/(dv/dr)$, where ρ is the gas density and v_{th} is the thermal velocity of the gas.

The force multiplier function can be written as

$$\mathcal{M}(t) = kt^{-\alpha} \tag{3.6}$$

where k and α are the force multiplier parameters. In [16], the accepted values for these parameters are: k $\simeq 1/30$ and $\alpha \simeq 0.7$.
The aforementioned force multiplier parameters are quantities used to summarize the cumulative effect of thousands of spectral lines:

- α: is the steepness of the slope representing line intensity distribution, thus controlling the balance between strong and weak spectral lines. For high values of this parameter, the wind is dominated only by few strong lines, otherwise there is more participation of weak lines. In general, this value quantifies the ratio of line acceleration from optically thick lines to total radiative acceleration and can be expressed as $\alpha = g_{rad}^{thick}/g_{rad}^{tot}$.
- k: is a coefficient that measures the numerical density of strong spectral lines and their ability to contribute to the radiative force. High values of k mean a higher wind efficiency. Indeed, k, as stated in [17], is proportional to the flux-weighted number of lines stronger than Thomson scattering, and is interpreted as the fraction of flux that would already be blocked in the photosphere if all lines were optically thick. From [18] it can be seen that k $\propto Z^{1-\alpha}$, where Z is the metallicity of the gas.
- δ: has been introduced in an extended version of the CAK model, to account for the dependency on the ionization stage of the gas with respect to the local density, so how many lines are actually available. It is particularly important when the wind has strong temperature or opacity variations. Under typical O star conditions, it is of the order of $\simeq 0.1$, and is used to calculate the effective α, α', as $\alpha' = \alpha - \delta \simeq 0.6$.

The final equation for gas velocity, obtained considering all the equations above and the assumption of a stationary, spherically symmetric wind, is the following one [16]:

$$\left(1 - \frac{a^2}{v^2}\right) v\frac{dv}{dr} = \frac{2a^2}{r} - \frac{da^2}{dr} - \frac{GM(1-\Gamma_e)}{r^2} + \frac{GM\Gamma_e k}{r^2}\left[\frac{4\pi}{k_e v_{th} dM/dt}\right]^{\alpha}\left(r^2 v\frac{dv}{dr}\right)^{\alpha} \tag{3.7}$$

Due to the complex dependency on dv/dr, the equation is non-linear, and this implies the existence of a critical point, where the equation becomes singular unless a regularity condition is satisfied. The solution is required to be physically acceptable and regular in correspondence with the critical point. This selects a particular configuration of the flux, uniquely defining the mass-loss rate value, which can no longer be chosen arbitrarily. The result is the famous relation of CAK theory for the mass-loss rate [16], that can be written as follows:

$$\frac{dM}{dt} = \frac{4\pi GM}{\kappa_e v_{th}} \alpha (1-\alpha)^{\frac{1-\alpha}{\alpha}} k^{\frac{1}{\alpha}} \frac{\Gamma_e^{\frac{1}{\alpha}}}{(1-\Gamma_e)^{\frac{1-\alpha}{\alpha}}} \tag{3.8}$$

3.2 Optically thick wind models

Classical wind models like CAK theory describe optically thin wind models, where gas is transparent to continuum radiation. In these models, wind acceleration is due to the radiation pressure absorbed and emitted by a significant amount of spectral lines. Even being an incredibly advanced theory for its time, CAK theory presents some limitations, mainly due to the strict, even if necessary, assumptions made.

For instance, the approximation of the wind behavior as a spherically symmetric flow has been proven to be imprecise, due to turbulences, clumping, and internal shocks. Moreover, the distribution of lines is too simplified, and dependencies on temperature, metallicity, and ionization have to be taken into account. In addition to this, CAK theory only considers cases where stellar rotation and magnetic fields are negligible with respect to the other forces at play.

The greatest limitation in optically thin wind models is constituted by the *single-scattering limit*. In this configuration, photons are assumed to interact and transfer momentum only once. However, in very luminous stars this assumption is no longer valid, particularly the gas can become optically thick in continuum radiation if the gas density is sufficiently high. In this case, since the gas appears to be opaque to photons, radiation gets absorbed and re-emitted multiple times, transferring a substantial amount of energy to the gas. In this case, radiation pressure has contributions that belong not only to lines, but also to continuum radiation. In this way, the acceleration can grow to be much bigger than the one predicted by optically thin models.

Although an increase in the strength of the mass loss is already expected from the CAK, when the Eddington parameter is close to the Eddington limit (i.e. when $\Gamma_\mathrm{e} \approx 1$), Vink et al. 2011 [19] found a significant change in the slope of the $\dot{M}$ for high values of Γ_e. The trend found in that paper is very steep, with $\dot{M} \propto \Gamma_\mathrm{e}^{4.77}$. The change in the $\dot{M}(\Gamma_\mathrm{e})$-behavior can be related to a switch from an optically thin to an optically thick wind regime.

A change in the spectral appearance of the star is also present, from Of to WNh-type, even on the main sequence. These stars end up being classified as WRs even on the main sequence due to their spectra, independent on their evolutionary status, as seen in [20], [21]. A study that used this spectral change is that of Bestenlehner et al. 2014 [**?**], where the transition regime was studied from an observational point of view. This study ended up confirming the findings of [19] based on Monte Carlo wind models.

In Bestenlehner 2020 [22], the switch from the optically thin to the optically thick regime was also found by fitting observed values of the mass loss found for the R136 cluster in the Large Magellanic Cloud, where a new wind recipe was proposed. This work is focused on the study and implementation of the wind model developed by Bestenlehner 2020 [22], which will be treated in more detail in Section 3.2.1.

Interestingly, wind recipes that rely on the switch mechanism introduced above, can generate an optically thicker and slower wind but with significantly higher mass loss, which produces hotter and more luminous stars. This could provide a tentative solution to the Humphrey-Davidson (HD) limit problem.

HD limit problem

The main limitation of CAK theory stellar winds is the fact that they consider only optically thin lines, thus being considered among the optically thin wind models. This issue is directly related to another existing problem: the theoretical overpopulation of overluminous supergiants inside the HD limit.

The HD limit is an empirical limit first theorized by Humphrey and Davidson in 1979 [23], over which very few cool very luminous stars are observed. More specifically, over a certain luminosity (typically $\log(L/L_\odot) \gtrsim 5.8$), either stars are not able to maintain an extended cool structure and do not appear as red supergiants, or spend very little time in that condition, thus reducing the number of observations at those luminosity and temperature. This limit is usually interpreted as a threshold over which mass-loss mechanisms become extremely effective and prevent the star from evolving towards lower temperature regions in the H-R diagram.

The main problem with this observational lack of stars in the HD limit region of the H-R diagram is due to the overproduction of cool supergiants inside the HD limit made by theoretical star models, as studied in [8]. This overproduction could be due to wrong prescriptions for the mass-loss rate. Indeed, theoretical models that employ optically thin winds, like CAK theory or its extensions, very often result in winds definitely not able to strip the stars enough for them to get rid of their envelope. The resulting stars, instead of becoming Wolf-Rayet stars, end up dying within the HD limit.

Iorio et al. 2023 [24] offers a good representation of the evolution of stars on the HR diagram employing mostly optically thin wind prescriptions, shown in Figure 3.1: all the stars end their lives in the cool region of the HR diagram as inflated supergiants at these metallicities (nearest to the ones used in this study).

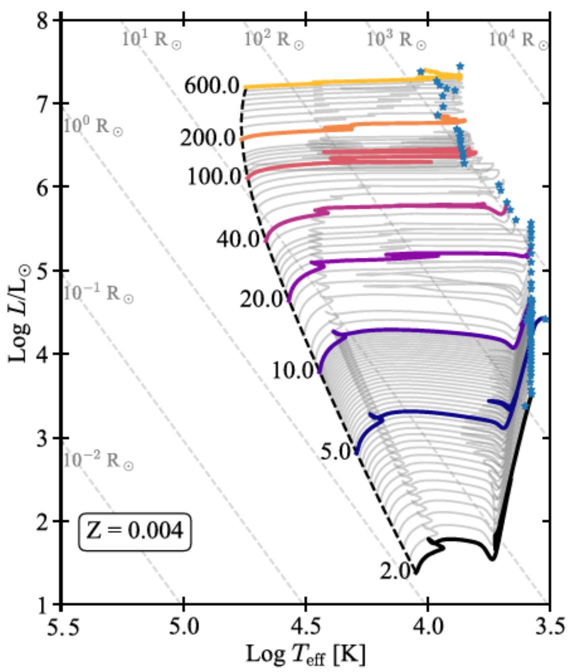

Figure 3.1: HR diagram with evolutionary tracks of stars with optically thin wind prescriptions, taken from [24], The stellar tracks for the various initial masses are represented with differently colored lines, while the beginning of the main sequence phase is a black dashed line.

The fundamental issue is that evolutionary models with optically thin winds produce a large number of stars in a region of the H-R diagram that hosts little to no observations. This discrepancy suggests that wind models based only on optically thin mechanisms do not correctly grasp all the dominant processes in these regimes. Possible solutions could be, for instance, the integration of non-radiative mechanisms, like rotation or magnetic fields, the introduction of optically thick wind models or a combination of the two.

3.2.1 Bestenlehner 2020 wind model

The model studied and implemented in this work has been taken from the paper by Bestenlehner 2020 [22]. The main focus of this wind model was to provide a simple recipe that, without implementing complex features of the wind, is still able to describe the mass loss of stars situated in the R136 cluster. This cluster is a starburst region at the center of the Tarantula Nebula in the Large Magellanic Cloud (LMC). The main strength point of this recipe lies in its implementation. Indeed, Bestenlehner's mass loss relation is actually an extension of CAK theory, providing a simple yet effective relation for the estimation of stellar winds in both optically thin and optically thick regimes.

As already seen by comparing CAK predictions with observations, this theoretical model, despite reasonably agreeing in optically thin wind regimes, largely disagrees in the optically thick wind regime, as seen by [25]. The strategy adopted to correct for this disagreement is the following:

1. Consider the CAK theory wind model:

$$\dot{M} \propto M \frac{\Gamma_e^{\frac{1}{\alpha}}}{(1-\Gamma_e)^{\frac{1-\alpha}{\alpha}}} \tag{3.9}$$

2. Make three key assumptions:

   a. The energy transport in the star is assumed to be fully radiative

   b. The total pressure P consists of the sum of gas pressure P_{gas} of a fully ionized ideal gas and the radiation pressure P_{rad}

   c. The ratio of gas pressure to total pressure $P_{gas}/P = \beta$ is constant throughout the star

3. Considering the previous assumptions, it is possible to replace the stellar mass term in CAK with the following stellar mass - Eddington parameter relation, using the Eddington stellar model for radiative stars.

$$M = \mathcal{C}\frac{1}{\mu^2}\frac{\Gamma_e^{1/2}}{(1-\Gamma_e)^2} \tag{3.10}$$

   where

   - μ is the mean molecular weight, and $\mu^{-1} \simeq 2\,X + 0.75\,Y + 0.5\,Z$ with the chemical composition of Hydrogen(X), Helium(Y) and metals (Z) in mass fraction

   - $\mathcal{C}$ is a factor including all the constants, and is equal to

$$\mathcal{C} = -\frac{2}{G^{3/2}}\left(\frac{3c}{\sigma\pi}\right)^{1/2} R^2\xi_1^2\left(\frac{d\theta}{d\xi}\right)_{\xi=\xi_1} \tag{3.11}$$

where G is the universal gravitational constant, c is the speed of light, σ is the Stefan-Boltzmann-radiation constant, R is the universal gas constant and $\xi_1^2 \left(d\theta/d\xi\right)_{\xi=\xi_1} \simeq -2.01824$ is the Lane-Emden constant

4. Combining the previous relation for the mass with the mass loss recipe derived in CAK theory, the final result is Bestenlehner's recipe

$$\dot{M} = \mathcal{C}\frac{4\pi G}{\kappa_e v_{th}}\frac{1}{\mu^2}k^{1/\alpha}\alpha(1-\alpha)^{(1-\alpha)/\alpha}\frac{\Gamma_e^{1/\alpha+1/2}}{(1-\Gamma_e)^{\frac{1-\alpha}{\alpha}+2}} \tag{3.12}$$

where k and α are the force multiplier parameters defined in the CAK theory.

This recipe depends on a series of constants, on stellar parameters, such as temperature and chemical composition, on the CAK force multipliers, and on the Eddington parameter. To make it more manageable, the wind model can be written by regrouping some of the constants into a new term, $\dot{M}_0$, so that the final result, used in this thesis and in the original work, is

$$\dot{M} = \dot{M}_0\,\frac{\Gamma_e^{1/\alpha+1/2}}{(1-\Gamma_e)^{\frac{1-\alpha}{\alpha}+2}} \tag{3.13}$$

In order to distinguish between the optically thin and thick regimes, a transition point is considered, indicated with $\Gamma_{e,T}$. Considering the indications given by Bestenlehner's work itself, this transition point is to be determined by solving the following equation

$$\Gamma_{e,T}^{1/\alpha+1/2} = (1-\Gamma_{e,T})^{\frac{1-\alpha}{\alpha}+2} \tag{3.14}$$

In the code I wrote to implement this wind recipe in MESA, this equation is solved via the bisection method.

In Figure 3.2 is shown the main result from Bestenlehner 2020 [22], displaying the evolution of his new mass loss recipe, calibrated on the WNh of the R136 cluster in the LMC, on top of the population of O-stars in the same cluster.

Normalization of the wind recipe

In order to be actually used in stellar evolution codes, this model needs to be normalized (i.e., $\dot{M}_0$ needs to be determined). The original author decided to do this empirically, considering the so-called *slash stars*, a particular class of massive stars that lay at the spectral transition point between massive O stars and Wolf-Rayet stars, thus being considered the reference for the switch between optically thin and optically thick stellar winds. In Bestenlehner's work, the mass loss rate of the *slash stars* in the R136 cluster is observed and then the wind model has been normalized such that the mass loss rate at the switch point is equal to the mass loss rate of the considered stars.

Indeed, the author firstly rewrites his original formula as done in the previous section, considering $\dot{M}_0$ as a normalization term. Then he subsequently takes this term as a parameter and performs a fit to the observed values for the mass loss of the stars in the considered cluster, thus obtaining a tailored value of $\dot{M}_0$ for this cluster. In such conditions, this method actually works, because in the LMC there is at least one star with the required spectral characteristics, laying in the transitional region between optically thin and optically thick winds.

The main concern with this approach arises when trying to generalize this recipe to groups of stars at metallicities different than the one of the LMC, like in the case of the SMC.

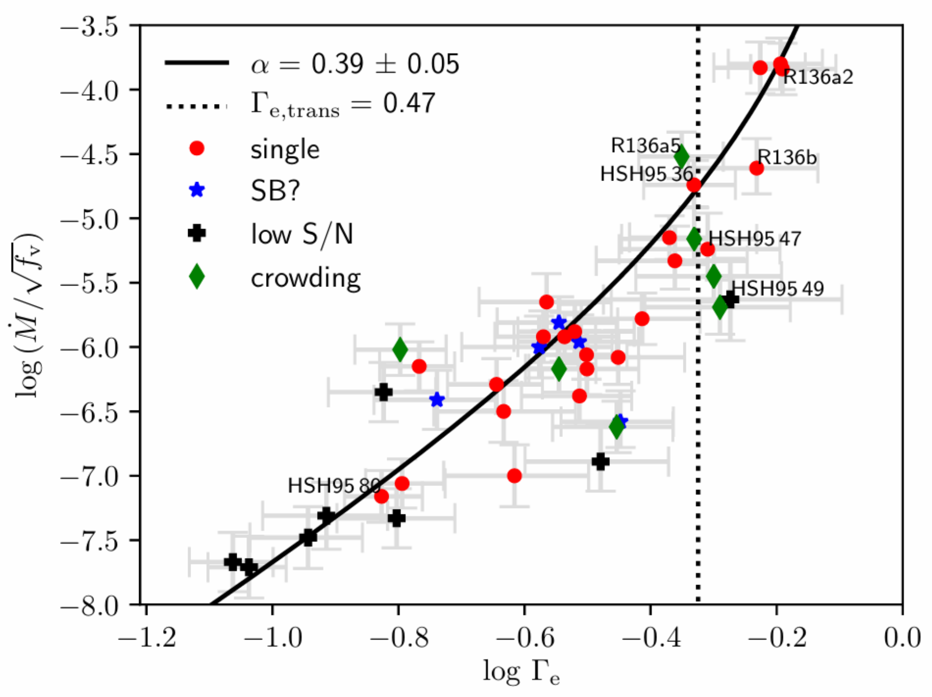

Figure 3.2: Fit of the mass loss recipe by Bestenlehner 2020 [22] on the observational points of the R136 cluster in the LMC. The fit for the wind recipe is indicated with a solid black line. The transition point in Γ_e from optically thin to optically thick winds is represented by a vertical dotted line. Finally, with different markers are represented the stellar parameters for stars in the R136 cluster.

Indeed, observing the SMC, as of now the presence of *slash stars* has not yet been registered, making it impossible to normalize the recipe as done and suggested by the original author.

In order to obtain a consistent yet simple implementation in the 1D stellar evolution code MESA (version r12115 [26], [27], [28], [29], [30]) a normalization based on metallicity dependencies was considered. In Bestenlehner's recipe, indeed, some of the terms can vary with metallicity and have a significant impact on the wind normalization.

In order to normalize, accounting for both the empirical results obtained by the original author, and extending the prescription at different metallicities, the procedure was the following:

1. Find the most recent reference value of $\dot{M}_0$ at LMC metallicity in [31], indicated as $\dot{M}_0(Z = Z_{LMC})$
2. Normalize the dependency on metallicity of force multiplier parameter k [18], to a generic value of metallicity indicated with Z_1; the factor containing this dependency will then be

$$\frac{k(Z_1)}{k(Z_{LMC})} \propto \left(\frac{Z_1}{Z_{LMC}}\right)^{1-\alpha} \tag{3.15}$$

3. Normalize the dependency on metallicity of the mean molecular weight, adding a factor

$$\frac{\mu^2(Z_{LMC})}{\mu^2(Z_1)} \tag{3.16}$$

4. Normalize the dependency on Hydrogen abundance of the electron scattering coefficient

$\kappa_e \simeq 0.2(1 + X)$, obtaining a factor

$$\frac{\kappa_e(Z_{LMC})}{\kappa_e(Z_1)} \simeq \frac{(1 + X_{LMC})}{(1 + X_1)} \tag{3.17}$$

The final result for the normalization factor is the following one

$$\dot{M}_0(Z = Z_1) = \dot{M}_0(Z = Z_{LMC}) \left(\frac{Z_1}{Z_{LMC}}\right)^{\frac{1-\alpha}{\alpha}} \frac{\mu^2(Z_{LMC})}{\mu^2(Z_1)} \frac{(1 + X_{LMC})}{(1 + X_1)} \tag{3.18}$$

For some additional remarks regarding the choice of the normalization technique, see the dedicated section in the Appendix.

3.2.2 Effect of rotation and overshooting increase

As previously mentioned in the dedicated section, the introduction of rotation and core overshooting can generate an enhancement of the chemical mixing of the star, leading it towards a chemically-homogeneous evolution, increasing both temperature and luminosity. Since an enhanced luminosity produces higher Γ_e values, the activation of optically thick winds might depend substantially on rotation and overshooting.
For this reason, in this work their effect will be analyzed by generating models both for rotating and non-rotating stars.

3.2.3 MESA code and Simulation setup

The main code used for this work is MESA (Modules for Experiments in Stellar Astrophysics) version r12115 ([26], [27], [28], [29], [30]), a 1D hydrostatic stellar evolution code, used to simulate the life-cycles of stars and binaries. It enables detailed simulations of stellar structure and evolution across a broad range of stellar masses, metallicities, and evolutionary phases, from pre-main-sequence contraction to advanced nuclear burning stages, and in some cases, to core collapse or white dwarf cooling.

This code works by solving a series of differential equations describing the main processes driving stellar evolution, and accounting for a wide variety of effects like energy release through nuclear fusion, energy transport through radiation, convection and conduction, and mass loss due to different models of stellar winds. A stellar evolution code, like MESA, solves the differential equations by integrating them after being provided with a series of input parameters such as initial mass, rotational speed, chemical composition of the proto-star, that get evolved through the subsequent stages of its life.

MESA is built on a modular framework, which allows the user to adapt and customize different characteristics of the stellar evolution. An example of these would be the energy transport mechanisms, the convection processes, the net of nuclear reactions, and, finally, the mass-loss prescriptions. In addition to the different modules, MESA relies also on `inlist` files, namely a collection of built-in boundary conditions, parameters, and functions selected by the user to be employed in the evolution of the star. If needed, it is also possible to add customized and case-specific functions in the `run_star_extras` file. This was done in this work to implement the new wind model by Bestenlehner 2020 [22] and subsequently test it to reproduce the evolution of massive stars.

The setup used for the stellar evolution has a similar structure to the one published by Sabhahit et al. 2023 [32], available at: `https://github.com/Apophis-1/VMS_Paper2` with some of the modifications applied in Boco et al. 2025 [33] and Simonato et al. 2025 [34]. Regarding stellar winds, the setup used in this work is structured as follows:

- For temperatures $T_{eff} < 4000$ K, the used prescription is the one for red supergiants by de de Jager et al. 1988 [35];
- For temperatures in the range 4000 K $< T_{eff} < 10^5$ K, the newly implemented prescription by Bestenlehner 2020 [22] is used, both in the optically thin and optically thick regime;
- For temperatures $T_{eff} > 10^5$ K we use the maximum between the optically thick WR wind prescription by Sander & Vink 2020 [36] and Vink 2017 [37].

Finally, MESA will be used to produce a complete set of stellar tracks for two different metallicities ($Z = 0.003, 0.008$) and two values of the rotational rate per each metallicity ($\Omega/\Omega_{crit} = 0.0, 0.6$). These tracks will then be processed to be employed in the population sythesis code SEVN, treated more in detail in Section 4.5.1

3.3 MESA Results

In this section are shown the results of the performed simulations and the fundamental results of this work. The analysis have been performed for two different values of metallicity, respectively the one relative to the Small Magellanic Cloud, the main focus of this thesis, and the one of the Large Magellanic Cloud, used as a comparison. A fine grid in metallicity is beyond the scope of this work and is deferred to future studies.

All single stellar models have been run assuming two different initial stellar rotation rates, expressed as fractions of the critical angular velocity, $\Omega_{\rm crit}$. Specifically, we adopt $\Omega/\Omega_{\rm crit} = 0.0$ and 0.6 (corresponding to an initial rotational velocity of v_{rot}450 km/s), in order to explore the extrema of the parameter space in terms of rotational velocity. These values were chosen to assess how rotation affects stellar winds and evolutionary pathways.

3.3.1 HR diagram and wind composition

Here are presented the HRD for some of the computed stellar tracks, highlighting the burning stages with different colors and the optical thickness of the wind with different line styles.

SMC results
In this section are shown the results for simulations set considering an environmental metallicity equal to the one of the SMC. Two different plots are presented: in the first plot the stellar tracks have been computed considering a non-rotating star, while in the second one the star is assumed to rotate with $\Omega/\Omega_{crit} = 0.6$. The order will stay the same for the whole analysis.

A comparison of Figure 3.3 and Figure 3.4 shows numerous differences in the behavior of the stars on the HRD. In Figure 3.3, the stars mostly reflect the evolution observed in other models considering optically thin winds. Indeed, the majority of massive stars on the lower end of the mass spectrum ($M_{ZAMS} < 60 M_\odot$) avoid activating the optically thick mass loss recipe and therefore appear as significantly colder.

These characteristics, typical of stars with optically thin winds at relatively low metallicities, show that in such conditions stars are unable to peel off their stellar envelope, making them evolve towards the colder side of the HR diagram after completing the main sequence, entering the HD limit region and usually dying there. In the case of Figure 3.3, only the most massive

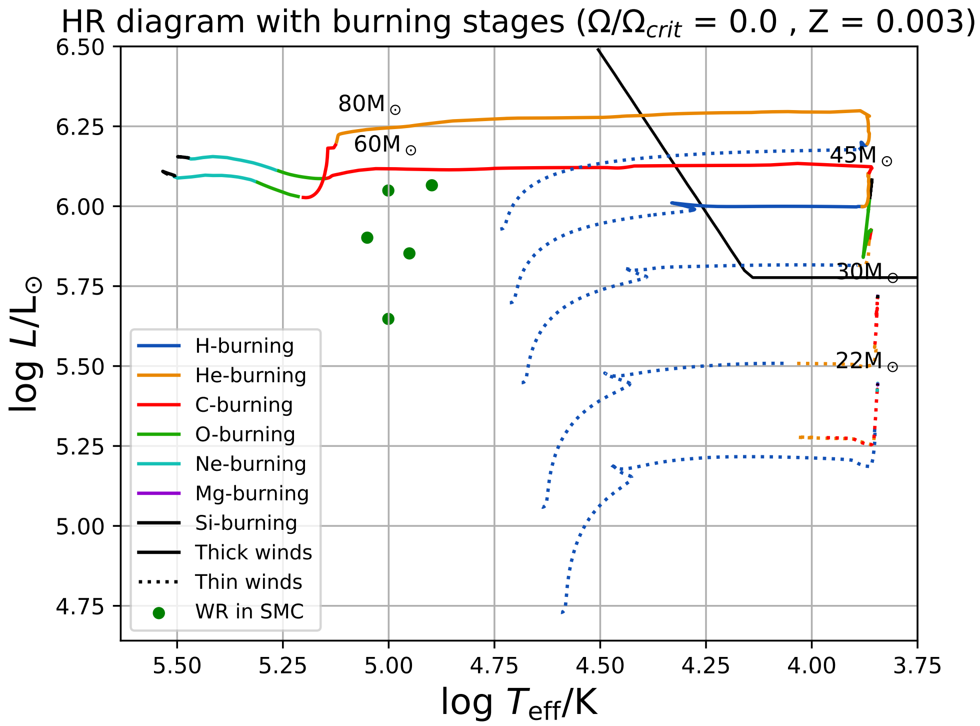

Figure 3.3: Evolution of single stars on the HRD with different burning stages in the SMC, stellar rotation $\Omega/\Omega_{crit} = 0.0$. In the plot, the different burning stages of the star are represented with different colors, while the regime of the stellar wind is indicated with different linestyles, namely dotted for the optically thin and solid for the optically thick. Green circles are the observations of single WRs of [38].

stars ($\gtrsim 60M_\odot$) can enter the thick wind regime and escape the HD limit, dying in the WR part of the HR diagram.

It is also fundamental to note that in the non-rotating case, displayed in Figure 3.3, the stellar tracks are not able to reproduce the WR observation in the SMC in terms of luminosity. Indeed, the stellar tracks for the most massive stars, with initial mass above $60M_\odot$, pass above the experimental points, whereas the less massive stars are not able to strip off their envelope by themselves and to reach a high enough temperature to be considered a WR star.

Considering now Figure 3.4, the models with stars rotating with $\Omega/\Omega_{crit} = 0.6$ are shown. It is possible to see that the agreement between the stellar tracks and the observational point has increased significantly. Indeed, in this case, the high rotational speed changes the evolution of the stars even in the main sequence, making them enter the chemically homogeneous evolution regime. In this conditions the stars become more luminous and compact, making it easier for them to activate optically thick winds, whose presence is shown even at the end of H-burning.

Activating this kind of wind makes the star able to peel off their H-rich envelope, moving them towards the hotter side of the HR diagram and avoid entering the HD limit region. In this case the most massive stars are not the only exception escaping the HD limit, because this behavior extends to much lower masses ($M \simeq 22M_\odot$, making them valuable candidates for stars able to reproduce single WR observations in the SMC.

However, stars with initial velocities $\Omega/\Omega_{\rm crit} \gtrsim 0.6$, corresponding to surface rotational velocities $v_{\rm rot} \gtrsim 450$ km/s, are not representative of the bulk of the O-type stellar population in the SMC.

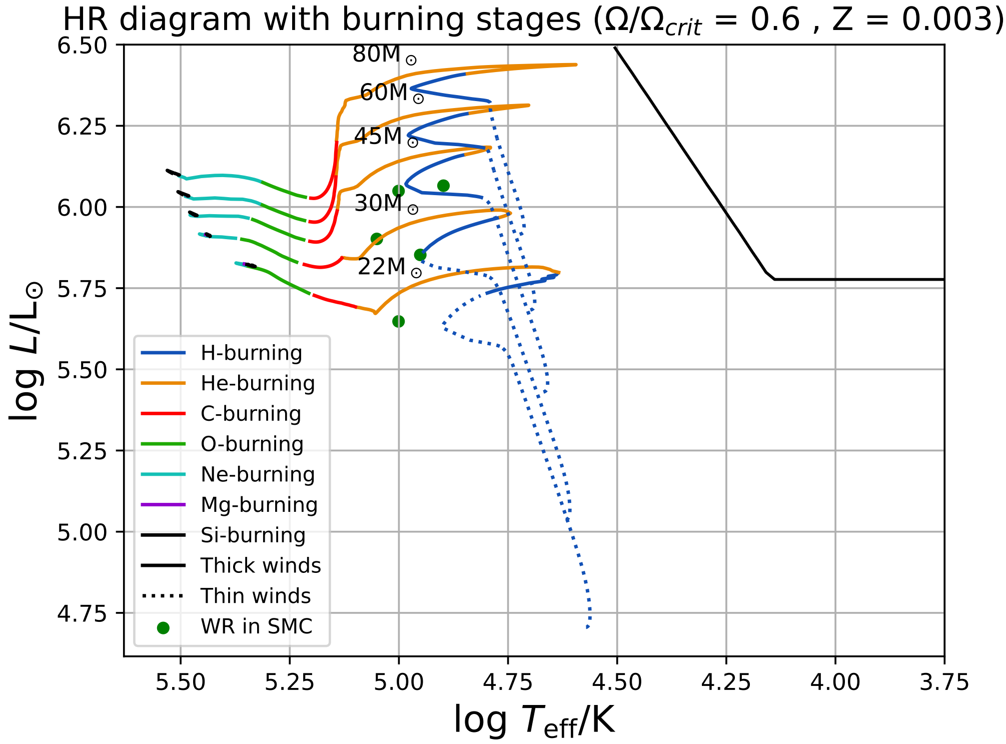

Figure 3.4: Evolution of single stars on the HRD with different burning stages in the SMC, stellar rotation $\Omega/\Omega_{crit} = 0.6$. For the description of the lines, refer to Figure 3.3.

To contextualize this affirmation, [33] built a combined dataset consisting of 171 O-type stars, and the distribution of their observed projected rotational velocities ($v \sin i$) and true rotational velocities (v_{rot}), which result is shown in Figure 3.5. This analysis indicates that stars with $v_{\rm rot} \gtrsim 450$ km/s account for only $\sim$10% of the SMC population. Moreover, most observed O-type stars are no longer on the zero-age main sequence, suggesting they may have already spun down. Consequently, even a small fraction of initially rapidly rotating stars could be sufficient to explain the presence of the seven single Wolf–Rayet (WR) stars observed in the SMC.

LMC results

Looking at Figure 3.6 and 3.7, it appears, coherently with expectations, that in the LMC the threshold for activation of optically thick winds moves to lower masses both in the non rotating ($M \gtrsim 45 M_\odot$) and the rotating case ($M \gtrsim 20 M_\odot$).

This is due mainly to the metallicity of the environment. Indeed, increasing the amount of non-Hydrogen elements and compounds, also increases the amount of metals, whose lines are the driving mechanism of this kind of wind. An increase in the strength of stellar winds then determines a more severe stripping of the star, significantly reducing its mass. Because of this, the Eddington parameter increases (since it is $\propto 1/M$), making it easier to exceed the threshold necessary for the activation of optically thick winds.

Even though the low-luminosity ($\log(L) < 5.5$) part of the WR population of the LMC is not reproduced, this work still presents a significant improvement in providing stellar tracks that move towards the hotter part of the HRD. In any case, there is hope for future testing to reproduce even the missing part of the observed WR dataset, aiming for higher rotational rates or overshooting parameter values.

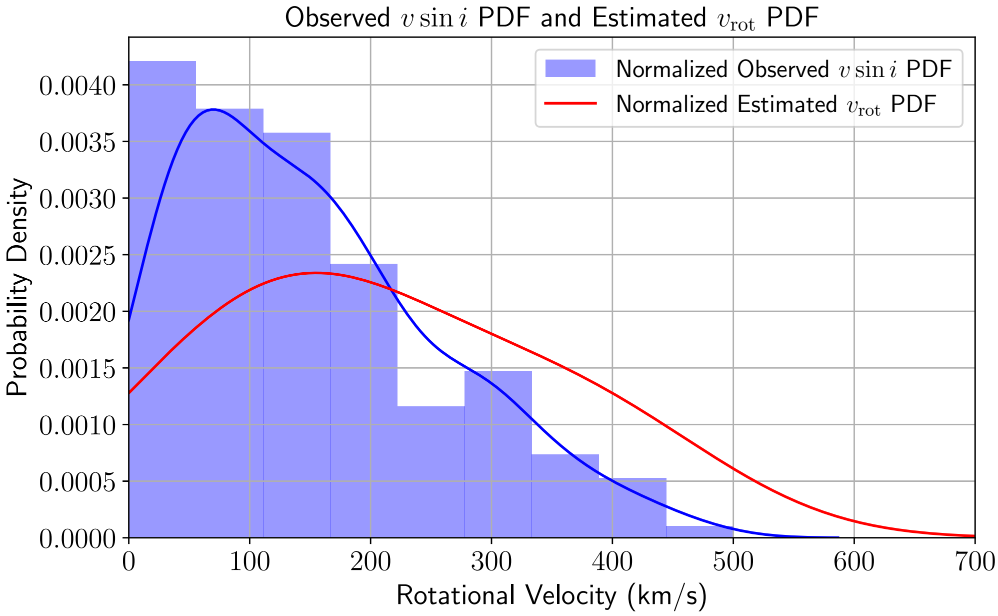

Figure 3.5: Velocity distribution of 171 O-type stars in the SMC. In the plot the normalized observed $v \sin i$ distribution is shown in blue, and the reconstructed initial rotational velocity v_{rot} is in red. The dataset is a compilation from [39], [40], and [41]

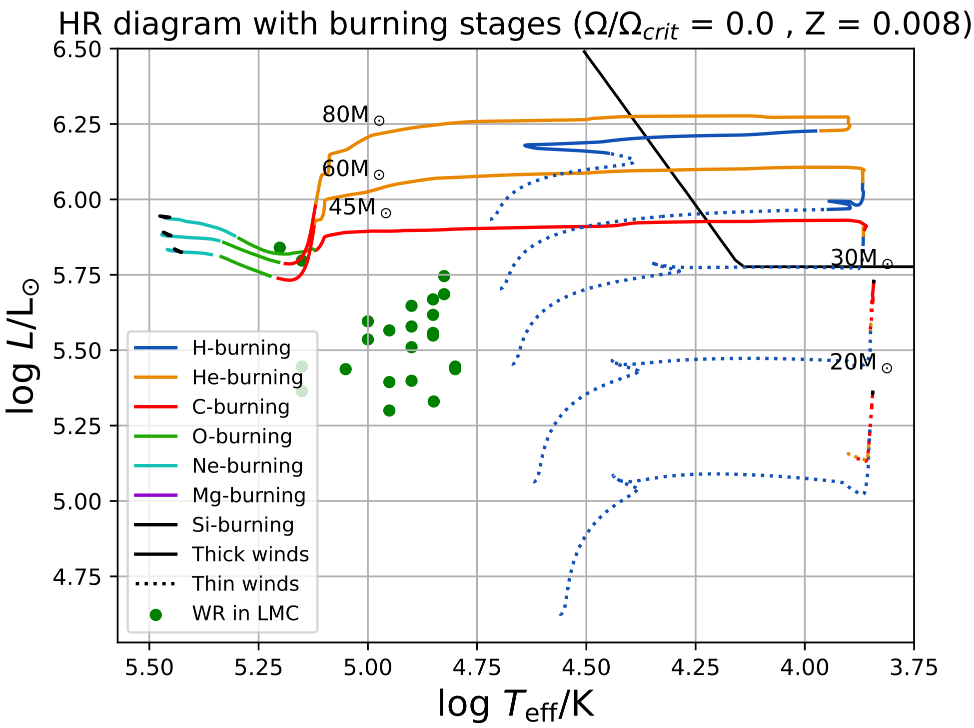

Figure 3.6: Evolution of single stars on the HRD with different burning stages in the LMC, non-rotating case. For the description of the lines, refer to Figure 3.3.

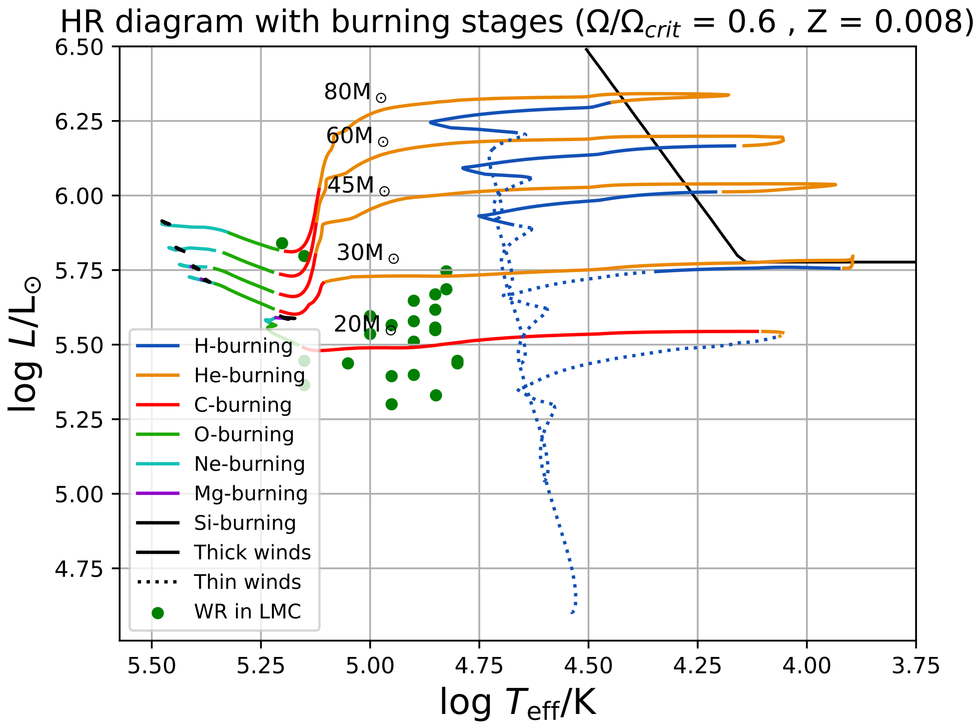

Figure 3.7: Evolution of single stars on the HRD with different burning stages in the LMC, case rotating at $\Omega/\Omega_{crit} = 0.6$. For the description of the lines, refer to Figure 3.3.

3.3.2 Time evolution on the HR diagram

In this section are presented the results for the calculation relative to the amount of time spent by the simulated stars each region of the HRD. In order to calculate this quantity, it is necessary to define the "transition" velocity of the star on the HRD, calculated as follows.

$$v_{\rm HRD} = \sqrt{\left|\frac{d\log L}{dt}\right|^2 + \left|\frac{d\log T}{dt}\right|^2} \tag{3.19}$$

This transition velocity has units of dex yr^{-1}. The inverse of $v_{\rm HRD}$, $\tau_{\rm HRD} \equiv 1/v_{\rm HRD}$, with units of yr dex^{-1}, measures the time it takes for the star to move by 1 dex in the HR diagram, which is shown in Figures 3.8-3.9, through all the star's life on the HRD.

SMC results

Regarding the non-rotating case of the SMC, displayed in the top panel of Figure 3.8, stars with initial masses $\simeq 60\, M_\odot$, activate optically thick winds, and despite their fast evolution, they are able to spend some time at temperatures around $\log(T_{eff}) \sim 5.2$, in the proximity of experimental points. On the other hand, stars with masses lower than this end up being trapped inside of the HD limit and dying there.

On the other hand, the rotating case in the bottom panel of Figure 3.8, shows really promising results, with stars that avoid spending time inside the HD limit, while spending most of their post-main sequence lifetime as WRs, at $\log(T_{eff}) \sim 5.1$.

One note that can be made regarding the reproduction of observational points. When stellar tracks go over the green dots, the speed appears to be relatively high, meaning that the newly formed WR do not spend a high amount of time there, only to slow down immediately after, at slightly higher temperatures, at the transition between the end of core He-burning and C-burning happening. This increased speed over the green dots apparently makes the star more rare to observe and, therefore, less fitting for the comparison with experimental data.

However, this discrepancy can refer to an already known issue in stellar modeling, usually referred to as the *WR radius problem*. As explained in [33], detailed atmosphere models that take into account the effect of the (hot) iron opacity bump on the wind dynamics, could show that the external layers of the star, stripped by strong stellar winds, move outward, effectively cloaking the hydrostatic layers of the star.

In these regimes, the effective temperature referring to the last hydrostatic layers of the star is significantly higher than the observed effective temperature. This is because the wind stays optically thick up to many stellar radii outside the star. In this condition, from the exterior, the star can appear considerably cooler. Because of this, the temperature or radius discrepancy can be attributed at least in a partial way to problems in predicting the effective temperature of stars with optically thick winds.

LMC results
As seen in the previous section, the results of simulations in the LMC show features that are substantially similar to those of the SMC. Focusing on the rotating case, the bottom panel of Figure 3.9, it is possible to see that the data are reproduced very well by stars with a mass $\gtrsim 30M_{\odot}$, while smaller masses (like $M \sim 20M_{\odot}$) tend to spend relatively less time on the observational points, while spending more time on the cooler part of the diagram.

3.3.3 Mass loss strength

In this section we will briefly show the results regarding the strength of the mass loss during the stellar life.

SMC results
In Figure 3.10, the same stellar tracks analyzed in the previous plots are depicted, but in this case the logarithm of the $\dot{M}$ is shown in different colors, depending on its value. As is clearly visible in both panels of Figure 3.10, the strength of the winds increases significantly at the transition point, especially for the tracks relative to higher initial masses, going from darker tones to bright yellow. Comparing the results for rotating stars (bottom panel) with respect to the non-rotating ones (top panel), one can observe that for lower masses like 20 - $40M_{\odot}$ the transition is still visible, despite being less noticeable, with the colored tracks going from deep purple to more blue tones.

Overall, the state-of-the-art knowledge of optically thick winds being stronger than optically thin ones can also be verified for this model.

LMC results
With regard to Figure 3.11, it is clear that the same behavior denoted by the tracks at SMC metallicity (shown in Figure 3.10) is still applicable to the ones at LMC metallicity. Indeed both panels in Figure 3.11 show general evidence of a sharp increase in $\dot{M}$ after the transition point, more visible for high mass stellar tracks, while being less evident but still present for less massive rotating stars.

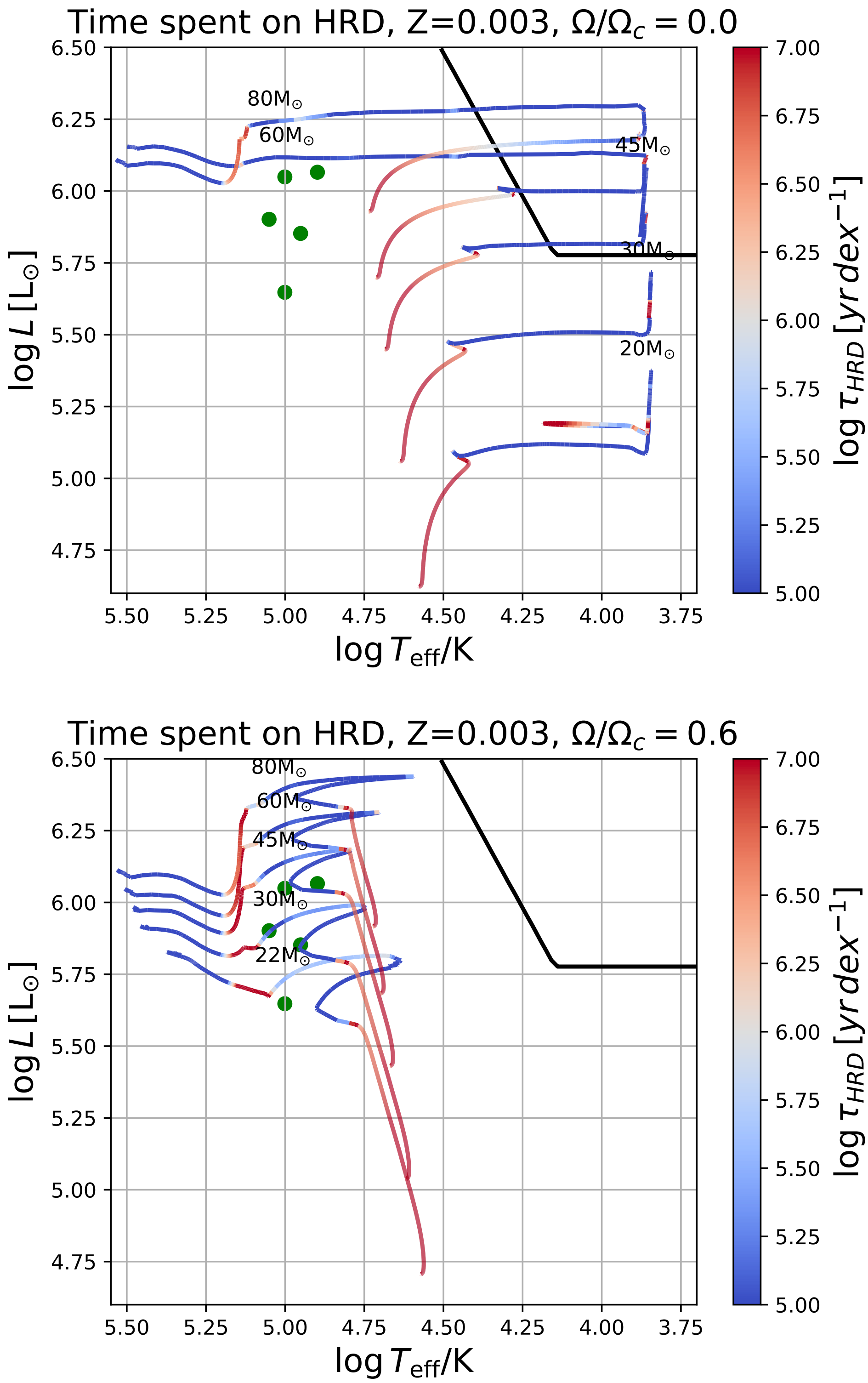

Figure 3.8: Evolution of the time spent on the HRD for stars in the SMC, $\Omega/\Omega_{crit} = 0.0, 0.6$. Warm tones show regions where stars tend to spend more time.

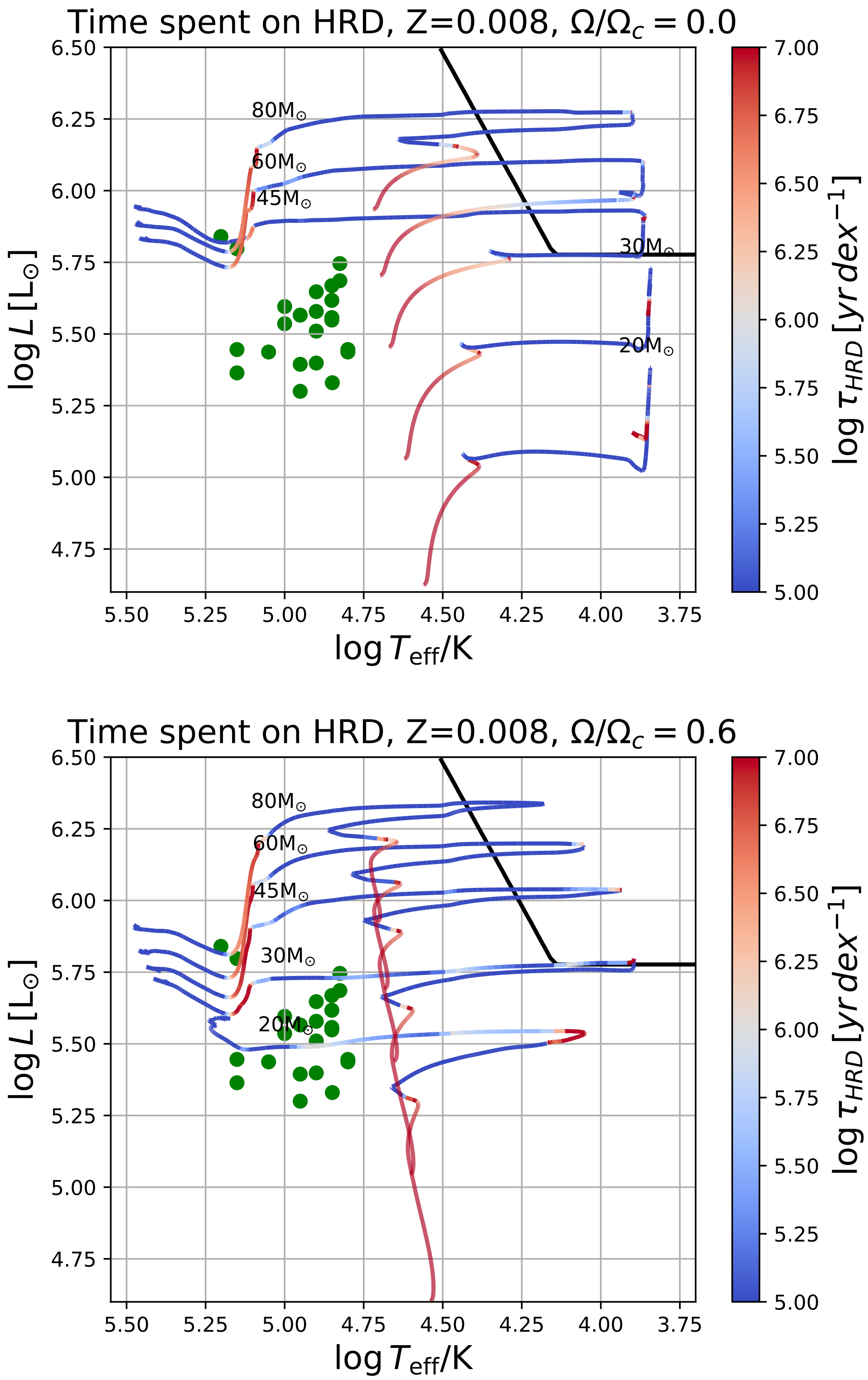

Figure 3.9: Evolution of the time spent on the HRD for stars in the LMC, Ω/Ω_{crit} = 0.0, 0.6. For the description of the colors, refer to Figure 3.8.

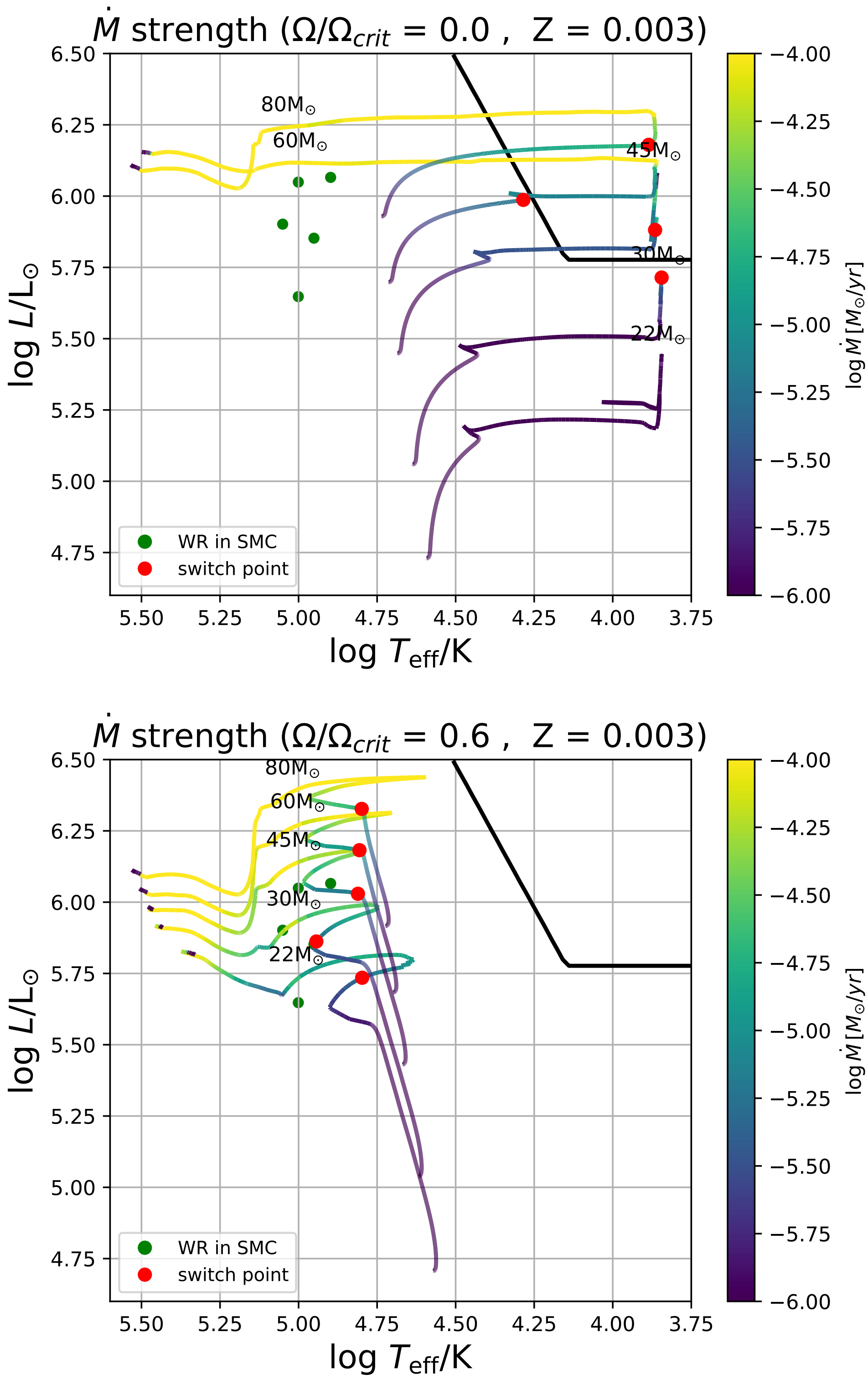

Figure 3.10: Mass loss strength for tracks of non-rotating (top) and rotating (bottom) stars at SMC metallicity. Higher values of mass-loss are represented in yellow tones, while lower values are in purple. On top of this line, a red marker is placed on the transition point, where the wind switches from optically thin to optically thick.

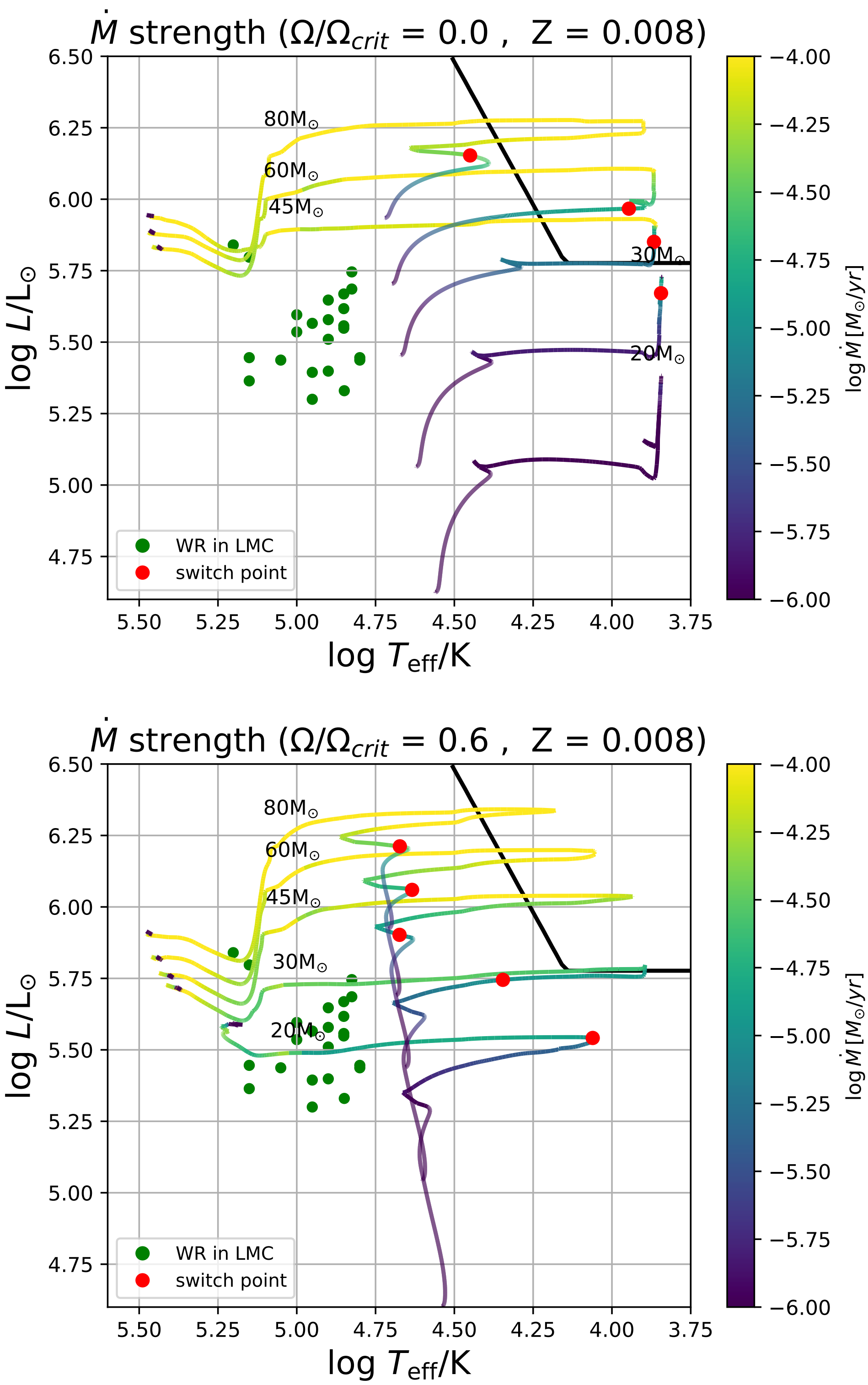

Figure 3.11: Mass loss strength for tracks of non-rotating (top) and rotating (bottom) stars at LMC metallicity. For the description of the lines, refer to Figure 3.10.

3.3.4 Mass and radius evolution

In this section, the evolution of both stellar mass and radius with age will be observed, comparing two different cases, namely the one with non-rotating (NR) and rotating (R) stars.

NR stars will be displayed in black, R stars in red. Since NR stars in the mass range 20-45 do not enter the thick-wind regime, they can be considered as a reference for the behavior of stars evolving solely under thin winds. Instead, NR with M>60 and all R stars are used as a prototype for the evolution of stars that activate optically thick mass-loss prescriptions.

SMC
In the top panel of Figure 3.12 is displayed the evolution of the mass as a function of the age of the star, for the cases mentioned before. The first noticeable feature in Figure 3.12, is that the red tracks appear longer than the black ones. This is an effect due to rotation, since the additional mixing provides more fuel to the core.

Observing the lines in the top panel of Figure 3.12 relative to the masses of 20 and 30 $M_{\odot}$, it is possible to easily compare the different behavior of the mass that would be observed with optically thin and thick winds. Indeed, for smaller masses, the black case is a perfect representation of the optically thin wind case, since during the evolution of the star for these values of initial masses they never activate the enhanced optically thick winds. For this configuration, while the first part of the evolution is similar to the red one, it becomes clear that the mass does not drop that much during the stellar evolution, proving that the stars are not significantly stripped, even in the final stages of their lives.

On the other hand, the red case acts as a representative of the new and enhanced optically thick wind model. Indeed, towards the end of the evolution, when the stars become luminous enough to activate this mass loss recipe, it is possible to see a sudden drop in the stellar mass, meaning that a substantial stripping of the star is acting fairly quickly.

Considering now the higher masses, 45 and 60 $M_{\odot}$, in the top panel of Figure 3.12, the difference is less evident, even if still present, because for these initial masses the stars are able to activate optically thick winds also for the NR case.

In conclusion, by observing the plot in Figure 3.12, it appears that rotating stars are able to be peeled off more than the NR case and, for more massive stars that are still able to activate thick winds, the sudden drop in the value of the mass tends to happen later in the life of the star for rotating stars than for NR ones.

In the bottom panel of Figure 3.12 it is possible to see the evolution of the logarithm of the stellar radius during the life of the star. Comparing the tracks of non-rotating stars with the ones of rotating stars, the influence of a stronger stellar wind and of the high rotational rate appears evident. Indeed, as explained in the previous sections, higher rotational velocities force the stars to become more compact. Adding to this the effect of an enhanced mass loss that strips a significant amount of the external layers, it is possible to obtain a result like the one showcased by the red tracks, where stars tend to stay compact and move towards much smaller radii towards the end of their evolution.

Observing now the black curves, we can see the typical behavior of massive stars with an optically thin wind prescription. Their tracks tend to go to a completely opposite direction with respect to the red one, producing stars that end up cooling and inflating to significantly high stellar radii, without the ability to become single WR stars. This will also have profound consequences for the binary evolution, as we will see in Section 4.4.

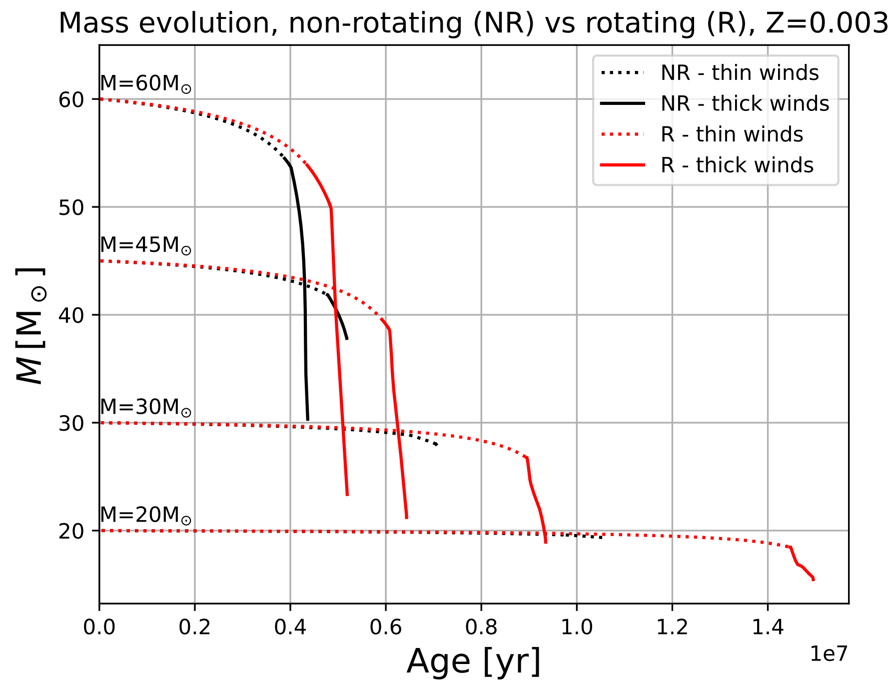

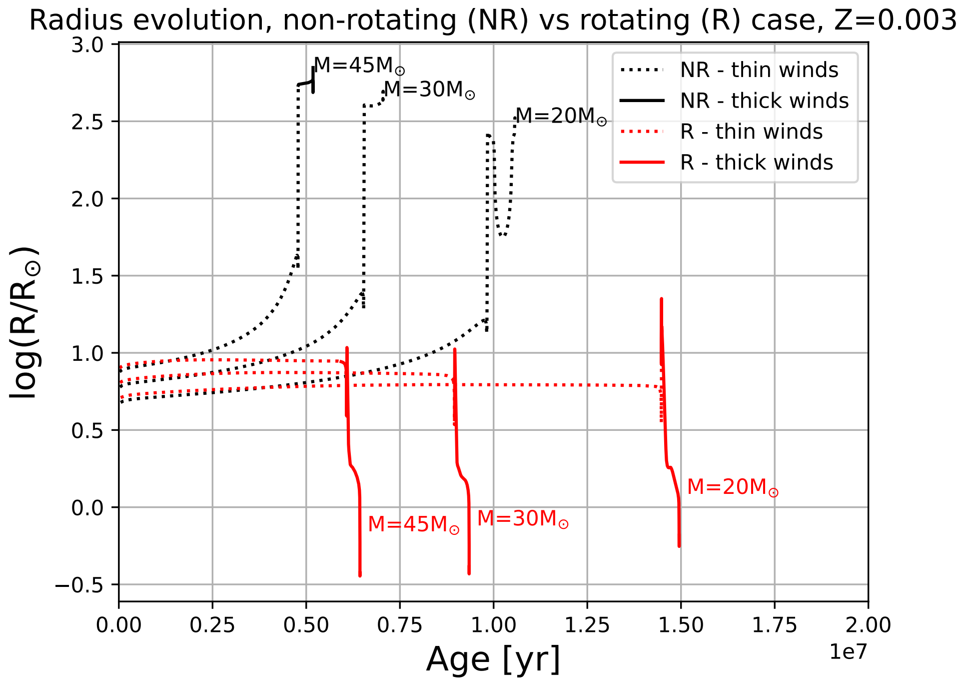

Figure 3.12: Evolution of the stellar mass (top panel) and radius (bottom panel) for rotating (R) and non-rotating (NR) cases, SMC metallicity. The different linestyles are used to describe the different kinds of wind dominating for each phase of the stellar life, respectively optically thin (dotted line), optically thick (solid line).

LMC

The results for the LMC are shown in Figure 3.13. The behavior in this case is similar to the one analyzed for the SMC, with the only difference that the 45 $M_\odot$ tracks now activate thick winds. For the top panel of Figure 3.13, the general behavior of red rotating tracks is a slow decrease of the mass up to the activation of the thick wind recipe, that generates a sudden drop in mass, happening at ages slightly higher than in the black NR case.

Concerning the evolution of the radius in the bottom panel of Figure 3.13, the stars behave similarly to the SMC case, with the only difference represented by the track of the 45 $M_\odot$ star. Indeed, in this case, the non-rotating star is able to activate optically thick winds, and they appear to be strong enough that the star is able to strip and become a WR even in the NR case. However, differently from the SMC, in the LMC case even rotating stars suffer a brief but significant expansion before contracting.

3.3.5 Impact of overshooting

To justify the claim that increased rotational rates and higher overshooting parameters produce similar results on the evolutionary tracks of massive stars, a parameter study has been performed, in order to address an eventual degeneracy produced by the variation of the two parameters.

The results have been published in Boco et al. 2025 [33]. The statement that suggests that varying either the overshooting parameter or the rotational rate of a star produces similar results seems to be verified. Even if in [33] a different stellar wind model is employed, there is a strong belief that the recipe adopted in this work would present a similar behavior under the same testing conditions.

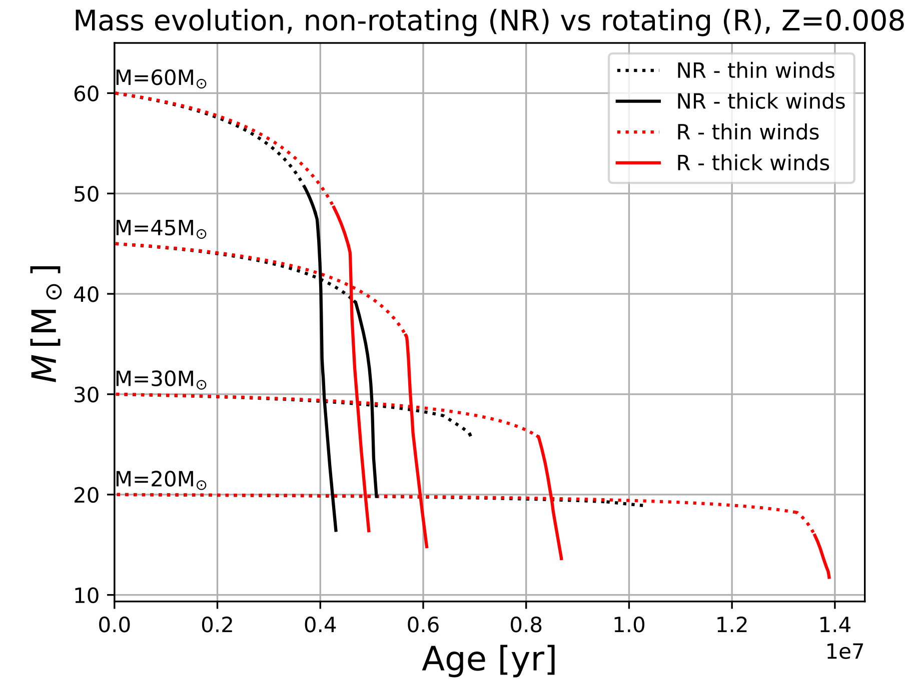

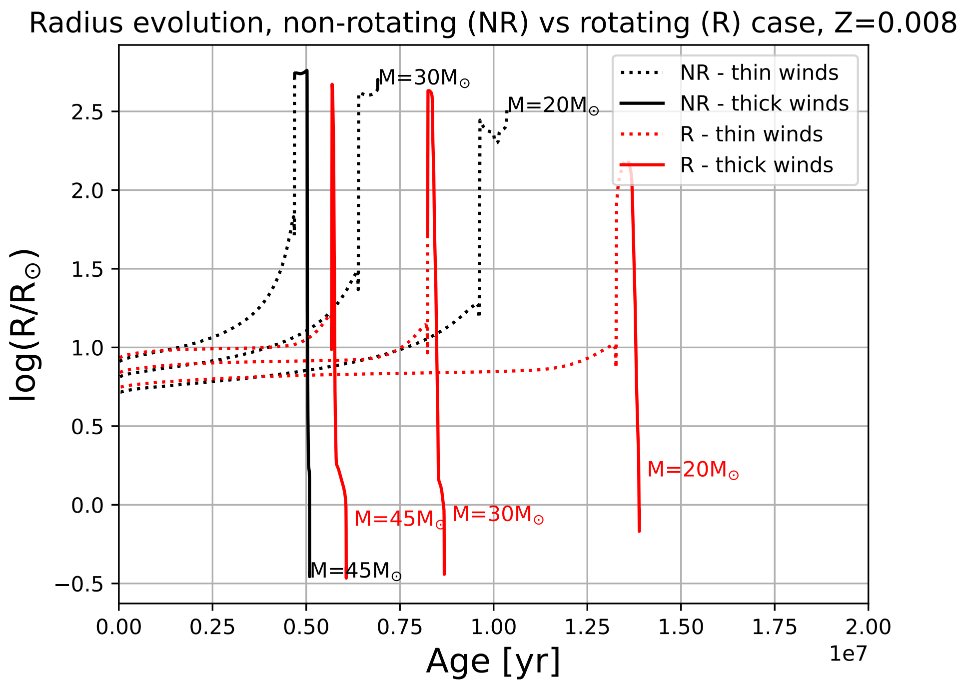

Figure 3.13: Evolution of the stellar mass (top) and radius (bottom) for rotating (R) and non-rotating (NR) cases, LMC metallicity. For the lines' description, refer to Figure 3.12.

Chapter 4

Binaries

4.1 Binary evolution

In order to fully understand massive stars' life and evolution, it is fundamental to study binary and multiple systems, since the vast majority of massive stars (even exceeding 85% for O-stars' population [42]) belongs to systems with such a configuration.

Unlike single stars, the life of a binary system is dramatically influenced by the interaction between the two components, mainly through the transfer of mass from the donor star to the accretor. These interaction events are fundamental. Indeed, even if single stars with the exact same initial properties as the binary components are considered, the evolutionary path taken by donor and accretor will result in being critically different from the one they would have followed if no binary interaction was involved.

It is important to consider that massive stars are often born in systems with orbital separations of the order of the size that these stars reach during their evolution [42], so it is very likely that the majority of these stars (about $\sim 70\%$ of the population) will exchange mass with their companion at some point in their lives [42].

There are many possible and crucial consequences to the interaction processes, making stars follow unique evolutionary paths resulting in specific final fates, very different from the single stellar evolution ones. Indeed, massive binaries that undergo mass transfer and/or stellar collision may form peculiar objects, such as stripped stars, that have had their external envelope removed by their companion, or "puffy" stars, that present inflated envelopes. Moreover, massive binary stars have critical implications for gravitational waves: understanding binary massive stars' evolution is a fundamental step to interpret correctly the observed gravitational wave events, since this kind of system often represents a progenitor for the binary black hole (BBH) that ends up producing the signal observed by the LIGO-Virgo-KAGRA interferometers during its merger.

It is clear that approximating the evolution of massive stars as single stars is not enough to accurately describe how these stars actually behave. However, the modelization of these systems is extremely complex. This is due to the uncertainties in the mathematical description of many physical processes both related to the single star, such as stellar winds or internal mixing mechanisms, and to the binary interactions, like stability and efficiency of the mass-transfer episodes or the common envelope phase.

In order to describe a binary system it is necessary to introduce three fundamental parameters.

The first is the mass ratio $q = M_2/M_1$, where M_2 is the mass of the least massive star in the binary, while M_1 is the most massive star. The second parameter is represented by the orbital period P_{orb}, which can assume a wide variety of values, depending on the characteristics of the system. Finally, the third parameter is the eccentricity e, which quantifies how much the orbit of a system differs from a perfect circle. A circular orbit is indicated by $e = 0$, and higher values mean that the orbit is increasingly more elliptic.

4.1.1 Mass transfer and Roche lobe overflow

As introduced in the previous Section, stars in binary system may undergo multiple episodes of mass transfer, that can happen via stellar winds or through the usually more efficient Roche-lobe overflow (RLOF). The latter mechanism is described, in a reference frame co-rotating with the binary, by the Roche potential:

$$\phi_R = -\frac{G(M_1 + M_2)}{2a}\left[\frac{2}{1+q}\frac{1}{\sqrt{x^2+y^2+z^2}} + \frac{2q}{1+q}\frac{1}{\sqrt{(x-1)^2+y^2+z^2}} + \left(x - \frac{q}{1+q}\right)^2 + y^2\right] \tag{4.1}$$

where q is the mass ratio and a is the semi-major axis of the binary system orbit. The potential can be subdivided into three different terms. The first two are related to the gravitational potentials of the two objects, while the third one is a fictitious centrifugal potential due to the reference frame being non-inertial. As can be seen in the 3D representation displayed in Figure 4.1, this potential has five equilibrium points, called *Lagrangian points*, and the teardrop-shaped equipotential surfaces surrounding each of the stars in the binary are usually referred as *Roche lobes*.

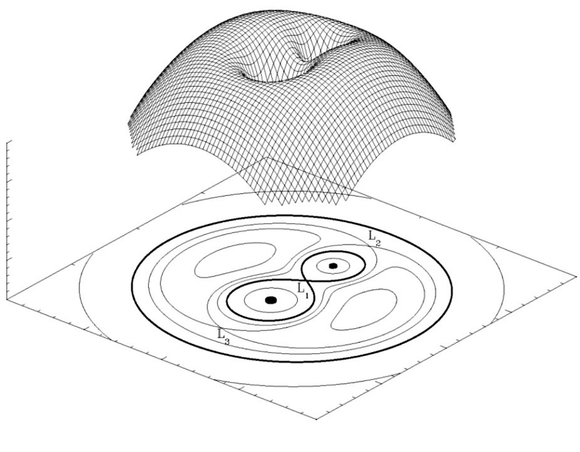

Figure 4.1: 3D representation of the Roche potential [43]

If the donor star inflates enough, it can reach the boundary of its Roche-lobe, filling completely the region where the stellar envelope is still gravitationally bound to the star. At that point, if the star inflates even more, gas and plasma start "spilling" into the Roche lobe of the accretor star through the Lagrangian point L1. The gas then stars to be gravitationally pulled towards the companion star, which accretes it, thus increasing its mass. This kind of process can occur multiple times during the evolution of the binary system, and can dramatically influence the structure of the binary object and both evolution and final fate of the single components. For a circular orbit, the Roche lobe radius is well approximated by the relation found in Eggleton et al. 1983 [44]:

$$R_L = \frac{0.49 \cdot q^{2/3}}{(0.6 \cdot q^{2/3} + \ln(1 + q^{1/3}))} \cdot a \tag{4.2}$$

indicating that the radius of the Roche lobe depends only on the orbital separation a and on the mass ratio q.

4.1.2 Common envelope

The common envelope (CE) phase is a crucial process in binary massive star evolution, which occurs when mass transfer between the two components of the system becomes dynamically unstable. This instability starts happening when the donor star is no longer able to maintain its hydrostatic equilibrium, and expands over the size of its Roche lobe, engulfing the companion in its external envelope. The effects of this kind of process are varied and can significantly influence the outcome of the evolutionary path of the binary.

The mechanism works as follows. When one or both stars undergo a CE phase, the envelope (which can belong to only one star or is resulting from the fusion of the two inflated envelopes) loses co-rotation with the stellar cores, and a drag force starts forming due to the different rotational velocities. Through this friction, energy and momentum are transferred from the binary system to the gaseous envelope. This increases the envelope's temperature, making it more loosely bound to the system. As a consequence of the energy removal from the binary system, the cores (or core and stellar companion) start spiraling in, therefore effectively reducing the orbital separation between the two components. In the case where the envelope gains sufficient energy to be ejected, the binary system is able to survive the CE phase, becoming a "stripped binary", a system usually made of two naked stellar cores (WR) or a compact object and a WR star. Otherwise, the stars are highly likely to end up merging inside the envelope, forming a single object. The product of this evolutionary path has been hypothesized to be the origin of very peculiar objects, such as Thorne-Zytkow objects, black holes with mass in the pair instability gap or massive stars with very high magnetic fields.

In the cartoon showed in Figure 4.2, it is possible to see the summary of the different evolutionary paths that can be taken by a binary star that undergoes a common envelope episode.

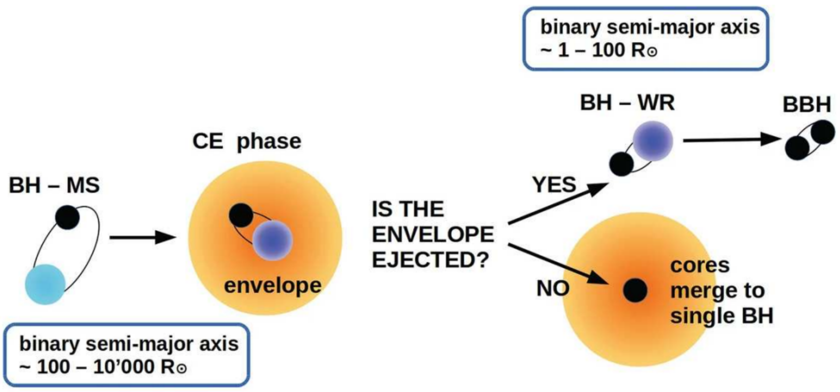

Figure 4.2: Diagram representing a common envelope episode in a binary starting from a BH - Main sequence (MS) star configuration [45]

The chance of a CE phase happening depends strongly on the stability of the mass transfer episodes, and on the nature of the external envelope of the stars considered. Indeed, stars with radiative envelopes usually favor a stable mass transfer (except for binaries with extreme mass ratios), whereas stars with deep convective envelopes are more keen on presenting dynamical instabilities, thus forming common envelopes more often.

Anyway, modeling the CE phase of a binary system is still nowadays an intrinsically complex problem, that challenges all stellar evolution codes. The main reason for these difficulties lies in the need of taking into account a high number of physical effects happening on different spatial and temporal scales. Examples of sources of uncertainty are represented by the binding energy of the envelope, the energy transfer efficiency between the system and the gaseous envelope, and the location of the actual boundary between core and envelope.

The description of the CE adopted in this work is also known as α *formalism*. This is used to describe the energy needed to unbind the envelope, assuming that the energy only comes from the one lost by the cores during the spiral-in phase, and it is expressed as follows:

$$\Delta E = \alpha(E_{b,f} - E_{b,i}) = \alpha \frac{G M_{c_1} M_{c_2}}{2} \left(\frac{1}{a_f} - \frac{1}{a_i} \right) \tag{4.3}$$

where E_b is the binding energy of the system, respectively, at the beginning and at the end of the CE phase, M_{c_i} , $i = 1, 2$ is the mass of the core i, a is the length of the semi-major axis before and after the phase, and α is a dimensionless parameter describing the fraction of the binding energy actually transferred to the envelope.

4.1.3 Merger efficiency

One of the fundamental quantities calculated in this work is the *merger efficiency*, indicated with η, which represents the number of merging BBHs (or other binary compact objects (BCOs)) per unit of total initial stellar mass [24]. This quantity is of crucial importance in the context of BBHs, because it enables a deeper understanding of the merger rate densities observed by the LIGO-Virgo-KAGRA (LVK) collaboration, and allows to make predictions regarding gravitational wave signals.

The calculation of the merger efficiency value is based on binary population synthesis simulations, and is typically defined as the ratio between the number of BCOs merging within a Hubble time N_{BCO} and the total initial mass of the simulated stellar population $M_{population}$. However, this calculation has to be corrected to take into account two main factors: the incomplete sampling of the initial mass function (IMF), and the actual fraction of binaries in a realistic stellar population.

The former correction, accounted for in the factor f_{IMF}, is mainly due to the initial masses of the binary components being assumed to belong to an IMF, whose behavior is described by a power-law with a negative power. This means that the number of low mass bodies that enter the population, not relevant to the study of BBHs, are dramatically higher than the one of the actually useful stars, wasting a considerable amount of computational time. For this reason, bodies with a primary mass lower than $8M_\odot$ are excluded from the simulated population and need to be accounted for in the later calculation of η.

For the latter factor, f_{bin}, the reason lies in the kind of simulated population. Indeed, to maximize the number of relevant systems for the analysis (so massive binary stars) it is useful to feed the population synthesis code an initial group of only binary stars. However, this configuration is not realistic, since there is no such fraction of binary stars in clusters of the known universe. Therefore, to better align the results with observationally based real-world values, one must assume that the actual stellar population is larger than the simulated binary sample, and that binaries represent only a fraction of all stars, typically taken to be 1/2. Finally, accounting for all the correction factors, the equation to calculate the merger efficiency becomes

$$\eta = f_{bin}\ f_{IMF}\ \frac{\mathcal{N}_{tot}(t_{merge} \lesssim 13.8\,\mathrm{Gyr})}{M_*(Z)} \tag{4.4}$$

This quantity is significantly influenced by a wide variety of factors, summarized below.

- **Metallicity**: the merger efficiency can increase by 1 to 4 orders of magnitude for metal-poor progenitors compared to metal-rich ones, as can be seen in Figure 4.3, where the merger efficiency was calculated for different metallicities.

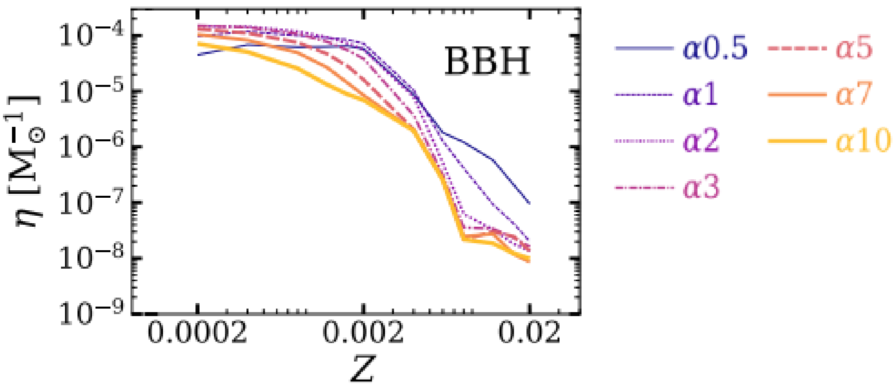

Figure 4.3: Evolution of the merger efficiency of BBHs as a function of metallicity [5]. Differently colored lines refer to models with different assumed values of the common envelope parameter α_{CE}.

- **CE efficiency parameter**: Even if it has a lighter impact compared to metallicity, α_{CE} is still capable of affecting the merger efficiency by influencing the formation channels of the systems and their survival rate to the CE phase. Higher values of α_{CE} tend to move the efficiency peak towards lower metallicities, as shown in Figure 4.3. The value adopted for this work is $\alpha_{CE} = 3$, as in [5] it is suggested that values of $\alpha_{CE} \gtrsim 1$ produce more consistent results with those found by the LVK collaboration.

- **Natal kicks**: In order to form BCOs, it is necessary for the binary to undergo up to 2 supernova (SN) explosions, that leave behind compact objects like BH and NS. During these explosive episodes, it is possible that matter is ejected in an asymmetric way. These asymmetries can push the newborn compact object, with a speed that can go from $\sim 10\,km\,s^{-1}$ to $\sim 1000\,km\,s^{-1}$, depending on the structural configuration of the progenitor. These pushes are called *natal kicks* and can have a significant impact on the formation and evolution of a BCO. Moreover, these kicks can impact the number of merging BCOs, since the majority of loosely bound binaries could be disrupted.

- **Stellar Evolution Models**: Uncertainties in stellar evolution models, such as prescriptions for stellar wind mass loss or the stability of mass transfer, affect the properties of progenitors and, consequently, the merger efficiency and merger times of BBH.

4.2 Effect of strong winds

High stellar winds have substantial consequences on binary systems, because they influence both the evolutionary path of single stars (as seen in Section 3.3), and also the interactions between the two stars.

With regard to the effects on single stars, strong stellar winds can deeply influence fundamental parameters such as luminosity, compactness, mass, radius, and temperature. In particular, the pre-supernova masses will be reduced, because the stellar envelope is stripped away by the wind (as seen in Section 3.3.4). In addition to this, the core masses will be smaller, as shown in [33] and [34]. Finally, also the pre-supernova radii will be smaller, as shown in Section 3.3.4. In general, smaller pre-SN and core masses may result in stronger natal kicks, that might disrupt the binary system. On the other hand, the smaller core masses may result in a severe reduction of pulsational pair instability supernovae (PPISNe) and pair instability supernovae (PISNe) [34], yielding an increase in the number of massive BHs.

In the non-rotating stellar models, computed with the mass loss prescription of [22], where thick winds are activated only for $M_{ZAMS} > 60\,M_{\odot}$, the increased BH production due to the avoidance of the pair instability regime is the dominant effect. For this reason, the total number of bound BBH surviving at the end of binary evolution is slightly larger with respect to the thin-winds case. Concerning the reduction of stellar radii, this will substantially decrease the number of stellar mergers during binary evolution. However, this effect is mostly visible in the case with stars rotating at $\Omega/\Omega_{crit} = 0.6$. Only when stellar rotation is involved the star is kept compact, so the number of stellar mergers is reduced even in stars born very close to each other. This effect will be seen more clearly in Section 4.4.2.

As introduced before, strong stellar winds can also influence binary evolution. The most visible consequence is the widening of the binary orbit. Strong stellar winds strip a considerable amount of material off of the surface of the stars which is, at least partially, lost in the interstellar medium. To preserve the angular momentum conservation, the system increases its orbital semi-major axis, thus making the binary wider. Strong winds also influence the size and binding energy of common envelopes. Indeed, for high metallicity the winds are able to strip away the envelopes, making them relatively small. This can have consequences on the binary evolution, because if the CE episodes are characterized by envelopes with reduced dimensions, it is possible that the system does not get tightened enough to merge via gravitational waves emission. Moreover, since high stellar winds can make the stars more compact and with a smaller radius, they expand less and are less likely to fill their Roche lobe, thus avoiding mass-transfer episodes.

All these processes can significantly influence the final fate of a binary, and not all of them act in the same direction. Indeed, stronger kicks tend to unbind binary systems, and the binary interaction effects make the orbits wider. These mechanisms imply a reduction in the number of bound BBHs merging within a Hubble time. However, all these effects can be countered by the reduction of the number of stars undergoing PPISNe and PISN, thus producing more BHs generated by very massive stars, Moreover, there will be less stellar mergers of binaries born with a small orbital separation, consequently generating a higher amount of BBHs with very tight orbits. These two effects tend to increase the number of BBHs merging within a Hubble time.

In the next sections will be studied how the effects introduced above will combine, comparing cases with different wind prescriptions and rotational speeds: the case analyzed in Iorio et al. 2023 [24] (non-rotating stars, mostly with optically thin winds), and the cases with the Bestenlehner 2020 [22] wind prescription, both for non-rotating and rotating stars.

4.3 Population synthesis

Stellar evolution codes, like MESA, can produce detailed single and binary star models with an incredible precision, but they are often computationally expensive In fact, they can take up to days to reach completion for a binary model, depending on its complexity.

To address the need for a code to simulate numerous stars and binary systems at once, so that to studies on the characteristics of an extended group of objects can be performed, population synthesis codes come in handy. Indeed they are designed to rapidly model samples of even billions of stars in just a matter of hours. Their speed is a feature of crucial importance, especially when a study spanning a large parameter space over a large group of stars has to be performed.

In recent years, a wide variety of population synthesis codes has been developed independently. In general some of them can be described as *rapid binary evolution codes*, which rely on fitting formulas developed by Hurley et al. 2000 [46], based upon the tracks by Pols et al. [47]. These tracks express the main stellar properties as functions of age, mass, and metallicity. This precomputed set of tracks is usually combined with prescriptions and parametrized models to describe complex binary evolution physics. The main codes using this approach are, for example, MOBSE [48] and COSMIC [49]. However, despite being extremely fast, these models are limited by the physical assumptions made to describe the models, and they present a tendency to overestimate the occurrence of CE phases [50].

An alternative to the previous kind of tools is presented by codes that adopt a different strategy. Instead of analytical formulas, they calculate stellar evolution including an algorithm which interpolates the main properties of stellar evolution (mass, radius, luminosity etc.) as a function of time and metallicity, based on pre-computed tables, usually generated by detailed stellar evolution codes like MESA or PARSEC. Despite being relatively slower with respect to rapid codes, these are more flexible and detailed than the simplified treatment with fitting formulas. Examples of this kind of codes are given by POSYDON [51] or SEVN [24], the code used in this work, used in combination with catalogs of stellar tracks computed in MESA.

4.3.1 SEVN code

SEVN (Stellar EVolution for N-body) [24] is a binary population synthesis code, used to explore the wide parameter space concerning binary compact objects' formation and massive star evolution. It is an incredibly versatile and flexible tool for astrophysics research, particularly for the study of gravitational wave progenitors.

This code is able to calculate the evolution of stars via interpolation of precomputed sets of stellar tracks, organized in SEVN-tables, while the interactions during binary evolution are implemented through analytic and semi-analytic prescriptions. This methodology allows the user to easily change and update the stellar evolutionary models by uploading new sets of tables without changing the internal structure of the code.

In order to adapt the output of detailed stellar evolution codes to the format required by SEVN, TrackCruncher has been developed. This is a complementary tool that elaborates stellar tracks into tables optimized for SEVN, and can be easily be customized for the different formats of the detail codes' outputs. Moreover, this tool has a built-in function that evaluates the produced tables, checking whether they are compatible with the SEVN requirements.

The different processes regarding binary and stellar properties are represented by a collection of C++ classes, organized as shown in Figure 4.4.

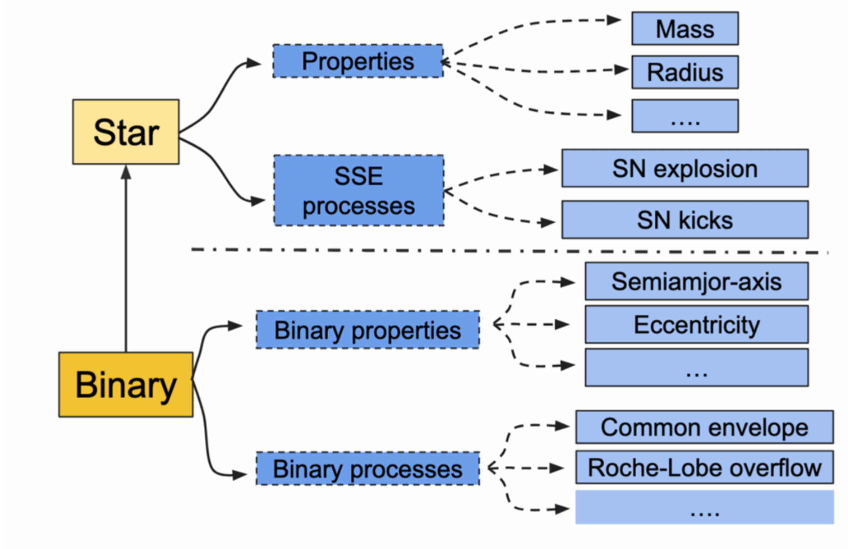

Figure 4.4: Overview of structure and organization of SEVN code [24]

As hinted before, SEVN is able to treat both the single stellar evolution (SSE) and the binary stellar evolution (BSE). In order to define uniquely the SSE, only the star's metallicity Z and the zero-age main-sequence mass (M_{ZAMS}) are required. In fact, if the same M_{ZAMS} and Z are provided for two different simulations, the results will always be the same, given that the set of evolutionary tables used for the simulations of the two stars will be the same.

To model both the binary and single stellar evolution, two sets of tables are employed, one for stars that start to evolve on the Hydrogen main sequence and one for pure-Helium stars. Each set of tables is constituted of 7 elements, related to different stellar properties: age, mass, radius, bolometric luminosity, mass of the He-core, mass of the CO-core and stellar phase.

The stellar phase is represented by a number between 0 and 7, summarized below:

- 0: Pre-Main Sequence
- 1: Main Sequence (start of Hydrogen burning)
- 2: Terminal Main Sequence (creation of a Helium core)
- 3: Shell Hydrogen burning
- 4: Core Helium burning
- 5: Terminal Core He-burning (creation of a CO core)
- 6: Shell He-burning
- 7: Remnant

In order to classify the remnant of a star after a SN explosion, another number is used, called `RemType`, which can assume the following values:

- -1: Massless remnant
- 0: Star is not a remnant
- 1: Helium White Dwarf (WD)

- 2: Carbon-Oxygen WD
- 3: Oxygen-Neon WD
- 4: Neutron star (NS) after electron-capture supernova
- 5: NS after core-collapse supernova
- 6: Black hole

During the evolution of a star, especially when it is in a binary, SEVN follows the stellar track that is closest to the initial mass given at the beginning of the simulation. The general rule is that, unless there is a change in the core mass, a jump to a new track is not allowed.

In the case a jump is necessary, the code looks through the tracks in the tables for the one with the best match for the stellar mass at the same evolutionary stage. The need to change tracks can be due to many different causes:

- **Star accreting/losing mass in the MS**: if the mass loss or accretion happens to exceed a certain threshold, the code will always jump to a new mass
- **Outside of MS**: the code will jump to a new track only if forced by some processes, such as mergers
- **Envelope stripping**: the star will always jump to a new pure-Helium track.

A schematic summary of the algorithm used to decide whether it is necessary to change track is shown in Figure 4.5.

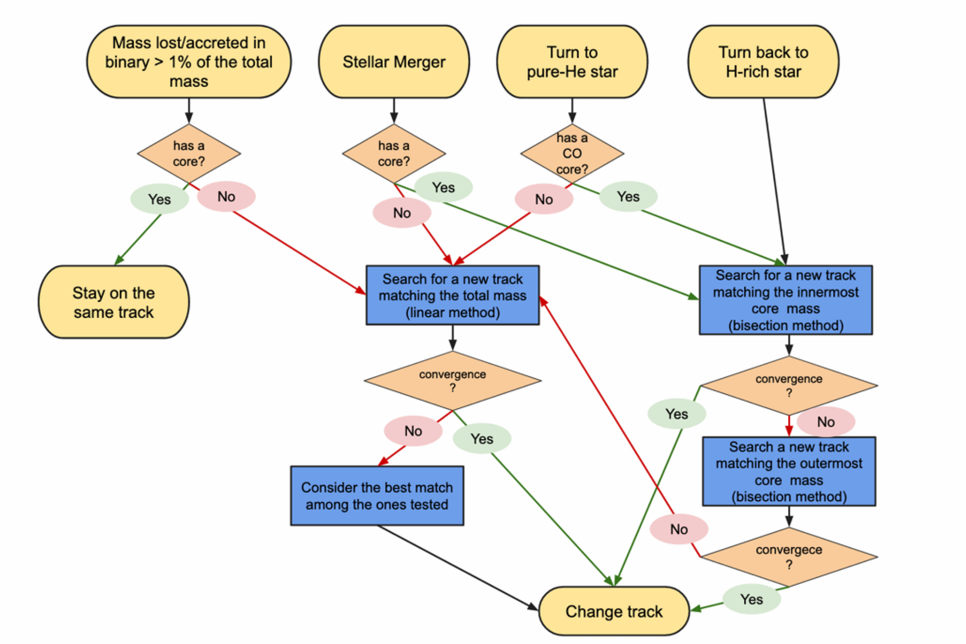

Figure 4.5: Representation of the algorithm used by SEVN during a stellar track change [24]

4.3.2 Simulation setup

In order to make the starting binary population as similar as possible to the one used in [24], the two sets of 10^6 systems, one for each metallicity ($Z = 0.003, 0.008$), used as input for the simulation were configured by extracting the binary parameters from distributions similar to the ones used in [24], and are summarized below.

- **Primary mass** M_1: the primary masses were randomly chosen in the interval $8 \lesssim M/M_\odot \lesssim 200$, drawn from a Kroupa initial mass function, described in [52]

$$\mathcal{F}(M_1) \propto M_1^{-2.3} \tag{4.5}$$

- **Secondary mass** M_2: to extract a list of secondary masses, firstly some mass ratios q are extracted from a distribution taken from Sana et al. 2012 [53]

$$\mathcal{F}(q) \propto q^{-0.1},\ q \in [0.1, 1] \tag{4.6}$$

  then, a list of secondary masses is recovered using $M_2 = q \cdot M_1$

- **Orbital period**: the orbital periods have been generated according to the distribution by Sana et al. 2012 [53], having

$$\mathcal{F}(P) \propto (\log P)^{-0.55},\ \log P \in [0.15, 5.5] \tag{4.7}$$

- **Eccentricity**: like the orbital periods, also eccentricities are drawn from the distribution by Sana et al. 2012 [53], with

$$\mathcal{F}(e) \propto e^{-0.42},\ e \in [0, 0.9] \tag{4.8}$$

The total effective mass of the population is, for both metallicites, around $2.8 \cdot 10^8\, M_\odot$, with a correction factor for the incomplete IMF sampling due to mass cuts equal to $f_{IMF} = 0.235$. As stated above, the metallicity values chosen for the two simulations are $Z = 0.003, 0.008$, and the common envelope efficiency parameter α_{CE} is set equal to 3.

In this work, SEVN is used to evolve all the binaries up to the moment when both stars are compact remnants or until the merger product becomes a compact remnant in the case of a collision. Just like in [24], for BCOs the only active process is the orbital decay by gravitational wave (GW) emission, and the merger time is estimated a posteriori, using a high-precision analytic approximation of the integration of the equations from Peters 1964 [54]. These relations describe the orbital decay and circularization due to GW emission. The results of these calculations are shown in the code output in the parameter *GWtime*, extensively used in the analysis.

4.4 SEVN results

In this section are presented the results of SEVN simulations performed with the initial conditions described in the previous sections.

In order to generate a set of customized tables to be used as input for the SEVN simulations, the stellar tracks produced and analyzed in the previous chapter have been processed through the code TrackCruncher. This code extracts the main stellar properties from the output of stellar evolution codes (MESA in this work) and stores them in the SEVN table format, estimating also the starting time of the SEVN phases.

However, since the stellar tracks computed with MESA for this work start from an initial mass of $10M_{\odot}$, in order to compute binary tracks for stars with masses lower than this, the produced tables have been integrated with the values for initial masses $0.6 - 9\,M_{\odot}$ taken from MIST tables[1], also computed from MESA stellar tracks, and available at the following link: `https://gitlab.com/sevncodes/sevn/-/tree/SEVN/tables`.

Like in the previous case, the main results shown will be those regarding the SMC metallicity, but those at LMC metallicity will also be included. Furthermore, through the analysis of the SEVN runs performed, a comparison will be made with the results of the SEVN runs performed in Iorio et al. 2023 [24], which we take as a reference for optically thin winds. In this way, it will be possible to see the impact of the wind prescription on a population syntheses study.

However, an important disclaimer should be made regarding the possibility of comparing the results of the runs performed for this work and those of Iorio et al. 2023 [24]. Since the simulated stellar populations are different[2], only the results normalized over the mass of the total population can be straightforwardly compared. For all the non-normalized results, we will compare only the shape of the distributions rather than the numbers.

A more thorough and self-consistent analysis will be performed in the future by computing more stellar tracks with optically thin wind prescriptions, and employing the same simulated stellar population as an input. On the other hand, the $\Omega/\Omega_{crit} = 0$ and $\Omega/\Omega_{crit} = 0.6$ cases can be compared both in shape and absolute numbers, since the simulated initial population is the same.

4.4.1 Numerical results

In this section will be described the first results of the simulations performed on a population of 10^6 binaries, for two different metallicities and two rotation rates per each metallicity.

SMC

In the Small Magellanic Cloud, out of the whole population, about 5% of binaries evolved from stellar tracks of non-rotating stars becomes a bound BBH. For rotating stars, we see an increase in this quantity, with an 18% of the binaries becoming a bound BBH.

If we refer the number of bound BBHs to the mass of the population, correcting for the mass cut and the binary fraction as explained in Section 4.1.3, we obtain the following results: in the non-rotating case $1.9 \cdot 10^{-4}$, in the rotating one $6.4 \cdot 10^{-4}$. In the case studied by Iorio et al. 2023 [24], taken as a reference for thin winds, this number is equal to $1.7 \cdot 10^{-4}$.

[1] The additional data for the tables in this work has been taken from `SEVNtracks_MIST_AGBrobust`.

[2] Iorio et al. 2023 simulates 10^6 binaries with $M_1 > 5\,\mathrm{M}_{\odot}$, while in this study I simulate 10^6 binaries with $M_1 > 8\,\mathrm{M}_{\odot}$.

The discrepancy between the NR case and the one in [24] is minimal. Indeed, stars with a mass $\lesssim 60\,M_\odot$, so the majority of simulated stars, have only optically thin winds. Stars with mass $\gtrsim 60\,M_\odot$ instead have different winds in the NR case. For these objects, optically thick winds are active, and prevent pulsation pair instability SN (PPISN) or pair instability SN (PISN), thus increasing the number of BHs. These BHs also suffer weaker natal kicks. For this reason, with respect to the [24] case, in this work we have a slightly higher fraction of bound BBHs.

On the other hand, in the R case there are significantly more bound BBHs, with respect to both the NR case and the [24] case. This is because of two main reasons: first, rotation generates bigger cores, thus producing more BHs overall. Secondly, since stars stay more compact in the R case, the number of stellar mergers in systems born with a small orbital separation is significantly reduced (as seen in Section 4.2).

Considering now only the bound BBHs, only a very small percentage of them are actually able to merge within the age of the universe (1 Hubble time). Indeed, in the non-rotating case 5.2% of the bound BBH end up coalescing, while in the rotating case, where winds are enhanced by rotation, there is a merger only in 2.5% of the cases. These numbers appear even lower if compared with the percentage of merging BBH with respect to the population of bound BBH in [24]: about 21% of bound systems ends up coalescing. This significant discrepancy is mainly due to the effect of strong winds that tend to widen the binary orbits and reduce mass-transfers and CE efficiency (see Section 4.2).

The merger efficiency has then been calculated for all the three cases according to equation 4.4, obtaining $1.03 \cdot 10^{-5}\,M_\odot^{-1}$ for the non-rotating case, $1.65 \cdot 10^{-5}\,M_\odot^{-1}$ for the rotating case, to be compared with the result of Iorio et al. at a similar metallicity, namely $3.72 \cdot 10^{-5}\,M_\odot^{-1}$. It is clearly visible that the new wind recipe yields significantly lower merger efficiency values for both the rotating and the non-rotating ones, with respect to the one obtained in the case for optically thin winds.

The rotating case has a higher merger efficiency than the non-rotating one, because of the much higher efficiency in producing bound BBHs (a factor $\gtrsim 3$ larger), due to less stellar mergers. This compensates and oversteps the effect of orbital widening, which reduces BBH mergers by just a factor ~ 2.

LMC

Considering now the Large Magellanic Cloud, for non-rotating stars the results are similar to the SMC non-rotating case, with about 5.4% of the systems becoming bound BBH with respect to the total number of simulated binaries. Regarding the rotating case, it is possible see an increase in the number of bound BBH, which becomes $\simeq 10\%$. Referring now to the mass of the population, as in the previous case, we obtain: $1.9 \cdot 10^{-4}$ for the non-rotating case, $3.6 \cdot 10^{-4}$ in the rotating case, and $1.4 \cdot 10^{-4}$ for [24].

In the non-rotating case, the effect of strong stellar winds on the number of merging BBH is clear: indeed, only 0.8% of systems merge in one Hubble time. This is coherent with the hypothesis of the influence of a high mass-loss enhanced by a higher metallicity with respect to the SMC case. This result is almost the same as that obtained in [24], with 0.78% merging BBHs. In the rotating case, instead, we see an increased amount of merging systems (3%) with respect to the non-rotating one. This may be due simply to the higher percentage of bound BBH forming, an effect of the fast rotational speed.

Regarding the merger efficiency, the calculated values are: $1.49 \cdot 10^{-6}\, M_{\odot}^{-1}$ for the non-rotating case, $1.05 \cdot 10^{-5}\, M_{\odot}^{-1}$ for the rotating case, and the values at corresponding metallicity for Iorio et al. 2023 is $1.1 \cdot 10^{-6}\, M_{\odot}^{-1}$.

In this case, we see that the values calculated with the results of simulations using the new stellar wind prescription are higher than the value considered as reference from [24]. As seen in [24], there is still a drop in the value of the merger efficiency for BBHs at a higher metallicity, even though this decrease appears to be shallower than the one found in the other work. However, despite the slightly higher value of η for the non-rotating case with respect to [24], the two numbers are still comparable.

A possible explanation for this phenomenon might be the different scaling in metallicity of the wind prescriptions. Indeed, [24] uses the one by [55], which scales as $\dot{M} \propto Z^{0.85}$. Instead, the wind used in this work, assuming $\alpha = 0.6$, scales like $\dot{M} \propto Z^{(1-\alpha)/\alpha} \simeq Z^{0.68}$. In order to address this phenomenon, further studies will be conducted in the future.

4.4.2 Semi-major axis variation

In this section some plots are presented, that display the variation of the semi-major axis (SMA) of the bound BBHs for the two different metallicities.

SMC

From the comparison between the three different panels in Figure 4.6, it appears clear that there is a general widening of the orbits for both the thick wind cases with respect to the thin wind case, since the area above the red line becomes progressively more populated.

As hinted before, this effect may be due to the influence of the stronger winds, which tend to widen the orbits of the binaries. Another observation can be made regarding the merging BBH. Indeed, in the $\Omega/\Omega_{crit} = 0.6$ case (right panel of Figure 4.6), there is an increase in the density of the population of merging binaries that have a very low initial SMA.

This was actually expected from this kind of configuration: the strong rotation rate makes the stars more compact, preventing them from interacting before becoming a binary compact object. Indeed, by limiting mass transfers and stellar inflation, the systems that would have undergone a stellar merger in non-rotating cases are now able to become BBHs and subsequently merge as a consequence of their reduced SMA.

LMC

For the LMC, the results are displayed in Figure 4.7. There are many similarities between the non-rotating case (center) and [24] (left), as was foreshadowed by the numerical results. For the rotating case, like in the SMC, the wind pushes the binaries to even wider orbits, but is contrasted by the effect of rotation, which increases the number of merging BBH in the small SMA region for the green case, thus explaining the numerical results presented before.

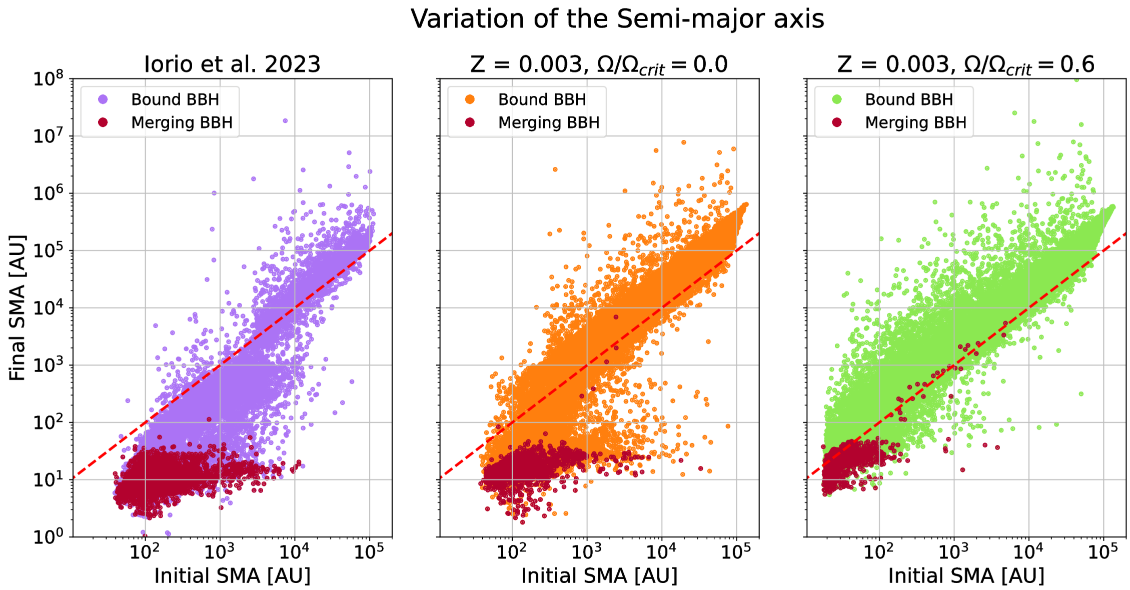

Figure 4.6: Variation of the SMA for bound BBH in the SMC. On the left panel there are the results taken from [24], in the central panel the results for the non-rotating case and on the right the rotating one. On the x-axis is displayed the initial semi-major axis of the binaries, and on the y-axis the final one. With a dark red color are highlighted the binaries that are able to merge within the age of the universe, and with a red line is marked the location on the plot where the initial and the final semi-major axis stays the same through the evolution of the binary.

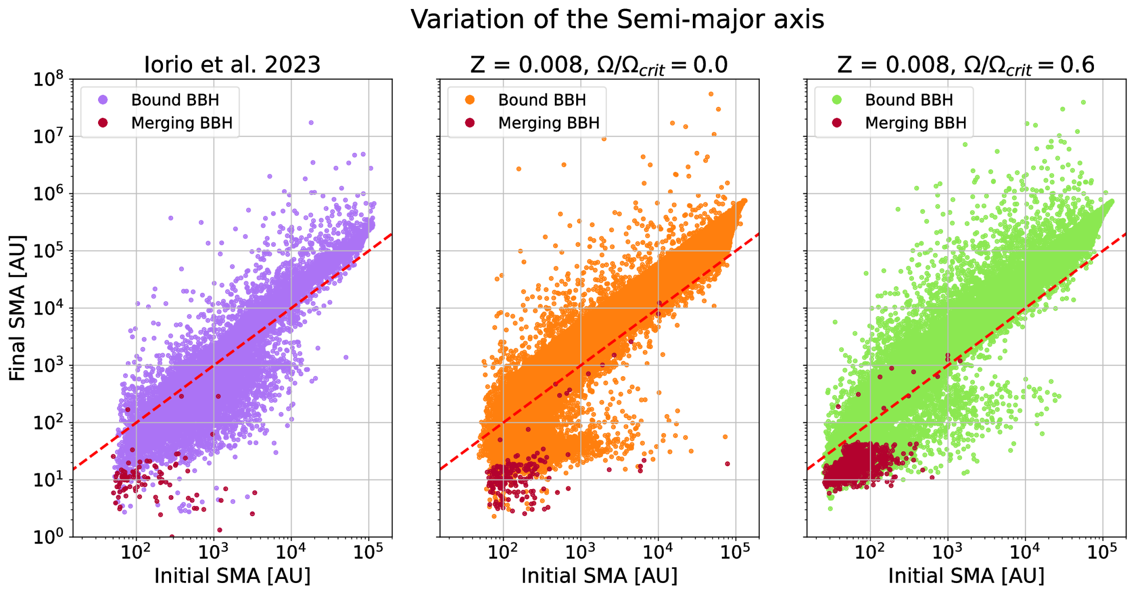

Figure 4.7: Variation of the SMA for bound BBH in the LMC. For the description of the plots, refer to Figure 4.6.

4.4.3 GWtime for bound and merging systems

Here are shown the results for the computation of the merging time for bound BBH systems, identified with the name *GWtime*.

The only disclaimer to make for the histograms in this section, and for further ones, is that comparisons on the absolute numbers can be done only between the non-rotating and rotating case, since they are originated by the same simulated stellar population. Comparisons with [24] should be limited to the shape of the distribution, due to differences in the total population mass and prescription to draw the secondary masses while building the input populations. An accurate numerical comparison will be deferred to future studies.

SMC

For the SMC the results are summarized in Figure 4.8. Comparing both cases with the new wind prescription with the one from Iorio et al. 2023, we can see that the vast majority of the merging systems in the left panel has a quite low merging time, meaning these systems have formed in a relatively recent time. Conversely, on the center and rightmost panel we can see that the peak of the merging systems histogram is shifted to much higher times, meaning that in these cases the calculated merger efficiency is influenced not only by very recently formed BBH (like in the first case) but also by much older systems. This is due to the widening effect of stronger stellar winds on the binaries.

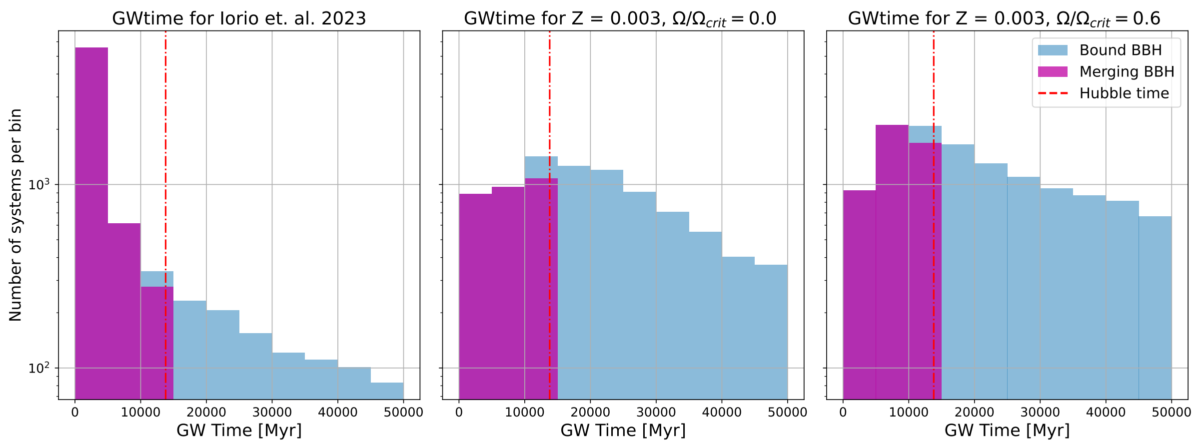

Figure 4.8: Gwtime distribution for bound binaries at the SMC metallicity. The histogram of the merging time for bound BBH is displayed in blue, for the three cases explained before, with on top another histogram showing only the merging BBH (purple). With a red stripe is identified the merging time equal to the age of the universe: systems with a GWtime smaller than this value are classified as mergers.

LMC

Regarding LMC metallicity, the results are shown in Figure 4.9. In this case, the time delay distribution of the non-rotating case shows similarities to the one by [24]. A general increase in the total amount of bound BBHs is visible. That might be attributed to a combination of the stripping effect of the wind and, in the rotating case (right panel), of the compactness due to rotation. These effects both contribute to reducing the interactions among stars and preventing their inflation, thus reducing the number of stellar mergers at the expense of increasing the number of BCOs.

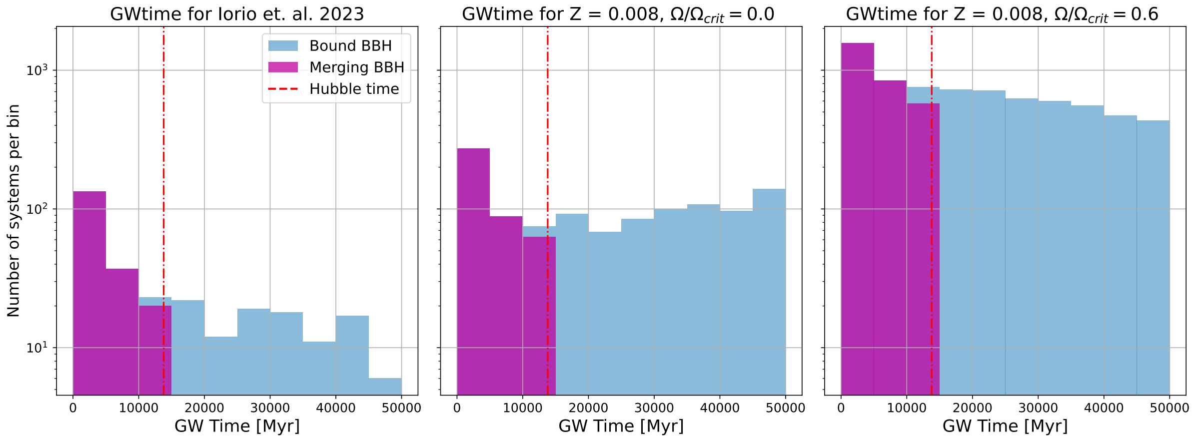

Figure 4.9: Gwtime distribution for bound binaries at the LMC metallicity. For further information about the plots, refer to Figure 4.8.

4.4.4 Final Semi-major axis

In this section, histograms displaying the distributions of SMAs of binary systems will be shown.

SMC

In Figure 4.10, it is shown the histogram for the semi-major axis for each different final state of the binary.

By comparing the two panels in Figure 4.10, it appears very clear the effect of the rotation (right), especially at low semi-major axes. Indeed, when stars rotate, the fraction of stellar mergers at low separation decreases dramatically due to the higher compactness and smaller radii of the stars. In this case, the number of merging BBH at low separation increases significantly. Another effect that is possible to notice is that for the non-rotating case (left panel of Figure 4.10), at higher separation there is an increased number of broken BBH. This shows the influence of strong stellar winds, while the rotating case (right) showcases less broken systems, hinting at an increased binding of the system due to rotation.

Moving now to Figure 4.11, comparing the [24] case (left) to the other two cases, it is possible to see that the peak of the distribution of initial SMA in [24] seems to significantly move toward lower values in the final SMA histogram. This is showing that binaries are able to become tighter and closer together at the end of their evolution. Considering stronger winds, like in the central plot, the shift to the left of the peak appears less pronounced than in the leftmost case, but still visible. Finally in the last case the position of the peak moves very slightly comparing the initial and the final distribution, showing once more the effect of the wind, that keeps stars far away from each other.

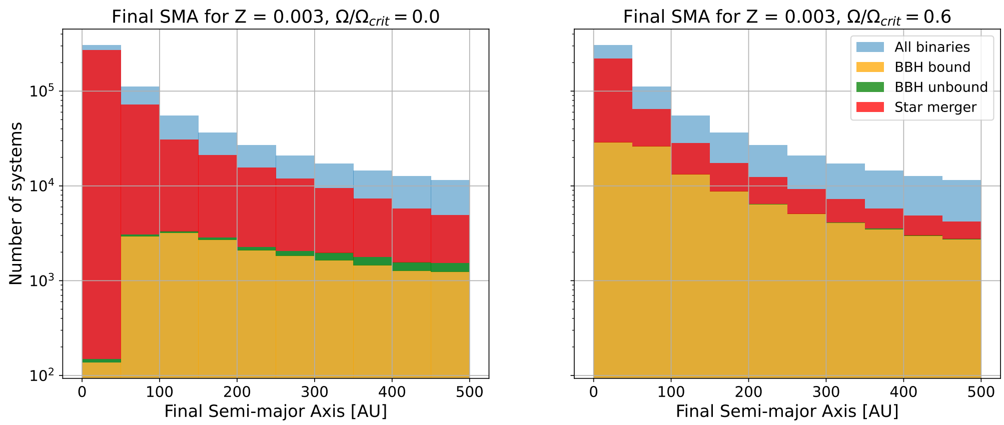

Figure 4.10: SMA as a function of the final fate, SMC metallicity. For each bin of the histogram, in yellow are represented the bound BBH, in green the BBH that end up breaking during the course of their evolution, and in red the systems that undergo a stellar merger. Finally, a blue histogram is plotted behind the other one, showcasing the distribution of initial SMAs for the whole population of binaries. On the left panel is shown the plot relative to the non-rotating case, while the rotating case is on the right.

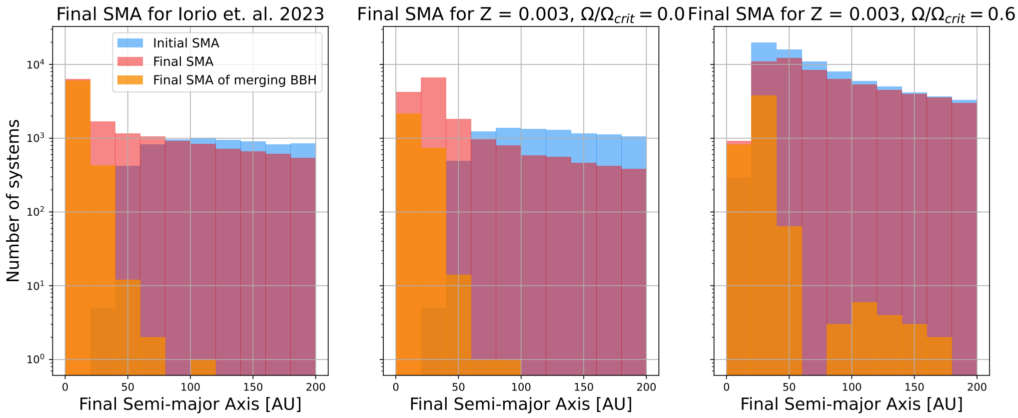

Figure 4.11: Initial vs final distribution of SMA, SMC metallicity. On top of each other are shown the histogram for the distribution of the initial SMAs for all the bound BBH (blue), the one for the final SMA of all the bound BBH (pink), and the final SMAs only for merging BBH (orange), for the three different analyzed cases.

Finally, in Figure 4.12, just the final SMA distribution for bound BBH (blue) and merging BBH (green) are shown. In this case, just as in the histogram for the GWtime (see Figure 4.8), there is a separation between the SMA values that might lead to a merger (SMA $\lesssim$ 50 AU) and those that are too far away, even if in this case the separation is less strict with respect to the GWtime one.

Indeed, the maximum GWtime value that the merger time could assume to lead to a merger is equal to one Hubble time, while in this case there is no upper boundary for the value of the SMA. Even though, in general, higher values of the SMA lead to a higher GWtime because the orbit is wider, the dependency is not so simple. Instead, there is a set of equations in Peters 1964 [54] that describe the relationship between semi-major axis, time, eccentricity, and GWtime, shown below:

- **Decay of the semi-major axis**:

$$\frac{da}{dt} = -\frac{64}{5c^5} G^3 M^3 \frac{q}{a^3(1+q)^2} f(e) \tag{4.9}$$

  where a is the SMA, $M = M_1 + M_2$ is the total mass of the system, q is the mass ratio, e is the eccentricity of the system and $f(e)$ is

$$f(e) = \frac{1 + \frac{73}{24}e^2 + \frac{37}{96}e^4}{(1-e^2)^{7/2}} \tag{4.10}$$

- **Decay of eccentricity**:

$$\frac{de}{dt} = -\frac{304}{15c^5} G^3 M^3 \frac{q}{a^4(1-e^2)^{5/2}(1+q)^2}\, e \left(1 + \frac{121}{304}e^2\right) \tag{4.11}$$

- **Merging time or "Peters time-scale"**:

$$t_P = \frac{5c^5(1+q)^2}{256 G^3 M^3 q} \cdot \frac{a_0^4}{f(e_0)} \tag{4.12}$$

  which is an analytic expression for the time-scale over which the orbit decays due to radiation of gravitational waves, and where e_0 and a_0 are, respectively, the initial eccentricity and the initial SMA.

Instead of behaving just like a distribution inversely proportional to the GWtime, the SMA has a slightly more complex configuration. Indeed, there are peaks in the SMA of merging BBHs even at relatively high values, as can be seen in Figure 4.12. This is probably due to systems that might have higher eccentricities, and are able to coalesce despite the orbit being fairly wide.

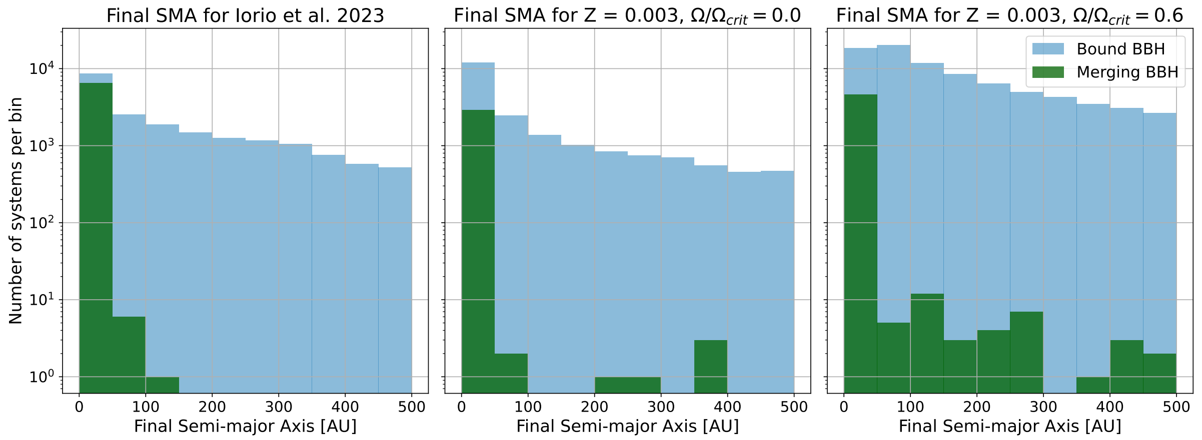

Figure 4.12: Final SMA for bound and merging BBH, SMC metallicity. In this plots are superimposed the histogram of the distribution of final SMA for bound BBHs (blue) and merging BBHs (green).

LMC

The corresponding results for LMC metallicity are shown in Figure 4.13, and are fairly similar to those found for the SMC. Indeed, also in this case a decrease in the number of stellar mergers and broken systems is observed, particularly in the rotating case (right panel) with respect to the non-rotating one (left panel), probably due to the higher rotation.

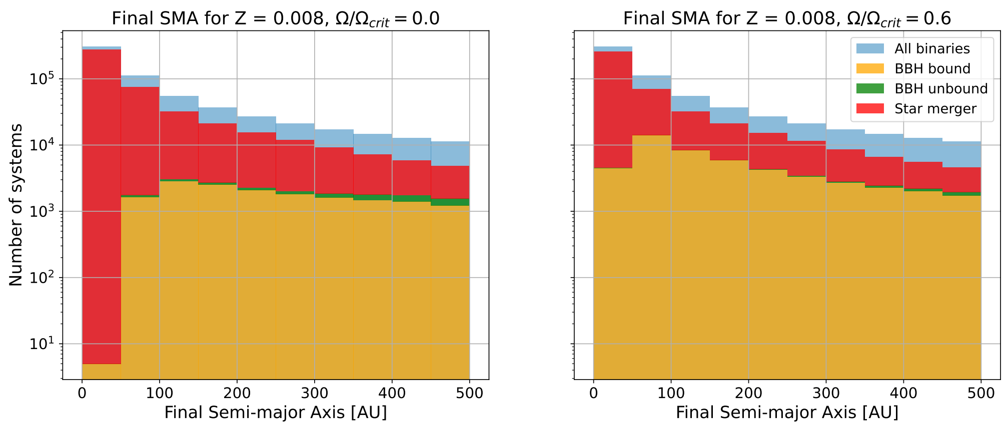

Figure 4.13: SMA as a function of the final fate, LMC metallicity. For further information about the plot, refer to Figure 4.10.

In Figure 4.14, there is a visible shift of the peak from the distribution of initial SMAs to the one of final SMAs. This is in contrast with what observed in the SMC, since it is expected from winds to keep binaries wide. This feature generates the difference in the GWtime distribution seen for the LMC with respect to the one for the SMC. Indeed, for the LMC, the merging time has a distribution similar to [24], instead of being peaked at higher values.

Finally, as can be seen in Figure 4.15, despite the three distribution looking apparently more similar for LMC metallicity than for SMC one, some distinct peaks are still visible at higher SMA values. This shows once again the impact on the chance of coalescence of systems to be depending not only on the SMA or GWtime, but also on a possible influence of eccentricity.

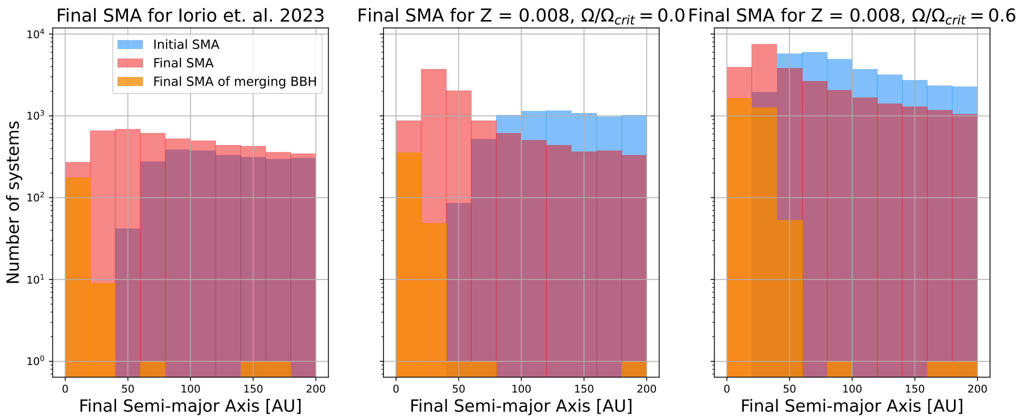

Figure 4.14: Initial vs final distribution of SMA, LMC metallicity. For further information about the plot, refer to Figure 4.11.

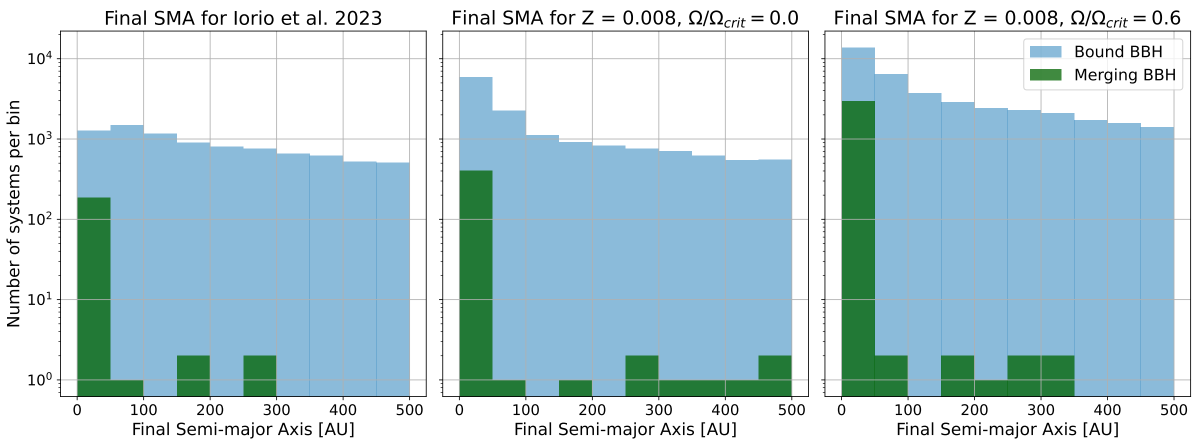

Figure 4.15: Final SMA for bound and merging BBH, LMC metallicity. For further information on this plot, refer to Figure 4.12.

4.4.5 Initial and Remnant mass of the primary star

In this section some histograms concerning the distribution of the mass of the primary star in the binary system are shown.

SMC

Figure 4.16 displays the distribution of initial primary masses for systems with different final fates. It is clearly visible that at lower initial masses the binary tends to either undergo a stellar merger or end up broken in the non-rotating case, while stronger winds combined with rotation are preventing the majority of stellar mergers thus increasing the number of bound BBHs.

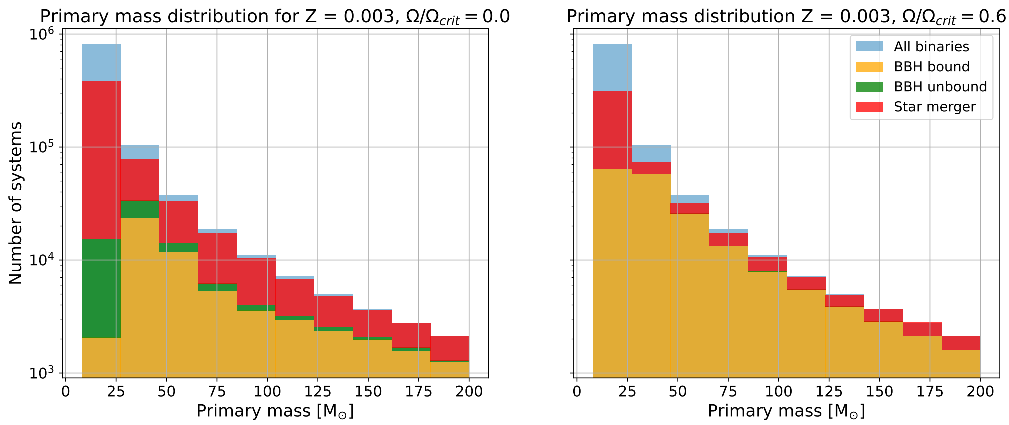

Figure 4.16: Distribution of the primary mass as a function of the final fate, SMC metallicity. The figure shows two histograms on top of each other: the first one is in blue and represents the distribution of primary masses for all the binary systems, while for the second in each bin the bound BBH are shown in yellow, the stellar mergers in red and the broken binary systems in green. In the left panel are shown the results for the non-rotating case, while those relative to the rotating one are on the right.

In Figure 4.17, it is possible to compare the results of this work with those of [24]. It is evident that, while in the latter case the distribution of remnant masses is kind of uniform and slightly shifted to lower values, in the other cases the situation is fairly different. Indeed, in the non-rotating case (center) the effect of strong winds makes the remnant masses' distribution more peaked toward lower values, with a sudden drop at about 40-50 $M_\odot$. There is probably visible the consequence of the activation of stronger optically thick winds, that prevent the formation of massive BHs. In the rotating case (right), the situation is similar to that of the central plot. However, due to the activation of optically thick winds at even smaller masses, the drop in the remnant masses' distribution occurs more suddenly and at lower masses ($\simeq 30\,M_\odot$).

Interestingly enough, for the thick wind cases in Figure 4.17, there is a peak in the distribution of the remnant masses at around 35 $M_\odot$. In the rotating case this peak is more clearly visible, and another peak is shown at around 17 $M_\odot$. This distribution is very peculiar and was also found in the astrophysical BBH primary mass inferred by the LVK collaboration from GWTC-2 and GWTC-3 data. The result is shown in Figure 4.18 below, taken from [56].

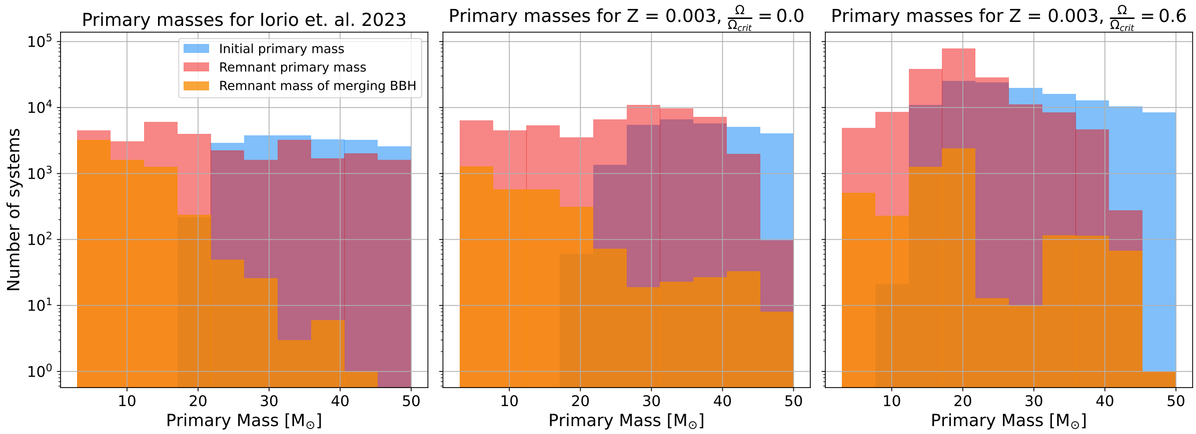

Figure 4.17: Initial vs final distribution of primary masses, SMC metallicity. In this figure, three different histograms are shown, one for the distribution of the initial primary masses of bound BBH (blue), one for the mass of the remnants produced by the primary star (pink) , and the last (orange) is the same as the pink one but restricted to bound BBH that merge within a Hubble time. The case by [24] is on the left panel, while the ones treated in this work are, respectively, the non-rotating (center) and rotating (right).

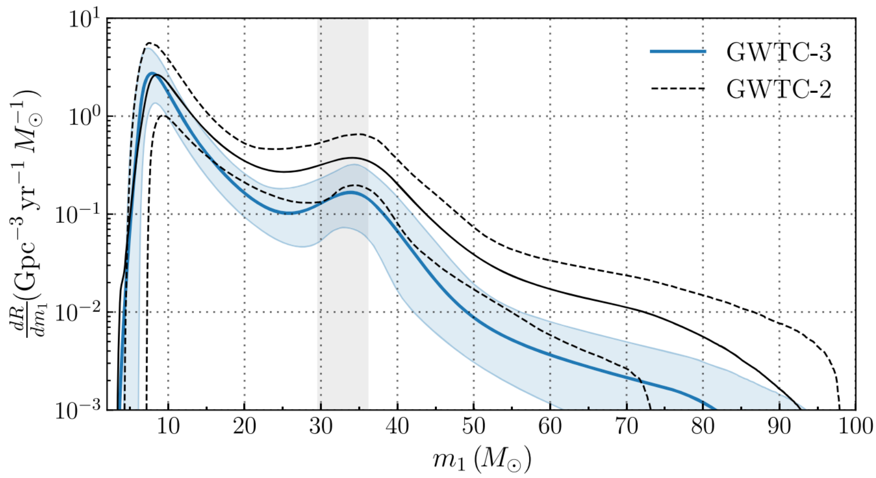

Figure 4.18: Inference on the astrophysical primary mass from GWTC-3. The solid blue curve shows the posterior population distribution with the shaded region showing the 90% credible interval

LMC

Results regarding the distribution of initial primary masses in the LMC are shown in Figure 4.20 as a function of the different final fates of the binaries. In this case there is a relatively high amount of broken binaries at lower masses in the non-rotating case, that then gets almost completely (but not totally) converted into bound BBHs when rotation is activated, mainly due to the effect of rotation. The higher amount of broken systems, instead, might be due to the widening of lighter binaries due to stronger winds: the higher mass-loss effects are indeed still present and visible, despite the numerical result for the merger efficiency apparently hinting otherwise.

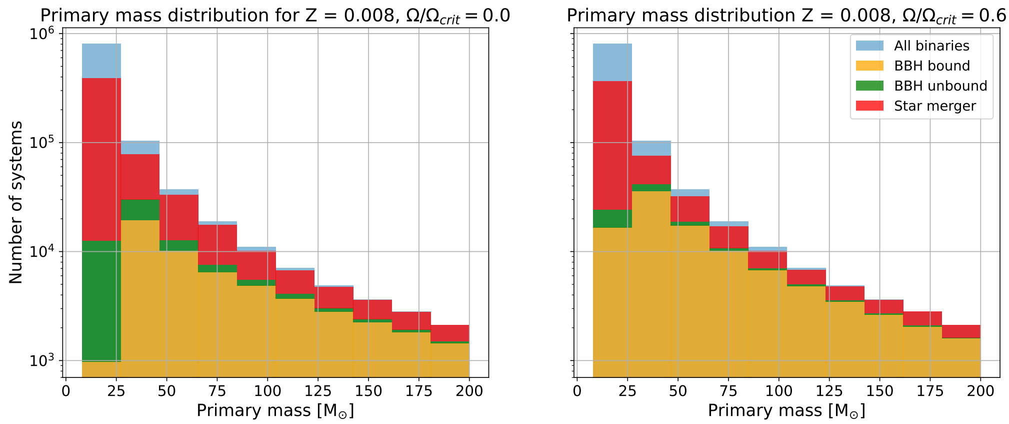

Figure 4.19: Distribution of the primary mass as a function of the final fate, LMC metallicity. For further information regarding the plot, see Figure 4.16

For the primary masses' distribution, shown in Figure 4.20, the only differences from the SMC case are in the peak of the distribution of the remnant masses. This peak is more pronounced and shifted to lower values, highly likely due to stronger winds stripping the stars more than in the SMC case, and a less visible peak around 17 $M_\odot$ for the remnant mass of merging BBHs.

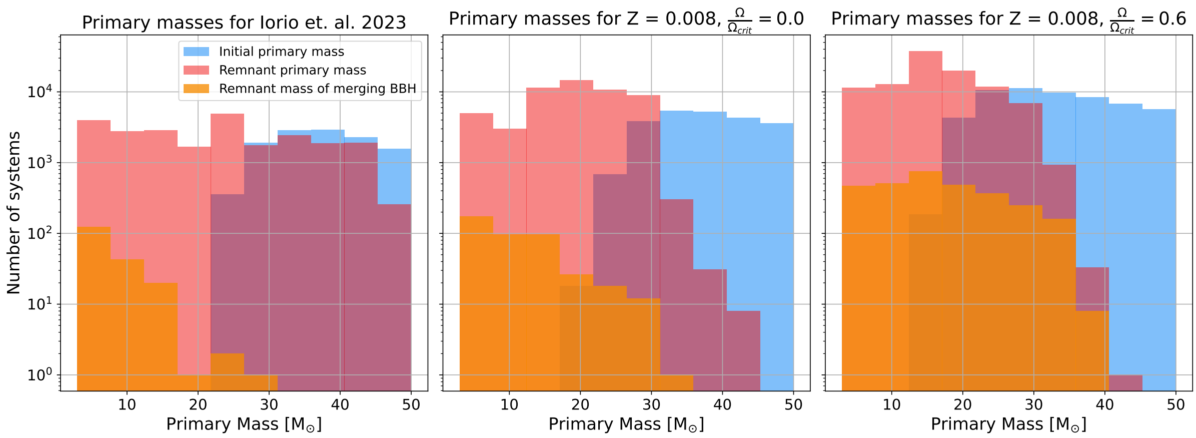

Figure 4.20: Initial vs final distribution of primary masses, LMC metallicity. For further information on this plot, refer to Figure 4.17.

4.4.6 Relations among the variables

In the final scatter plots shown in Figures 4.21 - 4.24 are showcased the relations between different variables. The plots are displayed firstly considering the population of all the bound BBH systems, and then only for the subset of the previous group constituted by merging BBH systems.

SMC

Observing the plot in Figure 4.21, relative to bound BBHs, and comparing the leftmost panel with the other two, it is possible to see once again the effect of strong winds, that tend to shift the majority of the population to the right, so towards higher SMA. Moreover, it appears that the GWtimes get progressively longer, in agreement with what was previously found to be another effect of the high mass loss.

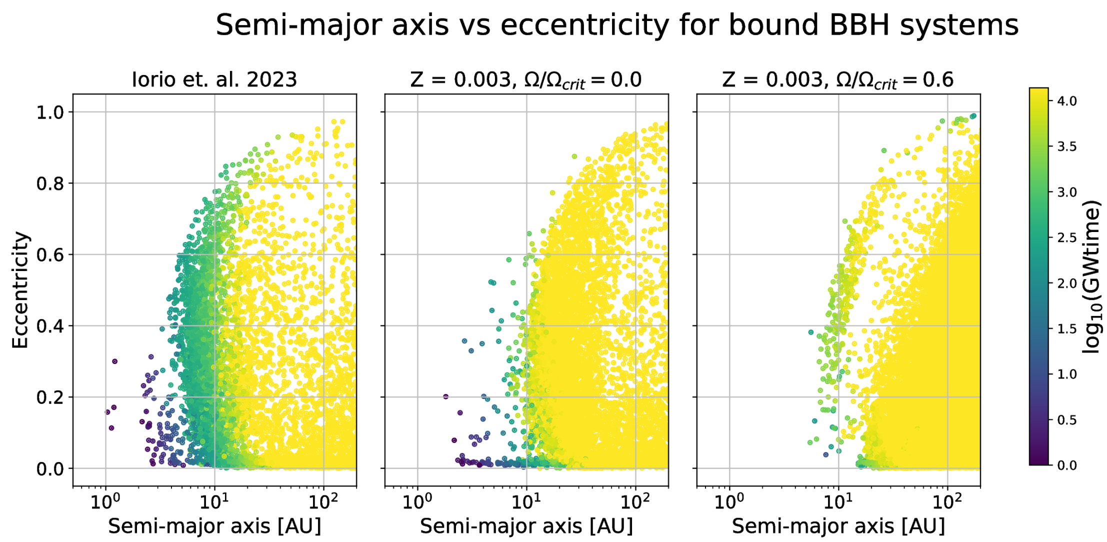

Figure 4.21: Relation between SMA and eccentricity for bound BBH systems, SMC metallicity. On the x-axis it is considered the SMA, on the y-axis the eccentricity and the logarithm of the GWtime is shown with a colormap. The case by [24] is on the left panel, while the ones treated in this work are, respectively, the non-rotating (center) and rotating (right).

Shifting the focus now to the plots in Figure 4.22, the one for only merging BBHs, it immediately shows that for the new mass loss prescription the elements of the population have significantly larger GWtimes. This is coherent with the previous plot and, in the case of rotating stars (right), they span a significantly smaller interval of SMA with respect to the plot with the results by [24] (left).

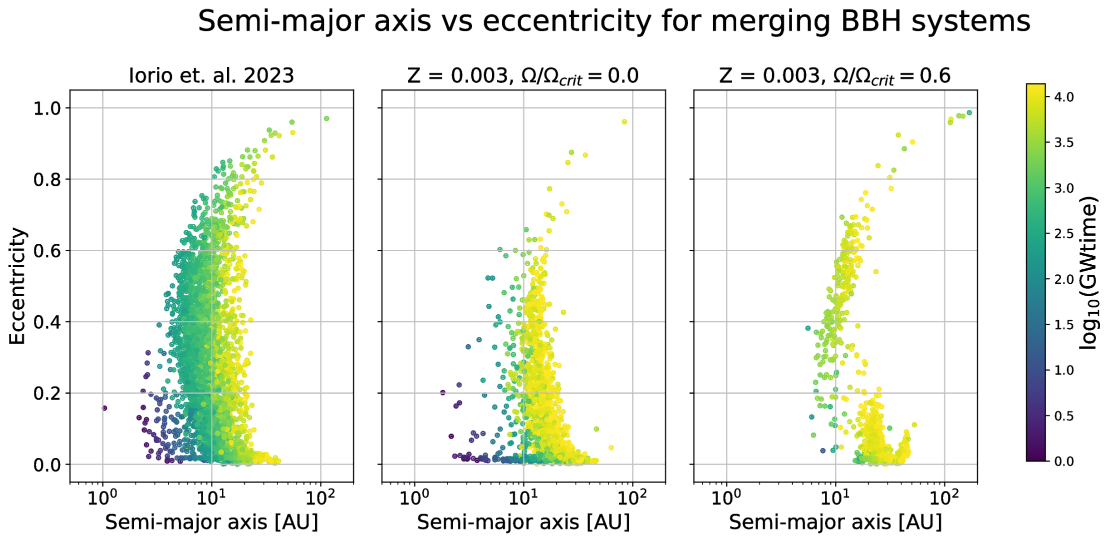

Figure 4.22: Relation between SMA and eccentricity for merging BBH systems, SMC metallicity. For further information regarding the plot, see Figure 4.21.

LMC

Concerning the LMC results, shown in Figure 4.23, they are once again similar to the ones presented for the SMC, except for an enhancement of some features. An example of this phenomenon is showcased by comparing the plot for the rotating case (right) with that relative to [24] (left): the population in the right one is significantly shifted to higher SMA, as a consequence of the wind mass loss.

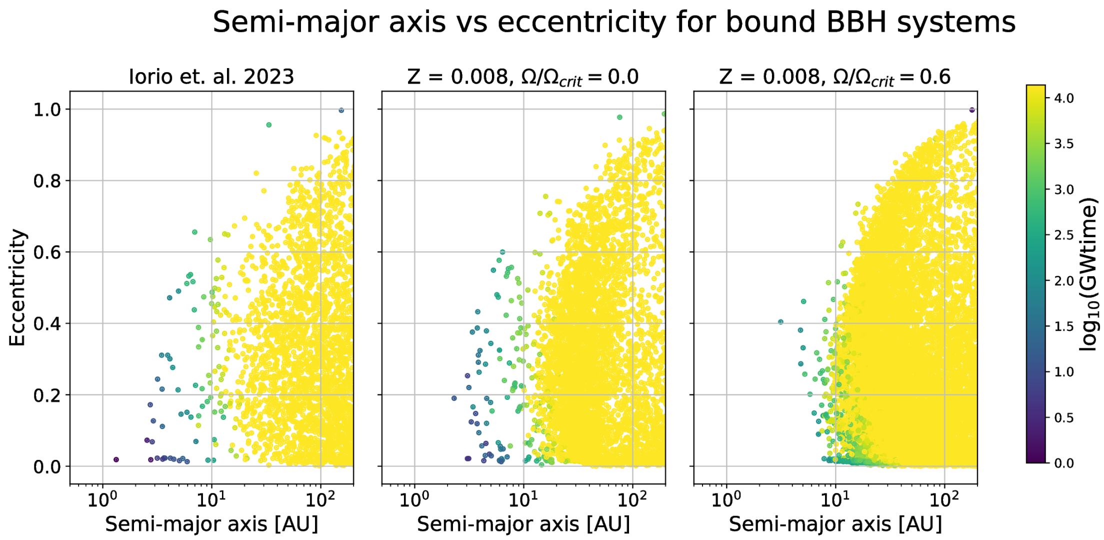

Figure 4.23: Relation between SMA and eccentricity for bound BBH systems, LMC metallicity. For further information regarding the plot, see Figure 4.21.

Finally we consider Figure 4.24, relative to merging BBHs. On top of noticing an increase in the number of systems (the reason of which have been explained in the previous sections), it is possible to see a general increase in the GWtime, coherently with expectations.

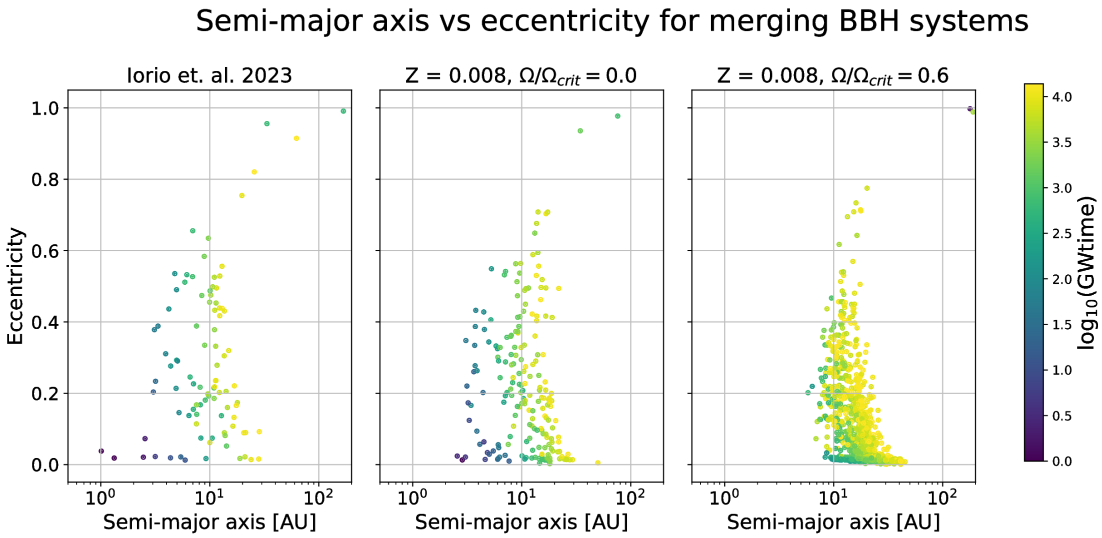

Figure 4.24: Relation between SMA and eccentricity for merging BBH systems, LMC metallicity. For further information regarding the plot, see Figure 4.21.

Chapter 5

Conclusion

In this work, Wolf-Rayet stars and their winds have been studied by analyizing their evolution with a new model of optically thick stellar winds, originally published in Bestenlehner 2020 [22]. The impact of this wind model has been studied both on the evolution of single and binary stars, with the aim of calculating the binary black hole merger efficiency for different values of metallicity and stellar rotation rates.

The model developed by Bestenlehner is characterized by its simplicity, and by the possibility for the star to undergo a transition from optically thin to optically thick winds, thus providing a unique recipe for the mass loss for two completely different mass loss regimes. The produced stellar winds, especially for stars that are able to enter the optically thick regime, result to be significantly higher and more intense with respect to other models employed in previous works, particularly compared with widely used optically thin wind models like the one in Vink 2001 [55].

Through the use of the 1D hydrostatic stellar evolution code MESA, some single stellar tracks have been produced for initial masses ranging from 10 to 320 $M_{\odot}$, considering the metallicity of both the Small and the Large Magellanic Cloud, and two different rotational rates per each metallicity, expressed in terms of the critical rotational velocity: $\Omega/\Omega_{crit} = 0.0$, 0.6.

For the non-rotating stars, stellar tracks with initial masses lower than 60 (for the SMC) and 45 (for the LMC) mostly evolve via optically thin winds. However, even if they are able to enter the optically thick wind regime, they do so only at the end of their evolution, where they usually inflate a lot and cool down on the rightmost part of the HR diagram. Instead, stars that have masses above these thresholds are able to activate thick winds before their final stages of evolution, and undergo an effective self-stripping that increases their temperature. This brings them towards the hotter side of the HR diagram, making their stellar tracks able to cross the observational points of actual WR in the Magellanic Clouds.

Concerning rotating stars, the models are able to enter a chemically homogeneous evolution regime, becoming hotter and more luminous. This increased luminosity helps the stars enter the optically thick wind regime starting from lower masses with respect to the non-rotating case, moving the threshold to 22 in the SMC and to 20 in the LMC. Such a decrease in the threshold for thick winds activation allows us to reproduce observed WRs with luminosities $\log L/L_{\odot} \lesssim 6$, which are difficult to produce in models with only thin winds.

The produced stellar tracks have then been processed to be used as an input for the population synthesis code SEVN, where 4 different simulations have been run (2 different metallicities and 2 rotational rates per each metallicity), considering a population of 10^6 binary systems, with primary masses going from 8 to 200 $M_\odot$.

The outputs of these runs have then been compared with each other and with the data obtained by Iorio et al. 2023 [24], used as a reference for the results of stellar models employing optically thin wind models. The main conclusions that can be drawn from the analysis of these runs are summarized as follows:

- Stronger stellar winds produce a substantial widening in the binaries, that decrease the amount of merging BBH systems. This effect lowers the value of the merger efficiency with respect to the optically thin case showed in [24]. Indeed, if the latter obtains $\eta \simeq 3.72 \cdot 10^{-5}$ in the SMC, the non-rotating stars in this work produce $\eta \simeq 1.03 \cdot 10^{-5}$, almost 4 times smaller.
- Higher rotational rates produce stars that stay more compact and do not inflate significantly during their evolution, preventing binary interactions and especially stellar mergers. In this way, even tight systems are able to survive their evolution and produce compact remnants, thus effectively increasing the fraction of bound BBHs in the population with respect to the non-rotating case. As a result, a significant amount of tight BBHs is added to the balance of the population.
- The higher number of tightly bound BBH generated by the systems that avoid undergoing a stellar merger in the rotating case, contribute to increase the fraction of BBHs that merge within a Hubble time. As a result, there is an apparent increase in the merger efficiency with respect to the non-rotating scenario, obtaining $\eta \simeq 1.65 \cdot 10^{-5}$ for the SMC metallicity. However, this increase is not due to a wrong modelization, but simply to the competition of two opposite effects: the one from strong winds, widening the binaries and breaking the bigger systems, and the one from rotation, generating merging BBHs from systems that would have merged before becoming BCOs.

For the LMC similar effects are observed, even though the merger efficiency values obtained in this work result to be higher than the one calculated in [24]. However, in agreement with [24], a drop in the merger efficiency is still observed, despite being shallower than [24]. As hypothesized in 4.4.1, this effect might be due to the different scaling in metallicity of the employed wind prescriptions.

In any case, it is important to keep in mind that this work presents a pioneering study to understand how the merger efficiency of BBHs might vary in case of optically thick winds and especially in the case of rotating stars. In order to get a more complete overview of the impact of these factors on η_{BBH} and, subsequently, on the merger rate density $\mathcal{R}_{BBH}$, it will be necessary to continue the analysis in a future study, where grids for different values of rotational rates and metallicities will be used, hopefully producing results that are able to solve the overestimation problem of the merger rate density at small redshifts.

Bibliography

[1] Cecilia Sgalletta, Michela Mapelli, Lumen Boco, Filippo Santoliquido, M. Celeste Artale, Giuliano Iorio, Andrea Lapi, and Mario Spera. The more accurately we model the metal-dependent star formation rate, the larger the predicted excess of binary black hole mergers, 2024.

[2] Leindert A Boogaard, Jarle Brinchmann, Nicolas Bouché, Mieke Paalvast, Roland Bacon, Rychard J Bouwens, Thierry Contini, Madusha LP Gunawardhana, Hanae Inami, Raffaella A Marino, et al. The muse hubble ultra deep field survey-xi. constraining the low-mass end of the stellar mass–star formation rate relation at z< 1. *Astronomy & Astrophysics*, 619:A27, 2018.

[3] Joshua S Speagle, Charles L Steinhardt, Peter L Capak, and John D Silverman. A highly consistent framework for the evolution of the star-forming “main sequence” from z 0–6. *The Astrophysical Journal Supplement Series*, 214(2):15, 2014.

[4] Paola Popesso, A Concas, Giovanni Cresci, S Belli, G Rodighiero, H Inami, M Dickinson, O Ilbert, M Pannella, and D Elbaz. The main sequence of star-forming galaxies across cosmic times. *Monthly Notices of the Royal Astronomical Society*, 519(1):1526–1544, 2023.

[5] Filippo Santoliquido, Michela Mapelli, Nicola Giacobbo, Yann Bouffanais, and M Celeste Artale. The cosmic merger rate density of compact objects: impact of star formation, metallicity, initial mass function, and binary evolution. *Monthly Notices of the Royal Astronomical Society*, 502(4):4877–4889, 2021.

[6] Erika Korb. Compact objects with wolf-rayet companions: a key binary configuration to produce gravitational wave mergers. *Bulletin de la Societe Royale des Sciences de Liege*, 93(3):363–373, 2024.

[7] A Schootemeijer, Tomer Shenar, N Langer, N Grin, Hugues Sana, G Gräfener, C Schürmann, C Wang, and X-T Xu. An absence of binary companions to wolf-rayet stars in the small magellanic cloud-implications for mass loss and black hole masses at low metallicities. *Astronomy & Astrophysics*, 689:A157, 2024.

[8] Avishai Gilkis, Tomer Shenar, Varsha Ramachandran, Adam S Jermyn, Laurent Mahy, Lidia M Oskinova, Iair Arcavi, and Hugues Sana. The excess of cool supergiants from contemporary stellar evolution models defies the metallicity-independent humphreys–davidson limit. *Monthly Notices of the Royal Astronomical Society*, 503(2):1884–1896, 2021.

[9] Sylvia Ekström. Evolution and final fates of massive stars, 2025.

[10] Alexander Heger, Bernhard Müller, and Ilya Mandel. Black holes as the end state of stellar evolution: Theory and simulations, 2023.

[11] Marco Limongi and Alessandro Chieffi. Presupernova evolution and explosion of massive stars. *Journal of Physics: Conference Series*, 202(1):012002, jan 2010.

[12] H Von Zeipel. The radiative equilibrium of a rotating system of gaseous masses. *Monthly Notices of the Royal Astronomical Society, Vol. 84, p. 665-683*, 84:665–683, 1924.

[13] A. Maeder and G. Meynet. Stellar evolution with rotation. VI. The Eddington and Omega -limits, the rotational mass loss for OB and LBV stars. , 361:159–166, September 2000.

[14] Ines Brott, Selma E De Mink, Matteo Cantiello, Norbert Langer, Alex de Koter, Chris J Evans, Ian Hunter, Carrie Trundle, and Jorick S Vink. Rotating massive main-sequence stars-i. grids of evolutionary models and isochrones. *Astronomy & Astrophysics*, 530:A115, 2011.

[15] Falk Herwig. The evolution of agb stars with convective overshoot. *arXiv preprint astro-ph/0007139*, 2000.

[16] John I Castor, David C Abbott, and Richard I Klein. Radiation-driven winds in of stars. *Astrophysical Journal, vol. 195, Jan. 1, 1975, pt. 1, p. 157-174.*, 195:157–174, 1975.

[17] Joachim Puls, Jorick S Vink, and Francisco Najarro. Mass loss from hot massive stars. *The Astronomy and Astrophysics Review*, 16:209–325, 2008.

[18] J Puls, U Springmann, and M Lennon. Radiation driven winds of hot luminous stars-xiv. line statistics and radiative driving. *Astronomy and Astrophysics Supplement Series*, 141(1):23–64, 2000.

[19] Jorick S. Vink, L. E. Muijres, B. Anthonisse, A. de Koter, G. Gräfener, and N. Langer. Wind modelling of very massive stars up to 300 solar masses. , 531:A132, July 2011.

[20] Alex de Koter, Sara R. Heap, and Ivan Hubeny. On the Evolutionary Phase and Mass Loss of the Wolf-Rayet–like Stars in R136a. , 477:792, March 1997.

[21] Paul A. Crowther and Nolan R. Walborn. Spectral classification of O2-3.5 If*/WN5-7 stars. , 416(2):1311–1323, September 2011.

[22] Joachim M Bestenlehner. Mass loss and the eddington parameter: a new mass-loss recipe for hot and massive stars. *Monthly Notices of the Royal Astronomical Society*, 493(3):3938–3946, 2020.

[23] Roberta M Humphreys and Kris Davidson. Studies of luminous stars in nearby galaxies. iii-comments on the evolution of the most massive stars in the milky way and the large magellanic cloud. *Astrophysical Journal, Part 1, vol. 232, Sept. 1, 1979, p. 409-420.*, 232:409–420, 1979.

[24] Giuliano Iorio, Michela Mapelli, Guglielmo Costa, Mario Spera, Gastón J Escobar, Cecilia Sgalletta, Alessandro A Trani, Erika Korb, Filippo Santoliquido, Marco Dall'Amico, et al. Compact object mergers: exploring uncertainties from stellar and binary evolution with sevn. *Monthly Notices of the Royal Astronomical Society*, 524(1):426–470, 2023.

[25] Joachim M Bestenlehner, Götz Gräfener, Jorick S Vink, F Najarro, Alex de Koter, Hugues Sana, CJ Evans, PA Crowther, V Hénault-Brunet, A Herrero, et al. The vlt-flames tarantula survey-xvii. physical and wind properties of massive stars at the top of the main sequence. *Astronomy & Astrophysics*, 570:A38, 2014.

[26] Bill Paxton, Lars Bildsten, Aaron Dotter, Falk Herwig, Pierre Lesaffre, and Frank Timmes. Modules for Experiments in Stellar Astrophysics (MESA). , 192(1):3, January 2011.

[27] Bill Paxton, Matteo Cantiello, Phil Arras, Lars Bildsten, Edward F. Brown, Aaron Dotter, Christopher Mankovich, M. H. Montgomery, Dennis Stello, F. X. Timmes, and Richard Townsend. Modules for Experiments in Stellar Astrophysics (MESA): Planets, Oscillations, Rotation, and Massive Stars. , 208(1):4, September 2013.

[28] Bill Paxton, Pablo Marchant, Josiah Schwab, Evan B. Bauer, Lars Bildsten, Matteo Cantiello, Luc Dessart, R. Farmer, H. Hu, N. Langer, R. H. D. Townsend, Dean M. Townsley, and F. X. Timmes. Modules for Experiments in Stellar Astrophysics (MESA): Binaries, Pulsations, and Explosions. , 220(1):15, September 2015.

[29] Bill Paxton, Josiah Schwab, Evan B. Bauer, Lars Bildsten, Sergei Blinnikov, Paul Duffell, R. Farmer, Jared A. Goldberg, Pablo Marchant, Elena Sorokina, Anne Thoul, Richard H. D. Townsend, and F. X. Timmes. Modules for Experiments in Stellar Astrophysics (MESA): Convective Boundaries, Element Diffusion, and Massive Star Explosions. , 234(2):34, February 2018.

[30] Bill Paxton, R. Smolec, Josiah Schwab, A. Gautschy, Lars Bildsten, Matteo Cantiello, Aaron Dotter, R. Farmer, Jared A. Goldberg, Adam S. Jermyn, S. M. Kanbur, Pablo Marchant, Anne Thoul, Richard H. D. Townsend, William M. Wolf, Michael Zhang, and F. X. Timmes. Modules for Experiments in Stellar Astrophysics (MESA): Pulsating Variable Stars, Rotation, Convective Boundaries, and Energy Conservation. , 243(1):10, July 2019.

[31] Joachim M Bestenlehner. Mass loss and the eddington parameter. *Proceedings of the International Astronomical Union*, 18(S361):163–167, 2022.

[32] Gautham N. Sabhahit, Jorick S. Vink, Andreas A. C. Sander, and Erin R. Higgins. Very massive stars and pair-instability supernovae: mass-loss framework for low metallicity. , 524(1):1529–1546, September 2023.

[33] Lumen Boco, Michela Mapelli, Andreas AC Sander, Sofia Mesini, Varsha Ramachandran, Stefano Torniamenti, Erika Korb, Boyuan Liu, Gautham N Sabhahit, and Jorick S Vink. Metal-poor single wolf-rayet stars: the interplay of optically thick winds and rotation. *arXiv preprint arXiv:2507.00137*, 2025.

[34] Filippo Simonato, Stefano Torniamenti, Michela Mapelli, Giuliano Iorio, Lumen Boco, Franca De Domenico-Langer, and Cecilia Sgalletta. Impact of stellar winds on the pair-instability supernova rate. *arXiv preprint arXiv:2505.07959*, 2025.

[35] C. de Jager, H. Nieuwenhuijden, and K. A. van der Hucht. Mass Loss Rates in the Hertzprung-Russell Diagram. *Bulletin d'Information du Centre de Donnees Stellaires*, 35:141, December 1988.

[36] Andreas A. C. Sander and Jorick S. Vink. On the nature of massive helium star winds and Wolf-Rayet-type mass-loss. , 499(1):873–892, November 2020.

[37] Jorick S. Vink. Winds from stripped low-mass helium stars and Wolf-Rayet stars. , 607:L8, November 2017.

[38] R. Hainich, D. Pasemann, H. Todt, T. Shenar, A. Sander, and W. R. Hamann. Wolf-Rayet stars in the Small Magellanic Cloud. I. Analysis of the single WN stars. , 581:A21, September 2015.

[39] V. Ramachandran, W. R. Hamann, L. M. Oskinova, J. S. Gallagher, R. Hainich, T. Shenar, A. A. C. Sander, H. Todt, and L. Fulmer. Testing massive star evolution, star formation

history, and feedback at low metallicity. Spectroscopic analysis of OB stars in the SMC Wing. , 625:A104, May 2019.

[40] M. J. Rickard, R. Hainich, D. Pauli, W. R. Hamann, L. M. Oskinova, R. K. Prinja, V. Ramachandran, H. Todt, E. C. Schösser, A. A. C. Sander, and P. Zeidler. Determining stellar properties of massive stars in NGC346 in the SMC with a Bayesian statistic technique. , 692:A149, December 2024.

[41] J. M. Bestenlehner, Paul A. Crowther, V. A. Bronner, S. Simón-Díaz, D. J. Lennon, J. Bodensteiner, N. Langer, P. Marchant, H. Sana, F. R. N. Schneider, and T. Shenar. Binarity at LOw Metallicity (BLOeM): Pipeline-Determined Physical Properties of OB Stars. , June 2025.

[42] Guglielmo Costa, Martyna Chruślińska, Jakub Klencki, Floor S Broekgaarden, Carl L Rodriguez, Tana D Joseph, and Sara Saracino. Stellar black holes and compact stellar remnants. In *Black Holes in the Era of Gravitational-Wave Astronomy*, pages 1–148. Elsevier, 2024.

[43] Konstantin Postnov and L. Yungelson. The evolution of compact binary star systems. *Living Reviews in Relativity*, 17, 05 2014.

[44] Peter P Eggleton. Approximations to the radii of roche lobes. *Astrophysical Journal, Part 1 (ISSN 0004-637X), vol. 268, May 1, 1983, p. 368, 369.*, 268:368, 1983.

[45] Cosimo Bambi, Stavros Katsanevas, and Konstantinos D Kokkotas. *Handbook of Gravitational Wave Astronomy*. Springer Nature, 2022.

[46] Jarrod R Hurley, Onno R Pols, and Christopher A Tout. Comprehensive analytic formulae for stellar evolution as a function of mass and metallicity. *Monthly Notices of the Royal Astronomical Society*, 315(3):543–569, 2000.

[47] Onno R. Pols, Klaus-Peter Schröder, Jarrod R. Hurley, Christopher A. Tout, and Peter P. Eggleton. Stellar evolution models for z = 0.0001 to 0.03. *Monthly Notices of the Royal Astronomical Society*, 298(2):525–536, 08 1998.

[48] Michela Mapelli, Nicola Giacobbo, Emanuele Ripamonti, and Mario Spera. The cosmic merger rate of stellar black hole binaries from the illustris simulation. *Monthly Notices of the Royal Astronomical Society*, 472(2):2422–2435, 2017.

[49] Katelyn Breivik, Scott Coughlin, Michael Zevin, Carl L Rodriguez, Kyle Kremer, Claire S Ye, Jeff J Andrews, Michael Kurkowski, Matthew C Digman, Shane L Larson, et al. Cosmic variance in binary population synthesis. *The Astrophysical Journal*, 898(1):71, 2020.

[50] Monica Gallegos-Garcia, Christopher PL Berry, Pablo Marchant, and Vicky Kalogera. Binary black hole formation with detailed modeling: stable mass transfer leads to lower merger rates. *The Astrophysical Journal*, 922(2):110, 2021.

[51] Tassos Fragos, Jeff J Andrews, Simone S Bavera, Christopher PL Berry, Scott Coughlin, Aaron Dotter, Prabin Giri, Vicky Kalogera, Aggelos Katsaggelos, Konstantinos Kovlakas, et al. Posydon: A general-purpose population synthesis code with detailed binary-evolution simulations. *The Astrophysical Journal Supplement Series*, 264(2):45, 2023.

[52] Pavel Kroupa. On the variation of the initial mass function. *Monthly Notices of the Royal Astronomical Society*, 322(2):231–246, 2001.

[53] Hugues Sana, SE De Mink, Alex de Koter, N Langer, CJ Evans, M Gieles, Eric Gosset, RG Izzard, J-B Le Bouquin, and FRN Schneider. Binary interaction dominates the evolution of massive stars. *Science*, 337(6093):444–446, 2012.

[54] Philip Carl Peters. Gravitational radiation and the motion of two point masses. *Physical Review*, 136(4B):B1224, 1964.

[55] Jorick S. Vink, A. de Koter, and H. J. G. L. M. Lamers. Mass-loss predictions for O and B stars as a function of metallicity. , 369:574–588, April 2001.

[56] R. Abbott, T. D. Abbott, F. Acernese, K. Ackley, and Adams et al. Population of merging compact binaries inferred using gravitational waves through gwtc-3. *Phys. Rev. X*, 13:011048, Mar 2023.

Appendix

Notes on the normalization

The normalization technique chosen for this work has been selected mainly for the purpose of keeping the version of the wind recipe adapted for different metallicities as simple as possible, as the original author intended.

Moreover, an additional note has to be made regarding the force multiplier parameter α: indeed, by looking at Table 3 in [18], it is possible to see that this parameter changes slightly with metallicity. In this work, the value of α (which is actually an effective α and in the extended CAK formalism should be called α') has been fixed to 0.6 (after being corrected with the δ parameter).

In order to address the validity of the choice of fixing the value of α and of normalizing the wind recipe using simply a rescaling of the metallicity dependent quantities, different calculations of the $\dot{M}$ have been performed, both for a rotating and a non-rotating star, and shown collectively in Figure 5.1 and 5.2. The $\dot{M}$ from the MESA stellar track is in red, the $\dot{M}$ calculated with the normalization described by equation 3.18 (with the fixed value of alpha) is yellow, the $\dot{M}$ calculated with the formula of the CAK theory (equation 3.8 is in green, and finally the analytic calculation of the whole formula by Bestenlehner 2020 [22] (equation 3.12) is in blue.

For the last two $\dot{M}$ calculations, instead of the value of alpha chosen for the simulations, a different value has been used, obtained by performing a bilinear interpolation in metallicity and temperature of the values in Table 3 of [18]. The result of this interpolation has then been used to calculate a value of α for the temperature closest to the one of the examined stellar track.

The result of all these calculations performed for the post Hydrogen burning part of the evolution of one of the initial stellar masses (namely the 22 $M_{\odot}$ one) is shown in the following plots, where in the first one the star is not rotating, and in the second one the star has a rotational speed of $\Omega/\Omega_{crit} = 0.6$.

Observing Figure 5.1, it is possible to see that the different $\dot{M}$ calculations all yield pretty similar results for the majority of the evolution, with a discrepancy of at most a factor 4 between the CAK mass loss and the ones of Bestenlehner, meaning that the two recipes produce reasonably similar results. The high peak could be due to possible instabilities in the simulations when the star enters the final stages of its life just before the supernova explosion.

Considering now the case for the rotating star in Figure 5.2, excluding the extreme and final stages of the stellar life, the discrepancy among the different recipes is significantly reduced, with just a small peak in correspondence of the activation of WR winds by [36].

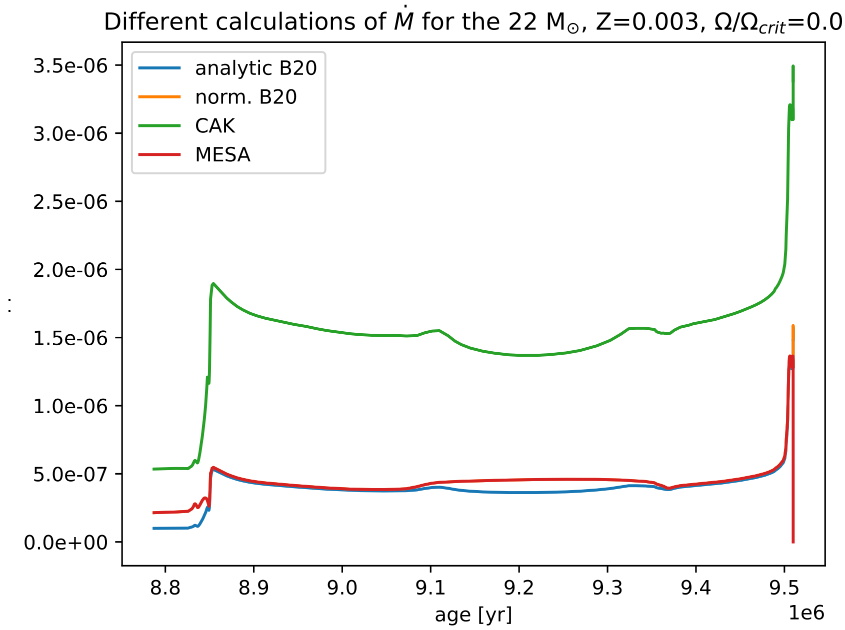

Figure 5.1: Comparison between the different calculations of $\dot{M}$, non-rotating case. The $\dot{M}$ from the MESA stellar track is in red, the $\dot{M}$ calculated with the normalization of equation 3.18is yellow, the $\dot{M}$ calculated with the formula of the CAK theory (equation 3.8 is green, and the analytic calculation of the whole formula by [22] is in blue.

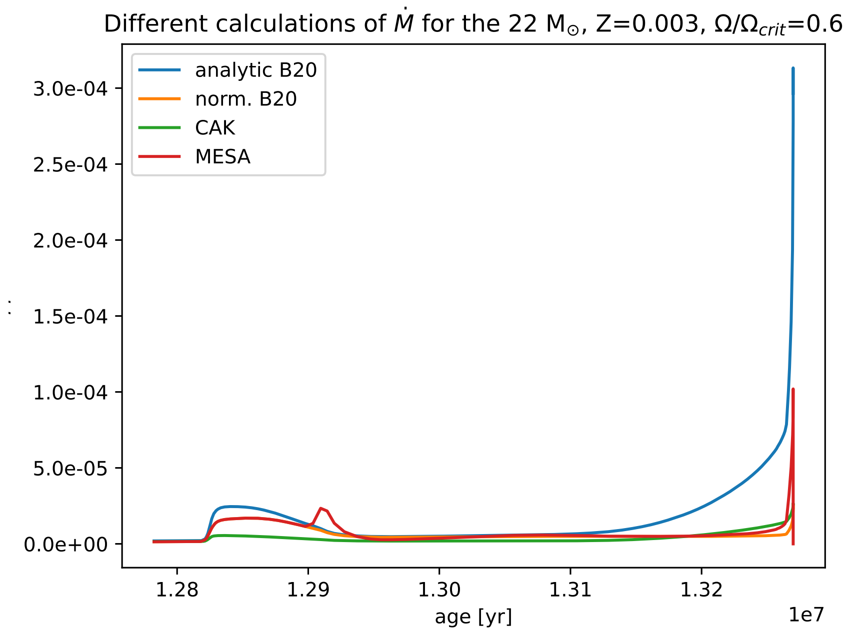

Figure 5.2: Comparison between the different calculations of $\dot{M}$, rotating case. For further information about the plot, see Figure 5.1

Overall, from the results of the calculations performed it is possible to draw some important conclusions:

- The approximations made by Bestenlehner on the CAK theory appear to be consistent, since the evolution of the obtained mass loss does not differ significantly from the one of the CAK theory.
- The normalization method chosen for this work yields results that are compatible with those that one would have obtained by choosing to compute the analytical formula theorized in [22].
- The choice of using a fixed value of alpha instead of the value obtained from the bilinear interpolation does not significantly influence the results.